5-1-2019

Multi-Resolution Spatio-Temporal Change Analyses of Hydro-Climatological Variables in Association with Large-Scale Oceanic-Atmospheric Climate Signals

Kazi Ali Tamaddun
kaziali.tamaddun@gmail.com

MULTI-RESOLUTION SPATIO-TEMPORAL CHANGE ANALYSES OF HYDRO-

CLIMATOLOGICAL VARIABLES IN ASSOCIATION WITH LARGE-SCALE

OCEANIC-ATMOSPHERIC CLIMATE SIGNALS

By

Kazi Tamaddun

Bachelor of Science – Civil Engineering
Bangladesh University of Engineering and Technology
2012

Master of Business Administration
University of Dhaka
2014

Master of Science in Engineering – Civil and Environmental Engineering
University of Nevada, Las Vegas
2016

A dissertation submitted in partial fulfillment
of the requirements for the

Doctor of Philosophy – Civil and Environmental Engineering

Department of Civil and Environmental Engineering and Construction
Howard R. Hughes College of Engineering
The Graduate College

University of Nevada, Las Vegas
May 2019

Dissertation Approval

The Graduate College
The University of Nevada, Las Vegas

April 9, 2019

This dissertation prepared by

Kazi Tamaddun

entitled

Multi-Resolution Spatio-Temporal Change Analyses of Hydro-Climatological Variables
in Association with Large-Scale Oceanic-Atmospheric Climate Signals

is approved in partial fulfillment of the requirements for the degree of

Doctor of Philosophy – Civil and Environmental Engineering
Department of Civil and Environmental Engineering and Construction

Sajjad Ahmad, Ph.D.   Kathryn Hausbeck Korgan, Ph.D.
Examination Committee Chair   *Graduate College Dean*

David James, Ph.D.
Examination Committee Member

Daniel Gerrity, Ph.D.
Examination Committee Member

Haroon Stephen, Ph.D.
Examination Committee Member

Ajay Kalra, Ph.D.
Examination Committee Member

Ashok Singh, Ph.D.
Graduate College Faculty Representative

ABSTRACT

The primary objective of the work presented in this dissertation was to evaluate the change patterns, i.e., a gradual change known as the trend, and an abrupt change known as the shift, of multiple hydro-climatological variables, namely, streamflow, snow water equivalent (SWE), temperature, precipitation, and potential evapotranspiration (PET), in association with the large-scale oceanic-atmospheric climate signals. Moreover, both observed datasets and modeled simulations were used to evaluate such change patterns to assess the efficacy of the modeled datasets in emulating the observed trends and shifts under the influence of uncertainties and inconsistencies. A secondary objective of this study was to utilize the detected change patterns in designing data-driven prediction models, e.g., artificial neural networks (ANNs), support vector machines (SVMs), and Gaussian process regression (GPR) models, coupled with data pre-processing techniques, e.g., principal component analysis (PCA) and wavelet transforms (WTs). The study was not solely limited to the hydrologic regions of the conterminous United States (U.S.); rather it was extended to include an analysis of northern India to appraise the differences in the spatiotemporal variation on a broader scale.

A task was designed to investigate the significant spatiotemporal variations in continental US streamflow patterns as a response to large-scale climate signals across multiple spectral bands (SBs). Using non-parametric (long-term) trend and (abrupt) shift detection tests, coupled with discrete wavelet transform, 237 unimpaired streamflow stations were analyzed over a study period of 62 years (1951 to 2012), looking at the water year and seasonal data, along with three discrete SBs of two, four, and eight years. Wavelet coherence analysis, derived from continuous wavelet transform, determined the association between the regional streamflow patterns and three large-scale climate signals, i.e., El Niño Southern Oscillation (ENSO), Pacific Decadal

Oscillation (PDO), and Atlantic Multi-decadal Oscillation (AMO), across continuous SBs ranging from two to 16 years. The results indicated significant positive (negative) trends and shifts in the northeastern and north-central (northwestern) regions with an increase in the number of stations as the SB durations increased. The spatiotemporal association between regional streamflow and climate signals varied significantly (from no correlation, $R_n^2 \sim 0$, to perfect correlation, $R_n^2 \sim 1.0$) even amongst adjacent regions. Among the climate signals, ENSO showed the highest association ($R_n^2 \sim 1.0$), having a consistent phase relationship with regional streamflow patterns, especially in the higher SBs. PDO (with the least influence among the three signals) and AMO showed stronger associations, in the lower SBs. These results may help explain the teleconnections between the climate signals and the US streamflow variations across multiple SBs, which may lead to improved regional flow regulations. The comparison among several data-driven models, e.g., ANN, SVM, and GPR models, preceded by PCA and WT, produced comparable results with significant accuracy (with R^2 above 0.90) in short-term prediction of streamflow.

Later, the correlations between the western U.S. snow water equivalent (SWE) and the two major oceanic-atmospheric indices originating from the Pacific Ocean, namely, ENSO and PDO, were evaluated using continuous wavelet transform and its derivatives. Snow Telemetry (SNOTEL) data for 1 April SWE from 323 sites (out of which 258 are in six hydrologic regions) were obtained for a study period of 56 years (1961–2016). The results showed that ENSO had a much higher influence than PDO throughout the western U.S. SWE across the study period. Both ENSO and PDO showed a higher correlation with SWE at multiple timescale bands across different time intervals, although significant intervals in the higher timescales were of longer duration. ENSO showed a higher correlation in the 10-to-16-year band across the entire study

period as well as in the lower timescales. PDO showed a higher correlation below the 4-year band. The relative phase relationship suggested that ENSO led SWE, with certain lags, while both were moving in the same direction in many instances. The lag-response behavior of SWE and PDO was not found to be uniform. Regional analyses, based on the western U.S. hydrologic regions, suggested significant variation across adjacent regions in terms of their correlation with ENSO/PDO. Association with ENSO was also observed to be higher compared to PDO among the regions. Regions close to the ocean and at lower elevation showed higher correlation compared to the inland regions with higher elevation.

The influence of ENSO on the north Indian temperature, precipitation, and PET change patterns was evaluated during the monsoon season across the last century. Trends and shifts in 146 districts were assessed using non-parametric statistical tests. To quantify their temporal variation, the concept of apportionment entropy was applied to both the annual and seasonal scales. Results suggest that the El Niño years played a greater role in causing hydro-climatological changes compared to the La Niña or neutral years. El Niño was more influential in causing shifts compared to trends. For certain districts, a phase change in ENSO reversed the trend/shift direction. The all-year (century-wide) analysis suggested that the vast majority of the districts experienced significant decreasing trends/shifts in temperature and PET. However, precipitation experienced both increasing and decreasing trends/shifts based on the location of the districts. Entropy results suggested a lower apportionment of precipitation compared to the other variables, indicating an intermittent deviation of precipitation pattern from the generic trend. The findings may help understand the effects of ENSO on hydro-climatological variables during the monsoon season. Practitioners may find the results useful, as monsoon, among the Indian seasons, experience the largest climate extremes.

A final task was designed that evaluated Coupled Model Intercomparison Project 5 (CMIP5) simulation models' ability to capture the observed trends under the influence of shifts and persistence in their data distributions. A total of 41 temperature and 25 precipitation CMIP5 simulation models across 22 grid cells (2.5° x 2.5° squares) within the Colorado River Basin were analyzed and compared against the Climate Research Unit Time Series (CRU-TS) observed datasets over a study period of 104 years (from 1901 to 2004). Both the model simulations and observations were tested for shifts, and the time series before and after the shifts were analyzed separately for trend detection and quantification. Effects of several types of persistence were accounted for prior to both the trend and shift detection tests. The mean significant shift points (SPs) of the CMIP5 temperature models across the grid cells were found to be within a narrower range (between 1960 and 1970) compared to the CRU-TS observed SPs (between 1930 and 1980). Precipitation time series, especially the CRU-TS dataset, had a lack of significant SPs, which led to an inconsistency between the models and observations since the numbers of grid cells with a significant SP were not comparable. The modeled CMIP5 temperature trends, under the influence of shifts and persistence, were able to match the observed trends quite satisfactorily (within the same order and consistent direction).

Unlike the temperature models, the CMIP5 precipitation models detected the SPs earlier than the observed SPs found in the CRU-TS data. The direction (as well as the magnitude) of trends, before and after significant shifts, were found to be inconsistent between the modeled simulations and observed precipitation data. Shifts, based on their direction, were found to either strengthen or neutralize pre-existing trends both in the model simulations as well as in the observations.

The results also suggest that the temperature and precipitation data distributions were sensitive to different types of persistence. Such sensitivity was found to be consistent between the modeled and observed datasets. The study detected certain biases in the CMIP5 models in detecting the SPs (a tendency of detecting shifts earlier or later than the observed shifts) and also in quantifying the trends (overestimating the trend slopes). Such insights may be helpful in evaluating the efficacy of the simulation models in capturing observed trends under uncertainties and natural variabilities.

ACKNOWLEDGMENT

DEDICATION

I dedicate this research to all the animals who are mercilessly treated and cruelly slaughtered for

mankind's own enjoyment. There is so little I can do to help them.

TABLE OF CONTENTS

LIST OF FIGURES

LIST OF ABBREVIATIONS

AC   -   Approximation Coefficient

AE_a -   Annual Apportionment Entropy

AE_s -   Seasonal Apportionment Entropy

AMO   -   Atlantic Multi-Decadal Oscillation

ANN   -   Artificial Neural Network

AR   -   Assessment Report

AWR   -   Arkansas-White-Red

CA   -   California

CMIP5   -   Coupled Model Intercomparison Project Phase 5

COI   -   Cone of Influence

CRB   -   Colorado River Basin

CRU-TS   -   Climate Research Unit Time Series

CS   -   Continuous Scale

CWT   -   Continuous Wavelet Transform

DC   -   Detail Coefficients

DJF   -   December-January-February

DS	-	Discrete Scale
DWT	-	Discrete Wavelet Transform
ENSO	-	El Niño Southern Oscillation
FT	-	Fourier Transform
GB	-	Great Basin
GL	-	Great Lakes
GPR	-	Gaussian Process Regression
HCDN	-	Hydro-Climatic Data Network
IMD	-	India Meteorological Department
IOD	-	Indian Ocean Dipole
IPCC	-	Intergovernmental Panel on Climate Change
ISMR	-	Indian Summer Monsoon Rainfall
JISAO	-	Joint Institute for the Study of the Atmosphere and Ocean
LC/LCO	-	Lower Colorado
LCRB	-	Lower Colorado River Basin
LMS	-	Lower Mississippi
LTP	-	Long-Term Persistence

MA   -   Mid-Atlantic

MK   -   Mann-Kendall

MK1   -   Original MK Test

MK2   -   Modified MK Test with TFPW – accounts for STP (Lag-1

Autocorrelation)

MK3   -   Modified MK Test – accounts for all the Significant

Autocorrelation Structures

MK4   -   Modified MK Test – accounts for LTP (Hurst Phenomenon)

MO   -   Missouri

MRA   -   Multi-Resolution Analysis

NE   -   New England

NOAA   -   National Oceanic and Atmospheric Administration

NRCS   -   Natural Resources Conservation Service

OH   -   Ohio

PC1   -   First Principal Component

PCA   -   Principal Component Analysis

PDO   -   Pacific Decadal Oscillation

PET	-	Potential Evapotranspiration
PN	-	Pacific Northwest
RG	-	Rio Grande
R_n^2	-	Wavelet Squared Coherency
SAG	-	South Atlantic-Gulf
SB	-	Spectral Band
SNOTEL	-	Snow Telemetry
SRS	-	Souris-Red-Rainy
SST	-	Sea Surface Temperature
STP	-	Short Term Persistence
SVM	-	Support Vector Machine
SWE	-	Snow Water Equivalent
TFPW	-	Trend-Free-Pre-Whitening
TN	-	Tennessee
TSA	-	Theil-Sen Approach
TXG	-	Texas-Gulf
U.S.	-	United States

UC/UCO	-	Upper Colorado
UCRB	-	Upper Colorado River Basin
UMS	-	Upper Mississippi
USGS	-	United States Geological Survey
WANN	-	Wavelet Artificial Neural Network
WT	-	Wavelet Transform
WTC	-	Wavelet Coherency
XWT	-	Cross Wavelet Transform

CHAPTER 1: INTRODUCTION

1.1. Research Background

Climate warming has affected hydrologic processes in various ways – one of them involves changes in the behavior and intensification of the hydrologic cycle (Durdu, 2010). The adverse consequences of these changes have increased under the changing climate, as the rapid increase in population stresses limited water resources (Wu et al., 2013). A detailed description of such adversities can be found in the assessment reports (AR5 and AR6) of the Intergovernmental Panel on Climate Change (IPCC) (IPCC, 2014 and 2019). Water managers have expressed concerns regarding the aftermath associated with access to fresh water as a response to the change in climate (Dawadi and Ahmad, 2013; Kandissounon et al., 2018). In a study of global and continental flow behaviors in relation to temperature increase by Labat et al. (2004), climate change was found to have a severe impact on North American streams. Studies indicate a considerable change in the intensity of flow behavior across the United States (U.S.), especially in the last century (U.S. EPA, 2012). As a consequence of the increasing temperature, flow regimes of the northern rivers in the U.S. have experienced major changes (Boyer et al., 2010). Hence, evaluating the change in flow behavior, along with other hydrologic variables, has become crucial to determining the effects of climate variability and change on limited water resources (Birsan et al., 2005). Changes in the intensity and frequency of flow events can potentially endanger critical infrastructures and the natural environment (Burn et al., 2010). Besides restricting access to potable water for future generations, with the escalating growth in the energy sector, the challenge becomes even more critical for water managers (Melesse et al., 2011; Bukhary et al., 2018). Therefore, quantification of streamflow change behavior across the

1

U.S. can be of utmost interest for a safe and sustainable future. A more recent approach focuses on the integration of multiple non-parametric methods to render better results, not only in terms of detection of change patterns but also to predict their behavior using data-driven models (Ahn and Palmer, 2015; Belayneh et al., 2016; Tiwari and Adamowski, 2017). Studies suggest that application of state-of-the-art machine learning techniques (intelligent models) can significantly increase the accuracy of hydro-climatological models' prediction (Tiwari and Adamowski, 2017). Coupling of pre-processing techniques, e.g., principal component analysis (PCA) and wavelet transforms (WTs), with intelligent models has also been found to increase the accuracy of time-series forecasting (Belayneh et al., 2016).

Among the various hydro-climatological variables, snow water equivalent (SWE) has been used as a common measurement of the snowpack. According to the Natural Resources Conservation Service (NRCS), SWE refers to the amount of water that is "contained within the snowpack". SWE can be thought of as the theoretical depth of water resulting from an instantaneous melting of the entire snowpack. Hence, snowpack in terms of SWE is considered a vital source of runoff in the water supply system across North America (Hunter et al., 2006; McCabe and Dettinger, 2002). The relative contributions of snowpack to water yield are much greater in the mountainous regions of the western U.S. than many other regions of the country. In these regions, approximately 50%-70% of the annual precipitation falls as snow, and is stored during the winter as snowpack (Palmer, 1988; Serreze et al., 1999); eventually, it affects the runoff of the succeeding seasons. The beginning of April is the time when snow courses attain maximum SWE. The 1 April SWE is used extensively in the western U.S. as an estimate to forecast the spring-summer runoff, and ultimately can be used to predict the annual runoff behavior in the surrounding regions. Understanding the relationships among the factors

influencing SWE could be beneficial to forecasters and water managers dealing with critical infrastructure management and irrigation practices (Hunter et al., 2006).

Studies on extreme climate events, i.e., droughts and floods, across the world, have found that such extremes are likely to be associated with the anomalies in zonal sea surface temperature (SST) fluctuations observed in the oceans. In turn, these fluctuations, coupled with the changes in global and regional atmospheric pressure systems, formation of surface winds, and moisture sources & evaporative demand, cause severe changes in the temperature and precipitation patterns (Diffenbaugh et al., 2015; Seager et al., 2015). Studies also suggest that these extremes are likely being aggravated by global warming (Williams et al., 2015; Yoon et al., 2015). The recent California drought has been of great interest to many climate researchers, (e.g., Griffin and Anchukaitis, 2014; Robeson, 2015). A study by Wei et al. (2016) identified major atmospheric circulation patterns affecting precipitation in California. However, the authors indicated that the contributions from the various components of the hydrologic cycle are yet to be properly understood. As a result, besides analyzing SST anomalies and precipitation patterns, recent studies have incorporated hydro-climatological variables like moisture sources, evaporative demand, and temperature in order to understand these climate extremes more thoroughly (Shukla et al., 2015; Pathak et al., 2016; Wei et al., 2016). In addition, various combinations of these variables have been found to show significantly different and sometimes inverse correlations with certain climate extremes. A few cases – for example, lower moisture with higher temperature – found to affect the extremes even more severely (Shukla et al., 2015). Hence, quantifying the changes in various hydro-climatological variables as a response to large-scale oceanic-atmospheric climate signals has become a significantly important topic of research for regional water managers and predictive climate data modelers.

1.2. Research Motivation

Studies show that changes in streamflow in the U.S. have experienced significant variations depending on the type of flow measurement, e.g., low flow, moderate flow, and peak flow (McCabe and Wolock, 2002). The variations were also found to be significant across different regions (Groisman et al., 2001) and at different temporal scales, e.g., annual and seasonal flows (Small et al., 2006). Studies also suggest that many of the traditional trend detection tests may not be resilient against nonlinearity (McBean and Motiee, 2006). Hence, those tests are often coupled with other analytical tools that are capable of dealing with nonlinear trends (Nalley et al., 2012), since such trends are relatively frequent in hydro-climatological data distributions. Over the past few decades, wavelet transforms (WTs), which can be either discrete or continuous in nature, have been used as an analytical tool in several studies that involved feature detection in frequency components (Partal and Küçük, 2006). Discrete wavelet transform (DWT), more precisely multi-resolution analysis (MRA), a derivation from DWT, has been used for spectral analysis in signal processing with the ability to decompose a signal into a set of high- to low-frequency components, referred to as spectral bands (SBs) in the following sections, which can assist in the analyses to detect the underlying features. A classification of streamflow into distinct hydro-climatic categories was provided by Smith et al. (1998) using DWT. Coulibaly and Burn (2004) explored the dynamic link between different climate signals and streamflow in the Northern Hemisphere by using continuous wavelet transform (CWT). The new WT analyses methods used in the field of hydrology have been reviewed and explained by Labat (2005). Pagano and Garen (2004) studied the western U.S. streamflow and suggested the use of WT for time-series analysis across multiple SBs for a better understanding of the less frequent events. Küçük and Ağiralioğlu (2006) suggested the use of WT as a better feature detection

4

technique compared to classical methods, e.g., Fourier transform (FT). Bayazit and Aksoy (2001), Drago and Boxall (2002), and Gaucherel (2002) also explored the use of WTs (both CWT and DWT) on nonstationary hydro-meteorological data at multiple temporal scales and recommended the WT approach over the traditional FT or derivatives of FT. Based on the documented literature, it was found that WT serves as a robust analytical tool in evaluating the change in hydro-climatological data. To explore the coupling of DWT and CWT, on a continental scale, to determine the association between large-scale oceanic-atmospheric climate signals across multiple temporal resolutions, and to utilize the detected associations in predictive models, was considered a major motivation of the study. Studies suggest that application of state-of-the-art machine learning techniques (intelligent models) can significantly increase the accuracy of hydro-climatological models' prediction (Tiwari and Adamowski, 2017). Coupling of pre-processing techniques, e.g., PCA and WT, with intelligent models has also been found to increase the accuracy of time-series forecasting (Belayneh et al., 2016). Hence, this study also tested the efficacy of several data-driven models preceded by PCA and WT.

As with studies dealing with snow derived data, besides analyzing the direct influence of climate on the western U.S. snowpack, studies have also examined the role of major climate indices on the hydrology of the western United States (Carrier et al., 2016; Kahya and Dracup, 1993). The El Niño Southern Oscillation (ENSO) and the Pacific Decadal Oscillation (PDO), both resulting from the Pacific Ocean, are considered to be two of the major large-scale oceanic-atmospheric climate signals that affect the western U.S. hydrology (Barnett et al., 1999; Beebee and Manga, 2004). Shifts in pressure cell locations and changes in their intensities cause trade winds to get stronger or weaker. This results in changes in the locations and velocities of oceanic currents – both of these cause upwelling of colder water from the bottom of the ocean, and move

5

warmer ocean-surface-water in specific directions, for example, east or west near the equator in the case of ENSO. Hence, SST fluctuations in multiple locations of the Pacific Ocean are initiated. The variations in pressure cells, coupled with the SST fluctuations, affect the direction, movement, and productivity of the storm tracks by affecting rates of oceanic evaporation and atmospheric moisture content. ENSO, a natural cycle observed in the eastern Pacific Ocean with a periodicity of two to seven years, alternates between two distinct phases, El Niño (positive or warm phase) and La Niña (negative or cold phase) (Redmond and Koch, 1991). PDO, which occurs on a timescale of 25 to 50 years, originates from the North Pacific Ocean, has a larger zone of influence compared to ENSO (Trenberth and Fasullo, 2007). Similar to ENSO, PDO also varies between warm and cold phases. Studies observing climate indices have also emphasized the teleconnection between the oceanic climate systems and the global hydrologic processes (Coscarelli et al., 2013; Sagarika et al., 2016). SST fluctuation alters the availability of moisture from the oceanic surface currents and eventually affects the formation of storm systems. Hence, SST fluctuations have the potential to influence hydro-climatological variables such as precipitation, snowpack, streamflow, runoff, and soil moisture. As a result, quantification of the associations between climate signals originating from the Pacific Ocean and the western U.S. SWE across multiple temporal resolutions was considered a major motivation of the study, since such an approach has not been adopted with snow derived data.

Outside the U.S. region, more specifically in the Indian sub-continent, the India Meteorological Department has observed and recorded monsoon patterns for several decades and has developed multiple stochastic models to forecast the initiation, recession, and strength of the Indian Summer Monsoon Rainfall (ISMR). Out of the many different factors affecting ISMR, ENSO has been considered to be one of the most significant large-scale forces that influence the

behavior of ISMR (Ju and Slingo, 1995; Kumar et al., 1999). As mentioned earlier, ENSO is a natural cycle originated from the tropical Pacific with two distinct phases. It is represented by an index, which records the SST fluctuations originating from the strengthening and weakening of the trade winds (Tamaddun et al., 2017a). Each phase of ENSO can last from a few months to a year, and they occur every two to seven years. From 1950 to 2012, ISMR was found to be above average or around average in almost all the La Niña years (negative or cold phase). Contrarily, five of the most prominent droughts in India during that period coincided with the El Niño years (positive or warm phase) (Kumar et al., 2006). A monsoon followed by El Niño does not necessarily result in poor rainfall all the time; however, as studies suggest, there might be other climate and weather factors, e.g., the extent of Himalayan/Eurasian snow, which influences the circulation of monsoon (Kumar et al., 1999). Studies have also suggested that other complementary factors to ENSO may affect ISMR, e.g., the Indian Ocean Dipole, complex coupling and dynamics of multiple variables, and variations in heat flux over different land masses (Webster and Yang, 1992; Ashok et al., 2001; Wang et al., 2005). Therefore, providing an in-depth analysis of the change patterns in multiple hydro-climatological variables of India during the monsoon season as a response to the phases of ENSO was considered a major motivation of the study.

1.3. Research Objectives

The primary objective of the work presented in this dissertation was to evaluate the change patterns, i.e., a gradual change known as the trend, and an abrupt change known as the shift, of multiple hydro-climatological variables, namely, streamflow, snow water equivalent (SWE), temperature, precipitation, and potential evapotranspiration (PET), in association with the large-scale oceanic-atmospheric climate signals. Moreover, both datasets and modeled

simulations were used to evaluate such change patterns to assess the efficacy of the modeled datasets in emulating the observed trends and shifts under the influence of uncertainties and inconsistencies. A secondary objective was to utilize the detected change patterns in designing data-driven prediction models, e.g., artificial neural networks (ANNs), support vector machines (SVMs), and Gaussian process regression (GPR) models, coupled with data pre-processing techniques, e.g., PCA and WT. The study was not solely limited to the hydrologic regions of the conterminous U.S.; rather it was extended to include an analysis of northern India to appraise the differences in the spatiotemporal variation on a broader scale. To attain the aforementioned objectives, the study was divided into four distinct tasks.

The first task detected the spatiotemporal trend and shift patterns of the conterminous U.S. streamflow across multiple frequency bands. Detection of change patterns across the frequency bands was expected to provide greater insight into the temporal variation of the streamflow patterns. Later, the changes in streamflow (along with their frequency bands) were associated with three large-scale oceanic-atmospheric climate signals, namely ENSO, PDO, and Atlantic Multi-decadal Oscillation (AMO). Later in this task, data-driven models were tested, preceded by PCA and WT, to evaluate the confidence in such models while predicting short-term streamflow behavior.

The second task detected the multi-resolution spatiotemporal association between the western U.S. SWE and the large-scale oceanic-atmospheric climate signals originating from the Pacific Ocean, i.e., ENSO and PDO. Since both these signals originate from the Pacific Ocean, which is relatively in closer vicinity to the western U.S., compared to the Atlantic Ocean, AMO was excluded from the analyses. Similar to the first task, this task also hypothesized that the

8

salient features of the association between the western U.S. SWE and the climate signals were better explained in their frequency components.

The third task extended the scope of the study by focusing on evaluating the trend and shift patterns of temperature, precipitation, and PET across northern India during the monsoon season. The change patterns were compared against the various phases of ENSO to weigh their influence on the Indian climate extremes. The spatiotemporal relationships among the variables, i.e., temperature, precipitation, and PET, were investigated as well across the last century. Moreover, this task also intended to determine the apportionment entropy, i.e., distribution of trends over the years or the months of a season, to provide greater insights into the trend quantification process.

In the final task, observed and modeled (Coupled Model Intercomparison Project Phase 5 – referred to as CMIP5 in the following sections) temperature and precipitation trends, for the Colorado River Basin, were compared under the influence of change (abrupt shift) points and several autocorrelation types (known as persistence in the hydrology literature) to determine the models' ability in mapping the observed behavior. Such analyses may estimate the inherent bias in the modeled datasets, and the obtained results may be helpful in adjusting the models, especially when used for predicting future scenarios. Choice of the appropriate model, among a large pool of available models for a particular region, can also be beneficial for regional water management. The formulations of each of the tasks were based on the following set of questions, which were supported by their respective research basis.

Task 1: Multi-scale spatiotemporal change analysis and short term projection of the conterminous U.S. streamflow in response to large scale climate variability.

Research Questions:

- What are the spatiotemporal trend and shift patterns of the conterminous U.S. streamflow in association with large-scale oceanic-atmospheric climate signals across multiple frequency bands?

- How effective are data-driven models, e.g., ANN, SVM, and GPR, when coupled with data pre-processing techniques, e.g., PCA and WT, in predicting short-term streamflow behavior?

Research Basis: Detection of trends and shifts across multiple frequency bands may provide a better understanding of the nature of the change patterns, especially when such changes have been found to be associated with the oscillatory behavior of large-scale oceanic-atmospheric climate signals such ENSO, PDO, and AMO. Since these signals contain multiple frequency components and alternating phases when changing over a long time, associating the streamflow change patterns with these signals across various frequency bands can be of significant importance. The detected intra-variation and inter-covariation between streamflow and the climate signals across multiple frequency bands may have the potential to improve the predictive ability of the data-driven models, e.g., ANN, SVM, and GPR, when coupled with pre-processing techniques and designed/optimized properly.

Major Contributions:

- Detection of trends and shifts of the conterminous U.S. streamflow in the original as well as decomposed time series of the water year and seasonal data using non-parametric statistical tests.

- Determination of spatiotemporal association between the regional streamflow and large-scale oceanic-atmospheric climate signals originating from both the Pacific and Atlantic Oceans.

- Testing of data-driven models coupled with data pre-processing techniques to predict short-term streamflow behavior.

- Evaluation of relative phase relationships (lag-response behavior) between the climate signals and the regional streamflow across multiple time scales along the study period.

Task 2: Multi-scale correlation between the western U.S. snow water equivalent and large-scale climate variability of the Pacific Ocean.

Research Questions:

- How do the large-scale oceanic-atmospheric climate signals originating from the Pacific Ocean affect the western U.S. SWE across multiple frequency bands?

- Which regions of the western U.S. have maintained a consistent phase relationship, in terms of SWE, with the large-scale climate signals originating from the Pacific Ocean; and how does the lag-response behavior change across multiple frequency bands?

Research Basis: Association between regional western U.S. SWE and the large-scale oceanic-atmospheric climate signals originating from the Pacific Ocean, e.g., ENSO and PDO, can be better explained in their frequency components since these signals contain multiple frequency components. Such signals also alternate between phases when changing over a long time. The detected correlation between SWE and the climate signals across multiple frequency bands may provide a better insight into their spatiotemporal relationships and may explain their phase relationships with greater detail.

Major Contributions:

- Multi-scale correlational analysis of the western U.S. SWE, both state-wise and hydrologic region-wise, in response to Pacific Ocean climate signals.

- Evaluation of relative phase relationships (lag-response behavior) between the climate signals and the regional western U.S. SWE across multiple time scales along the study period.

Task 3: Spatiotemporal trend, shift, and entropy analyses of temperature, precipitation, and potential evapotranspiration of north Indian monsoon during the ENSO phases.

Research Questions:

- What are the spatiotemporal trends and shift patterns of temperature, precipitation, and potential evapotranspiration in the north Indian monsoon (and its comprising months) across the last century during the phases of ENSO?

- What is the rate of change (slope) of the trends and how are the trends distributed (apportioned) along the years and through the months of monsoon?

Research Basis: Large-scale oceanic-atmospheric climate signals, such as ENSO and their phases have been found to influence global hydro-climatological patterns in various ways based on the geography and the seasonal variation of a region. Among the different regions of India, the northern part of the country has been observed to experience many different climate extremes, e.g., storms, droughts, and floods, over the years. Since monsoon is the single most important season for the region, evaluation of the temperature, precipitation, and PET patterns (both trends and shifts) across the last century, especially during the various phases of ENSO,

can be of great value to regional water management. A proper quantification, e.g., the rate of change and apportionment, of the trends can also be helpful in evaluating temporal variation across the years and through the months of monsoon, which lasts from June to September. Moreover, as the literature suggests, the multi-variable analyses approach to be adopted in the study may help investigators to understand the response of regional hydrology to large-scale climate signals such as ENSO.

Major Contributions:

- Evaluation of the long-term trend and abrupt shift patterns of temperature, precipitation, and PET across north India at the various ENSO phases using non-parametric statistical tests.

- Determination of the spatiotemporal relationships between the selected variables during monsoon and at each of the monsoonal months over a century-wide period.

- Comparison between the major shift points during monsoon and the phases of ENSO, which might have resulted in extreme events, e.g., flood or drought, throughout the study period.

- Analyses of entropy (apportionment entropy) to quantify how the detected variations were distributed temporally over the years (annually) and during the months (seasonally) of monsoon along the study area.

Task 4: Comparison of trends and shifts in the observed and modeled temperature and precipitation patterns of the Colorado River Basin under shifts and persistence.

Research Questions:

- What are the direction and magnitude of temperature and precipitation trends in the Colorado River Basin along the last century in the observed and modeled (CMIP5) gridded datasets?

- How do the shifts alter the direction and magnitude of the trends and what are the influences of various types of persistence, e.g., short and long-term autocorrelation, on the observed and modeled trends?

Research Basis: Comparison between observed and modeled datasets provides a set of qualitative and quantitative metrics to evaluate the accuracy of the modeled datasets, especially when such modeled datasets are heavily used for hydro-climatological prediction, such as the CMIP5. Assessment of trends (both in direction and magnitude) in the observed and modeled datasets can be helpful in correcting the bias (if any) in the modeled datasets. Moreover, such trends can highly be influenced by the presence of shifts, which can alter or moderate an existing trend. An undetected shift may result in poor estimation of a trend. Besides, the presence of persistence, i.e., autocorrelation in data, can overestimate a trend unless it is removed before the application of trend detection tests.

Major Contributions:

- Adoption of a shift-trend approach where the direction and magnitude of the trends are evaluated independently before and after significant shift points for both the modeled and observed datasets.

- A thorough examination of the effect of persistence not only for the trend tests but also for the detection of shift points.

- Determination of the inconsistencies detected between the CMIP5 and observed datasets – under the influence of shift points and persistence.

1.4. Research Tasks

The tasks conducted are presented in manuscript formats. The current chapter contains the introduction and formulates the research questions for the study. Chapter 2 is a manuscript titled "Multi-scale spatiotemporal change analysis and short term projection of the conterminous U.S. streamflow in response to large scale climate variability", which addresses the first set of research questions based on the underlying basis discussed earlier. This task investigated the significant spatiotemporal variations in the continental U.S. streamflow patterns as a response to large-scale climate signals across multiple spectral bands. Chapter 3 is a manuscript titled "Multi-scale correlation between the western U.S. snow water equivalent and large-scale climate variability of the Pacific Ocean", which addresses the second set of the research questions based on the associated research basis. This task determined the correlations between the western U.S. SWE and the two major oceanic-atmospheric indices originating from the Pacific Ocean, namely, ENSO and PDO, were evaluated using continuous wavelet transform and its derivatives. Chapter 4 is another manuscript titled "Spatiotemporal trend, shift, and entropy analyses of temperature, precipitation, and potential evapotranspiration of north Indian monsoon during the ENSO phases", which addresses the third set of research questions based on their underlying basis. This task determined the influence of ENSO on the north Indian temperature, precipitation, and PET change patterns were evaluated during the monsoon season across the last century. Chapter 5 is the last manuscript titled "Comparison of trends and shifts in the observed and modeled temperature and precipitation patterns of the Colorado River Basin under shifts and persistence", which address the last set of research questions based on their research basis

discussed in the previous section. This task evaluated CMIP5 simulation models' ability to capture the observed trends under the influence of shifts and persistence in their data distributions. Each of the chapters associated with the manuscripts also has its own introduction, study area and data, methodology, results, discussion, and conclusions sections. Chapter 6 summarizes all the tasks along with their major contributions and limitations. It also contains recommendations for future work.

CHAPTER 2: MULTI-SCALE SPATIOTEMPORAL CHANGE ANALYSIS AND SHORT-TERM PREDICTION OF THE CONTERMINOUS U.S. STREAMFLOW IN RESPONSE TO LARGE SCALE CLIMATE VARIABILITY

2.1. Introduction

Climate warming has affected hydrologic processes in various ways – one of the most prominent involves changes in the behavior and intensification of the hydrologic cycle (Durdu, 2010). The adverse consequences of these changes have increased under the changing climate, as the rapid increase in population stresses limited water resources (Wu et al., 2013). A detailed description of such adversities can be found in the assessment reports (AR5 and AR6) of the Intergovernmental Panel on Climate Change (IPCC) (IPCC, 2014 and 2019). Water managers have expressed concerns regarding the aftermath associated with access to fresh water as a response to the change in climate (Dawadi and Ahmad, 2013; Thakali et al., 2016 and 2018). In a study of global and continental flow behaviors in relation to temperature increase by Labat et al. (2004), climate change was found to have a severe impact on North American streams. Studies indicate a considerable change in the intensity of flow behavior across the United States (U.S.), especially in the last century (U.S. EPA, 2012). As a consequence of the increasing temperature, flow regimes of the northern rivers in the U.S. have experienced major changes (Boyer et al., 2010). Hence, evaluating the change in flow behavior, along with other hydrologic variables, has become crucial to determining the effects of climate variability and change on water resources (Birsan et al., 2005). Changes in the intensity and frequency of flow events can potentially endanger critical infrastructures and the natural environment (Burn et al., 2010; Tamaddun et al., 2015). Besides restricting access to potable water for future generations, with the escalating growth in the energy sector, the challenge becomes even more critical for water managers

17

(Melesse et al., 2011). In previous studies (Tamaddun et al., 2016a and 2016b), the changes in flow were divided into two broad categories, namely, the long-term trend, a gradual and monotonic change that was observed in the past, and the abrupt shift, a sharp change in the flow regime. Inattention to such changes may result in poor decision making in water resources management (Mirchi et al., 2012). As a result, besides emphasizing the knowledge of the regional trends and shifts as a response to large-scale climate variabilities (Clark et al., 2000), studies have suggested modifications of regional public policies to cater to these changes (Nalley et al., 2012).

Studies show that changes in streamflow in the U.S. have experienced significant variations depending on the type of flow measurement, e.g., low flow, moderate flow, and peak flow (McCabe and Wolock, 2002; Jobe et al., 2018). The variations were also found to be significant across different regions (Groisman et al., 2001) and at different temporal scales, e.g., annual and seasonal flows (Small et al., 2006). Studies also suggest that many of the traditional trend detection tests may not be resilient against nonlinearity (McBean and Motiee, 2006). Hence, those tests are often coupled with other analytical tools that are capable of dealing with nonlinear trends (Nalley et al., 2012), since such trends are relatively frequent in hydro-climatological data. Over the past few decades, wavelet transforms (WTs), which can be either discrete or continuous in nature, have been used as an analytical tool in several studies that involved feature detection in frequency components (Partal and Küçük, 2006). Discrete wavelet transform (DWT), more precisely multi-resolution analysis (MRA), a derivation from DWT, has been used for spectral analysis in signal processing with the ability to decompose a signal into a set of high- to low-frequency components, referred to as spectral bands (SBs) in the following sections, which can assist in the analyses to detect the underlying features. A classification of

streamflow into distinct hydro-climatic categories was provided by Smith et al. (1998) using DWT. Coulibaly and Burn (2004) explored the dynamic link between different climate signals and streamflow in the Northern Hemisphere by using continuous wavelet transform (CWT). The new WT analyses methods used in the field of hydrology have been reviewed and explained by Labat (2005). Pagano and Garen (2004) studied the western U.S. streamflow and suggested the use of WT for time-series analysis across multiple SBs for a better understanding of the less frequent events. Küçük and Ağiralioğlu (2006) suggested the use of WT as a better feature detection technique compared to classical methods, e.g., Fourier transform (FT). Bayazit and Aksoy (2001), Drago and Boxall (2002), and Gaucherel (2002) also explored the use of WTs (both CWT and DWT) on nonstationary hydro-meteorological data at multiple temporal scales and recommended the WT approach over the traditional FT or derivatives of FT. Based on the documented literature, it was found that WT serves as a robust analytical tool in evaluating the change in hydro-climatological data.

The primary objective of the current study was to evaluate the effects of SBs on the spatiotemporal trends and shifts of the continental U.S. streamflow across hydrologic regions and to determine their association with large-scale climate signals. Hence, streamflow data from 237 unimpaired stations were obtained and decomposed into multiple low-resolution subseries using DWT. The original time series along with their decompositions were then analyzed using non-parametric tests that are not limited to any particular probability distributions. Trends and shifts were detected using the Mann-Kendall (MK) (Mann, 1945; Kendall, 1975) test and the Pettitt's test (Pettitt, 1979), respectively. Later, wavelet coherence (WTC) analysis, derived from CWT, was used to determine the spatiotemporal association between regional streamflow and three large-scale climate signals, i.e., El Niño Southern Oscillation (ENSO) and Pacific Decadal

19

Oscillation (PDO), representing the sea-surface temperature (SST) fluctuations originating from the Pacific Ocean; and Atlantic Multi-decadal Oscillation (AMO), representing the SST fluctuation originating from the Atlantic Ocean. The analyses were conducted over a study period of 62 years, i.e., from 1951 to 2012. Emphasis on applying multiple statistical methods found in the literature (Ahn and Palmer, 2015), while analyzing hydro-climatological data, motivated the current study to adopt such an extensive analyses approach to provide an in-depth analysis on a continental scale, which is novel to the current study.

In a previous effort, Sagarika et al. (2014) assessed the trends and shifts of the U.S. streamflow accounting for autocorrelation (known as persistence in the hydrology literature) in data. The current study extended the depth of analyses by incorporating the effects of spectral frequencies in determining the streamflow variability. Besides the water year, this study also determined the seasonal trends and shifts, since the seasons play a significant role in the demand sector, especially in arid regions. Pathak et al. (2016) used trend analysis, coupled with DWT, to evaluate the hydrologic changes in the mid-western United States. In addition to applying DWT on a continental scale, the current study broadened the scope further by applying WTC in order to evaluate the association between regional streamflow patterns and large-scale climate signals. As many of the climate signals exhibit oscillatory behavior, application of WTs in understanding the effects of their frequency components in association with the U.S. streamflow was considered pivotal to the study. Even though removal of persistence before analyzing trends in data is found in the literature and is considered to be important (Serinaldi and Kilsby, 2016), studies suggest that the performance of the commonly used methods may not be satisfactory enough, and therefore, can produce biased results (Khaliq et al., 2009). Moreover, the MRA approach utilized in this study involves the application of high and low pass filters; hence, the

removal of persistence from the decomposed components was considered to be redundant. The data used in the study were obtained from unimpaired streamflow stations only; such stations can better represent the effects of climate variability since they are free from anthropogenic interference, meaning the flow paths of the selected streams on which the stations were located had not been modified by human activity. As decomposed time series are of lesser complexity than the originals, the salient features of the location of data variability, e.g., more frequent events or more uncommon extremes, are better represented in the decomposed series (Restrepo et al., 2014; Bhandari et al., 2018; Tamaddun et al., 2019a). As a result, the current study hypothesized that the spectral components can better explain the relationship between the local variations and large-scale climate variability. This is the first study in the documented literature that couples trend and shift detection tests with spectral component (frequency) analyses on a continental scale, and analyzes the change patterns in association with multiple large-scale climate signals. Such robust analyses may help explain the physical mechanisms of the oceanic-atmospheric systems that affect the U.S. streamflow. A more recent approach focuses on the integration of multiple non-parametric methods to render better results, not only in terms of detection of change patterns but also to predict their behavior using data-driven models (Ahn and Palmer, 2015; Belayneh et al., 2016; Tiwari and Adamowski, 2017). Studies suggest that application of state-of-the-art machine learning techniques (intelligent models) can significantly increase the accuracy of hydro-climatological models' prediction (Tiwari and Adamowski, 2017; Ateeq-ur-Rauf et al., 2018; Bhandari et al., 2019). Coupling of pre-processing techniques, e.g., principal component analysis (PCA) and WT, with intelligent models have also been found to increase the accuracy of time-series forecasting (Belayneh et al., 2016). Hence, this study also tested the efficacy of multiple data-driven models preceded by PCA and DWT. Besides

quantifying trends and shifts in association with large-scale climate signals, the results of this study may also be useful in improving forecasting models based on the detected multi-resolution associations, which may lead to making better water management decisions.

2.2. Study Area and Data

Out of the 704 unimpaired streamflow stations across the 18 hydrologic regions of the continental U.S. listed in the Hydro-Climatic Data Network (HCDN)-2009 (Lins, 2012) published by the United States Geological Survey (USGS) (http://water.usgs.gov/GIS), 237 stations were selected, each having 62 years of continuous monthly mean data from 1951 to 2012. To avoid spatial bias, in cases of streams with multiple stations, the stations at upstream locations were selected. Figure 2.1 (left) shows the locations of the stations across the hydrologic regions. The water-year mean, ranging from the previous year's October to the current year's September, and the seasonal means, i.e., fall (Oct-Dec), winter (Jan-Mar), spring (Apr-Jun), and summer (Jul- Sept), were used for the analyses. Figure 2.1 (inset table in the middle) shows the number of stations in each region along with the abbreviations used in the text to refer to the regions.

The monthly ENSO and AMO indices were obtained from the National Oceanic and Atmospheric Administration's (NOAA) (https://www.esrl.noaa.gov/) online database. The monthly PDO indices were obtained from the Joint Institute for the Study of the Atmosphere and Ocean's (JISAO) (http://www.jisao.washington.edu/) database. JISAO is a research collaboration between the University of Washington and NOAA.

Region No.	Hydrologic Region Name	Number of stations
1	New England (NE)	18
2	Mid-Atlantic (MA)	39
3	South Atlantic-Gulf (SAG)	21
4	Great Lakes (GL)	10
5	Ohio (OH)	20
6	Tennessee (TN)	8
7	Upper Mississippi (UMS)	19
8	Lower Mississippi (LMS)	2
9	Souris-Red-Rainy (SRR)	3
10	Missouri (MO)	21
11	Arkansas-White-Red (AWR)	11
12	Texas-Gulf (TXG)	5
13	Rio Grande (RG)	3
14	Upper Colorado (UCO)	
15	Lower Colorado (LCO)	2
16	Great Basin (GB)	4
17	Pacific Northwest (PN)	37
18	California (CA)	14
	Total	237

Figure 2. 1: (Left) Locations of 237 unimpaired streamflow stations analyzed in the study across the continental United States. Hatched regions were analyzed to determine their associations with the climate signals. **(Middle)** Number of stations in each hydrologic region analyzed in the study. The regions are referred to in the text by the abbreviations as shown in the parenthesis. **(Right)** Time-series plots of the station at Santa Cruz River near Lochiel, AZ (as a sample): **(a)** standardized plot of the original water year data, **(b)** first detail coefficient (DC) corresponding to DS2, **(c)** second detail coefficient corresponding to DS4, **(d)** third detail coefficient corresponding to DS8, and **(e)** third approximation coefficient (AC).

23

2.3. Methods

Trend and shift detection tests were applied on the original as well as on the decomposed time-series. Characteristics of the test methods, such as the ability to analyze skewed (non-normal) distributions, resistance to outliers, and sensitivity to non-stationarity in hydro-climatic data (Lins and Slack, 1999), dictated the choice of these two test methods (Önöz and Bayazit, 2003; Villarini et al., 2009). DWT, with MRA being used as the design method, was applied to obtain the time series at discrete scales (DSs). WTC, preceded by CWT, was used to determine the spatiotemporal association between the regional streamflow and the climate signals across continuous scales (CSs). In the following sections, brief descriptions of the MK and Pettitt's tests, followed by discussions of DWT, MRA, CWT, and WTC have been provided based on the previous literature. Please refer to the original sources for the fundamental theories and mathematics behind each test.

2.3.1. Trend and shift tests

The MK trend test (Mann, 1945; Kendall, 1975) is based on the null hypothesis that there is no trend in the time series. The test determines the direction of the trend, which can either be an increase (positive), decrease (negative), or absence of a trend, from the sign of a signum function. The Pettitt's test (Pettitt, 1979) detects the shift in a time series by testing the anomaly between the mean of two independent samples from the same time series. The direction of the shift, which can be either positive, negative, or an absence of a shift, is determined from the maximum and minimum probability estimates based on the significance level used. More details about and applications for these two tests can be found in the work of Villarini et al. (2009). The Walker's test (Wilks, 2006) was used to estimate the field significance of the individual regions depending on the number of significant stations within the region. This test uses the binomial distribution to determine if the number of significant trends observed could have happened by chance. A detailed discussion on regional trends can be found in the work of Helsel and Frans (2006). The MK test, the Pettitt's test, and the field significance test were analyzed at a minimum of 10% significance level ($p \leq 0.10$).

2.3.2. Wavelet transforms

The original streamflow time-series were decomposed using the wavelet toolbox found in the software package of MATLAB. For DWT, Coiflet was used as the mother wavelet function, which is symmetric in nature and is desirable for a linear response of the filter, which relates to the stability of the filter and helps in analyzing the trend in a robust way. For more details on choosing a wavelet function, readers may refer to Torrence and Compo (1998). MRA, which is a one-dimensional wavelet decomposition technique, was used as the design method of DWT.

MRA uses a sub-band coding technique for multiple wave reconstruction. Dilates and translates are generated by using the mother wavelet function to decompose the time domain into lower to higher spectral frequency bands (Karthikeyan and Nagesh Kumar, 2013), which are useful in representing the multiple resolutions of the time-frequency domain (Tan et al., 2011). More details on the wavelet transform used in this study can be found in Appendix 2.A.

The CWT approach, followed by the WTC analyses adopted in the study, was based on the works of Jevrejeva et al. (2003) and Grinsted et al. (2004). Morlet was used as the wavelet function for CWT. CWT determines the variance in a time series across the SBs, while WTC quantifies the correlation between two time series across the SBs. Readers may also refer to Tamaddun et al. (2017a and 2017b) for further explanation of each of the steps adopted in the study. CSs ranging from two to 16 years were considered in the analyses since the amount of uncertainty increased as the resolution decreased beyond the SBs of 16 years. DSs at two, four, and eight years were also chosen for the same reason, as can be seen in Figure 2.1 (right) – after three decompositions, little resolution remained in the time series. The following sections use the terms DS and CS to refer to the time series at different SBs associated with the discrete and continuous scales, respectively. For example, CS8 to CS16 refers to the time series associated with the continuous SBs ranging from eight to16 years, while DS4 refers to the four-year discrete SB. The CWT and WTC were analyzed with a minimum of 5% significance level against red noise. The non-stationary behavior of hydro-climatic variables in time-series analysis and the use of wavelets to address such behavior have been discussed in the works of Karthikeyan and Nagesh Kumar (2013) – this work also suggests the type of significance tests to be used in a hydro-climatic time-series analysis.

2.3.3. Wavelet artificial neural network (WANN) modeling

The final step of the study was to incorporate all the findings from the previous steps and combine them in artificial neural network (ANN) models to be used for short-term prediction. In this step, the discretized subseries (the first three details, i.e., DS2, DS4, and DS8 and the third approximation, i.e., AC3, as shown in Figure 2.1) of the regional streamflow patterns as well as of the three climate signals were fed into a set of ANN learning algorithms. PCA was conducted to determine the inputs that are statistically independent of each other. Moreover, the most efficient (or optimal) number of hidden neurons for each of the region was determined based on the guidelines provided by Belayneh et al. (2016). The data sets were divided into two independent segments before training the models. The first segment consisted of 50 years of data ranging from 1951 to 2000, which were used for training and validation. The second segment consisted of the remaining 12 years of data, i.e., 2001 to 2012, which were used for testing (with unseen data). Besides validation with 20% random sampling, K-fold cross-validation technique was adopted to train and validate the models, where at each fold, 20% of the data were left out for validation, while the remaining 80% of the data were used for training (resulted in a total of 5 folds). The training and validation of the models are discussed in the results section. Three groups of algorithms were tested in this study: (i) backpropagation training function with Jacobian derivative, (ii) backpropagation training function with gradient derivative, and (iii) supervised weight/bias training functions. A total of 17 learning algorithms were tested from these three groups. More details on ANN models coupled with wavelets (WANN) can be found in Belayneh et al. (2016), Tiwari and Adamowski (2017), and Worland et al. (2018). Similar training, validation (K-fold cross-validation), and testing were conducted using support vector

machines (SVMs) and Gaussian process regression (GPR) models to compare them against the WANN models. The final results have been reported in the results section.

2.4. Results

The study analyzed the continental U.S. streamflow trends and shifts (in the original time series and in their DSs), as well as quantified the spatiotemporal association between the regions experiencing significant shifts and three large-scale climate signals across the CSs. Figure 2.2 illustrates the location of the stations with significant trends and shifts in water year and their DSs. Figures 2.3 and 2.4 show the WTC results that quantified the correlation (wavelet squared coherency, R_n^2) between the regional streamflow and the climate signals. Additional tables (Tables A2.B1 and A2.B2) are provided in Appendix 2.B, while both Appendices A2.C and A2.D contain additional figures and their descriptions. Results of the short-term (one step ahead) prediction with SVM, GPR, and WANN for the regions MA, MO, PN are provided in Figures 2.5 to 2.7. Additional figures (Figures A2.E1 to A2.E21) and tables (Tables A2.E1 to A2.E6), containing the results of PCA, effect of hidden neurons on model performance, selected WANN model architecture, validation with random sampling, K-fold cross-validation, and comparison among several models and learning algorithms are provided in Appendix A2.E.

2.4.1. Trends and shifts in water years and seasons

In a water year and its DSs, positive trends were observed in the northeastern and north-central regions, while negative trends were located in the northwestern region (Figure 2.2). NE, MA, GL, OH, UMS, SRR, MO, AWR, TXG, and RG showed a significant number of stations with positive trends, while negative trends were observed in PN and CA. The number of stations

with significant trends and regions with field significance increased as the decomposition level increased (DSs increased) (Table A2.B1).

Stations with positive shifts, in water years and their DSs, followed similar spatial patterns to the ones with positive trends. However, stations with negative shifts were found to be more spatially dispersed (Figure 2.2). A steady increase in the number of stations with significant shifts, with an increase in DSs, was noticeable (Table A2.B2), which was not so evident for the stations with trends. Among the regions, NE, MA, SAG, GL, OH, UMS, MO, AWR, and TXG showed positive shifts, while negative shifts were observed in SAG, PN, and CA. In the higher DSs, all regions showed field significance.

Trends and shifts at each of the seasons, along with their DSs, were also evaluated (Appendix 2.C). The results showed a unique spatial pattern of stations with significant trends and shifts during each season. Fall (winter) showed similarity with summer (spring) in terms of the spatial pattern of significant stations. The increase in the number of significant stations with the increase in DSs was also noticeable in each of the seasons.
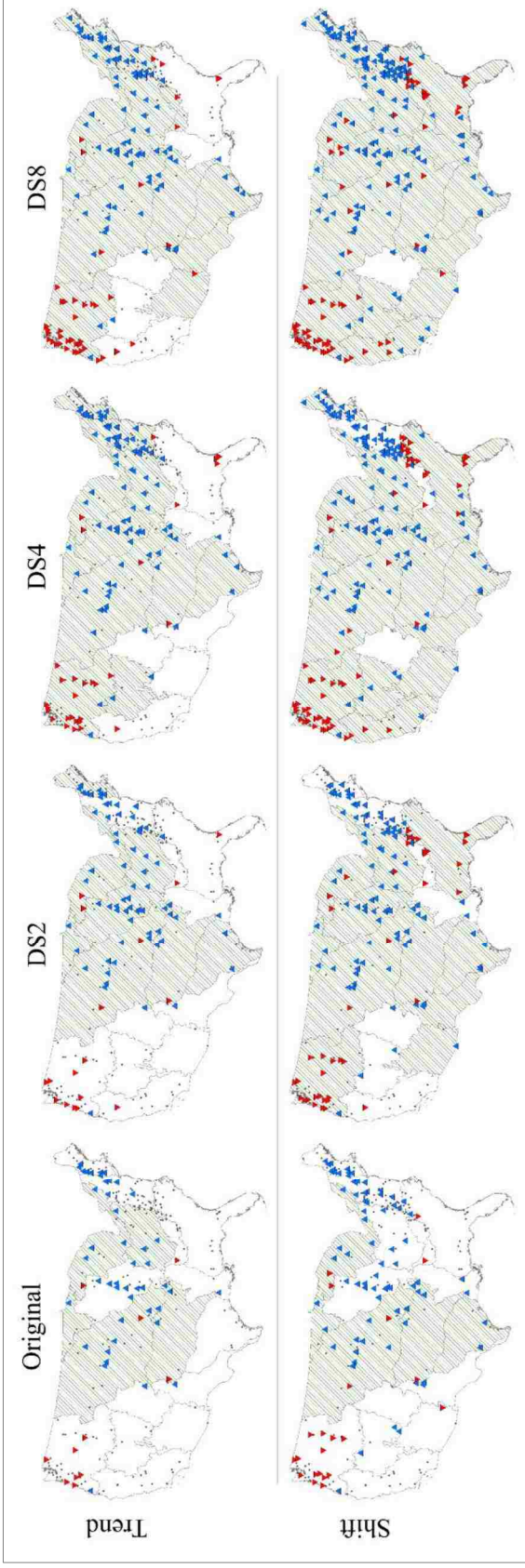
Figure 2. 2: Location of stations with significant trends (**1st row**) and shifts (**2nd row**), respectively, in the original water year and its DSs. Upward (downward) pointing blue (red) triangles represent significant positive (negative) trends and shifts at $p ≤ 0.10$. Shaded regions represent field significance.

30
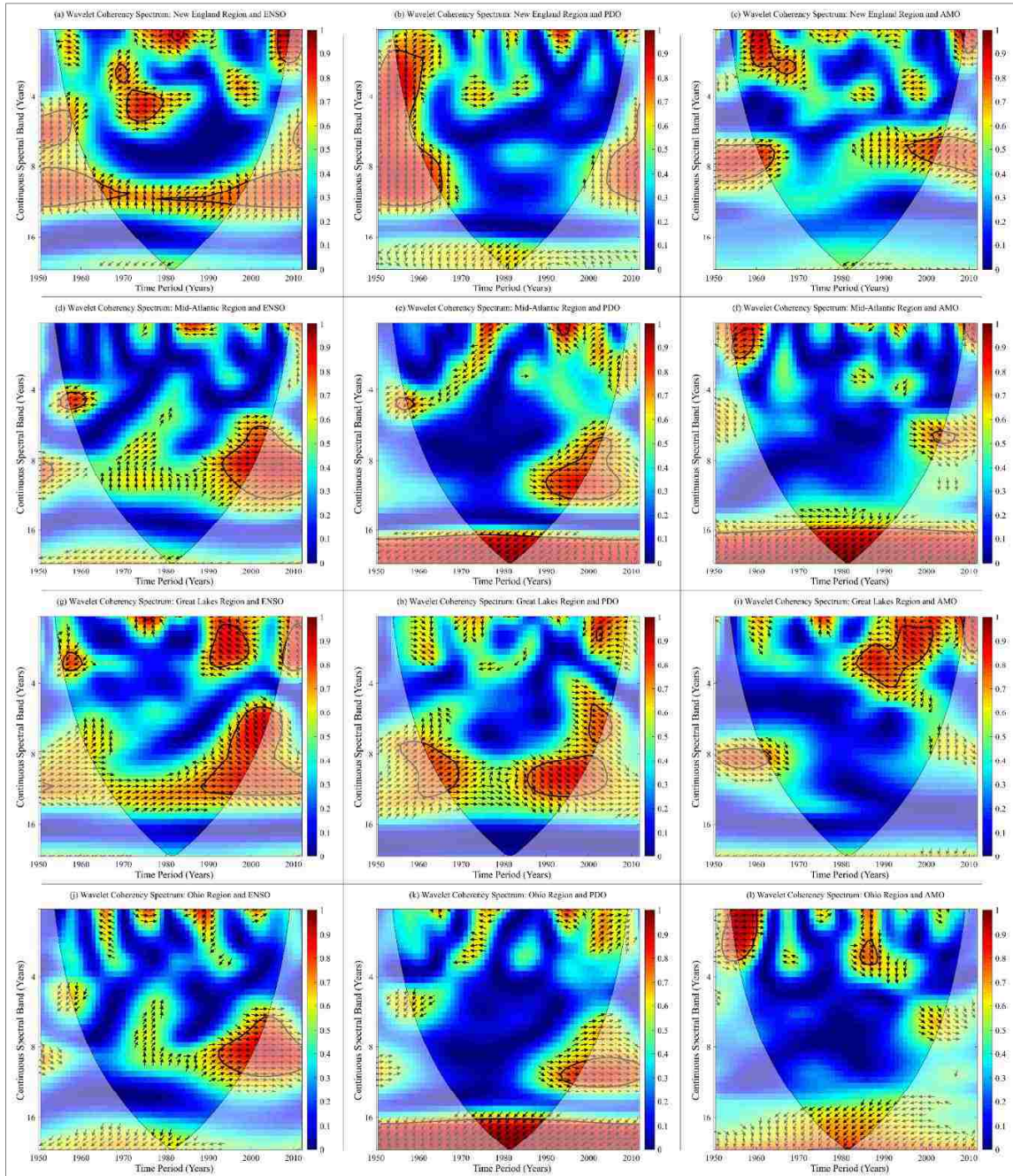
Figure 2. 3: Wavelet coherence spectra between regional streamflow of (**1ˢᵗ row**) New England, (**2ⁿᵈ row**) Mid-Atlantic, (**3ʳᵈ row**) Great Lakes, and (**4ᵗʰ row**) Ohio and the climate signals of (**1ˢᵗ column**) ENSO, (**2ⁿᵈ column**) PDO, and (**3ʳᵈ column**) AMO. Red (blue) represents a stronger (weaker) correlation (wavelet squared coherency, R_n^2). 5% significance zones against the red noise are delineated by the thick black contour lines. Arrows show the relative angular phase relationships between regional streamflow and the climate signals. Right (left) pointing arrows depict in-phase (anti-phase) relationship. Vertically upward (downward) arrows depict a lead of 90° or one-quarter (270° or three-quarter) between the climate signal and regional streamflow.

31

2.4.2. Concurrence of Shifts and the Climate Signals

Further analyses revealed that the number of stations with significant shifts over the study period experienced oscillating patterns – a series of positive shifts followed by a series of negative shifts, especially in the higher DSs (Appendix 2.D). This finding led the researchers to hypothesize that shifts can be explained better in their DSs, and such periodic behavior of shifts might be associated with large-scale climate signals since such signals also show periodic behavior with multiple frequency components. Hence, the study identified the regions that showed significant shifts during the coupled phases of the climate signals (Appendix 2.D). The regions of NE, MA, GL, OH, UMS, SRR, MO, and PN (shown as hatched regions in Figure 2.1) were found to experience significant shifts either at one or multiple coupled phases of the climate signals. To determine the variance of streamflow in each of these regions across multiple CSs, CWT was applied to the individual regional time series. CWT was also applied to each of the climate signals to determine their variance across the CSs (Appendix 2.D). Then using WTC, which is a complex conjugation of two individual CWTs, the correlation between the regional streamflow and the climate signals were quantified across the CSs (Figures 2.3 and 2.4) – where the higher power (wavelet squared coherency, R_n^2) in the WTC spectrum represented a higher correlation between the two time series. The relative phase relationships, which represent the lag-response behavior between regional streamflow and climate signals, across the CSs, were also plotted using arrows in the figures.

2.4.3. Correlation between regional streamflow and climate signals

The WTC analyses between regional streamflow and the climate signals revealed that each of the regions experienced a significantly different association with the climate signals. The

32

differences observed were found to be high even among adjacent regions. Correlation or the wavelet squared coherency ($0 \leq R_n^2 \leq 1.0$) was calculated based on Torrence and Webster (1999). All regions showed a high correlation (0.7 to ~ 1.0) with ENSO in CS8 to CS16. Regions, such as NE, SRR, MO, and PN showed a higher correlation (0.8 to ~1.0) with ENSO across the entire study period in the higher CSs. The correlations were found to strengthen after the 1990s for all the regions, as zones with higher correlations also started to show up in the lower CSs, e.g., below CS4 and between CS4 and CS8 (Figures 2.3 and 2.4). PDO showed a relatively higher correlation (0.8 to ~1.0) with the eastern regions, e.g., NE, MA, GL, and OH, compared to the central and western regions. MA and OH showed a higher correlation (0.9 to ~ 1.0) with PDO beyond CS16 across the entire study period. A higher correlation was also observed in the lower CSs for some regions; though the zones of significant correlation were observed to be of longer duration in the higher CSs (Figures 2.3 and 2.4). AMO showed intermittent zones of higher correlation (0.7 to ~ 1.0) with all of the regions at multiple intervals during the study period. Most of the significant zones with higher correlation (0.8 to ~ 1.0) were found between in CS2 and CS4 or between CS4 and CS8. MA, OH, and PN showed higher correlations (0.9 to ~ 1.0) with AMO across the entire study period beyond CS16 (Figures 2.3 and 2.4).
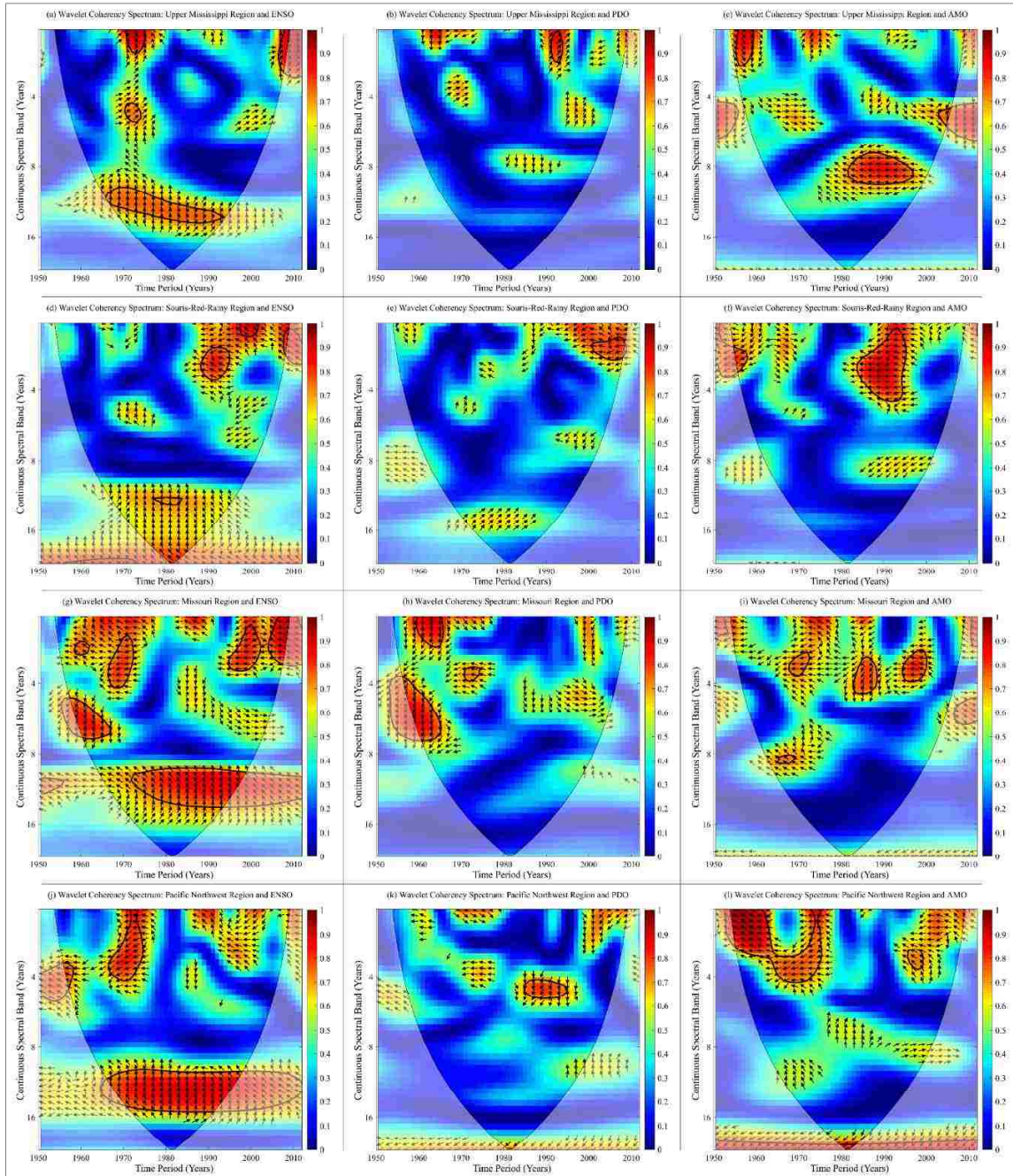
Figure 2. 4: Wavelet coherence spectra between regional streamflow of (**1st row**) Upper Mississippi, (**2nd row**) Souris-Red-Rainy, (**3rd row**) Missouri, and (**4th row**) Pacific Northwest and the climate signals of (**1st column**) ENSO, (**2nd column**) PDO, and (**3rd column**) AMO. Red (blue) represents a stronger (weaker) correlation (wavelet squared coherency, R_n^2). 5% significance zones against the red noise are delineated by the thick black contour lines. Arrows show the relative angular phase relationships between regional streamflow and the climate signals. Right (left) pointing arrows depict in-phase (anti-phase) relationship. Vertically upward (downward) arrows depict a lead of 90° or one-quarter (270° or three-quarter) between the climate signal and regional streamflow.

34

The relative phase relationships, represented by the arrows in the WTC power spectra, suggested that the lag-response behavior between regional streamflow patterns and ENSO were more consistent, compared to the phase relationships between regional streamflow and PDO/AMO. In cases of ENSO, the majority of the significant zones with higher correlations either showed an in-phase relationship (arrows pointing right) or a 90° difference (arrows pointing straight up). A 90° difference meant ENSO led the streamflow variation by a quarter, which is equivalent to six months to four years, depending on the CS of interest. The angular phase relationships between regional streamflow and PDO/AMO did not show any noticeable patterns, as they were found to be in opposing phases even within significant CSs bands.

2.4.4. Short-term prediction using data-driven models

Short-term (one step ahead) prediction using ANN, SVM, and GPR (preceded by WT) required determination of statistically independent inputs to avoid overfitting and to minimize autocorrelation. Hence, PCA was conducted for the selected regions. MA, MO, and PN were selected as the regions to be tested since these regions showed significant association with the climate signals across multiple SBs as was discussed in the previous section. Moreover, these three regions also represent the eastern, central, and western regions, respectively, of the conterminous United States. As shown in Figure 2.1, each time series was decomposed using DWT to obtain three details (i.e., DS2, DS4, and DS8) and the final approximation (i.e., AC3). Hence, the regional streamflow patterns were represented by four discretized sub-series. Similarly, each of the climate signals was also decomposed using DWT and four sub-series from each of the climate signals were obtained. Therefore, a total of 16 possible inputs (four from the regional streamflow and four from each of the climate signals) were obtained. Using PCA,

35

statistically independent inputs (orthogonally transformed features) were obtained. The results of PCA for MA, MO, and PN are shown in Figure A2.E1.

Once the optimum number of inputs, which are statistically independent of each other, was determined for each of the regions, the most efficient number of hidden neurons, which produced the least error, were selected based on the guidelines provided by Belayneh et al. (2016). The effect of hidden neurons on the model performances for the regions MA, MO, and PN are provided in Figure A2.E2. Figure A2.E3 shows the optimized ANN model architecture for the selected regions. The optimum number of inputs (statistically independent features) for MA, MO, and PN was found to be 11, 12, and 11, respectively. The most efficient number of hidden neurons for these three regions were found to be three, seven, and two, respectively. For MO and PN, seven and two were selected as the most efficient number of hidden neurons instead of 14 and 17 (which suggested least error) since even with seven and two neurons, the errors were comparable up to three decimal places with the errors obtained using 14 and 17 neurons as can be seen from Figures A2.E2b and A2.E2c. The optimum ANN model architecture for each of the selected regions also showed the optimum delayed response (lag-response relationship) of the outputs as compared to the inputs.

As mentioned in the methodology section, the input data were divided into two segments. The first segment contained data from 1951 to 2000 (a total of 50 years). The second segment contained data from 2001 to 2012. The first segment was used for training and validation (which involved adjustments of the model parameters) of the models, while the second segment was used for testing (with unseen data). Two approaches were tested to validate the models: (i) with a 20% random sampling and (ii) with K-fold cross-validation (with 5 folds). Results of training and validation using a 20% random sampling are provided in Figure A2.E4 for the three selected

regions. Results of the K-fold cross-validation are provided in Figures A2.E5 to A2.E13. Validation with both the approaches was found to be quite satisfactory with R^2 (coefficient of determination) close to or higher than 0.90 in almost every fold. Similar to ANN, K-fold cross-validation was also adopted with several SVM and GPR models. The pooled results of K-fold cross-validation (using 5 folds) are tabulated in Tables A2.E1 to A2.E3. Comparison among the various SVM models suggested that quadratic SVM produced the best training and validation performance, while comparison among the various GPR models suggested that Matern 5/2 produced the best training and validation performance. Hence, the quadratic SVM and Matern 5/2 GPR were selected to be evaluated in the testing phase with unseen data as inputs.

Once the training and validation phases were completed, testing with the unseen data was employed. In this phase, the unseen data (i.e., from 2001 to 2012) were tested with one step ahead prediction at every simulation (run). The performances of the testing phases are shown in Figures 2.5 to 2.7. The performances of SVM, GPR, and ANN, preceded by PCA and WT, were found to highly comparable. In all the cases, the fitted models predicted with significant accuracy (with R^2 above 0.90).

To test the accuracy of several learning algorithms available with the ANN models in MATLAB 2018a, a further comparison was made in the testing phase among 17 learning algorithms. For both MA and MO, Bayesian regularization backpropagation produced the best result, while for PN, cyclical order weight/bias training produced the best result. The performances of all the algorithms are provided in Tables A2.E4 to A2.E6. Three performance ratings, namely, Nash-Sutcliffe efficiency, percent bias, and RMSE-observations standard deviation ratio, were determined based on Moriasi et al. (2007). The results indicated 'good' to 'very good' performance ratings in all the cases.

37
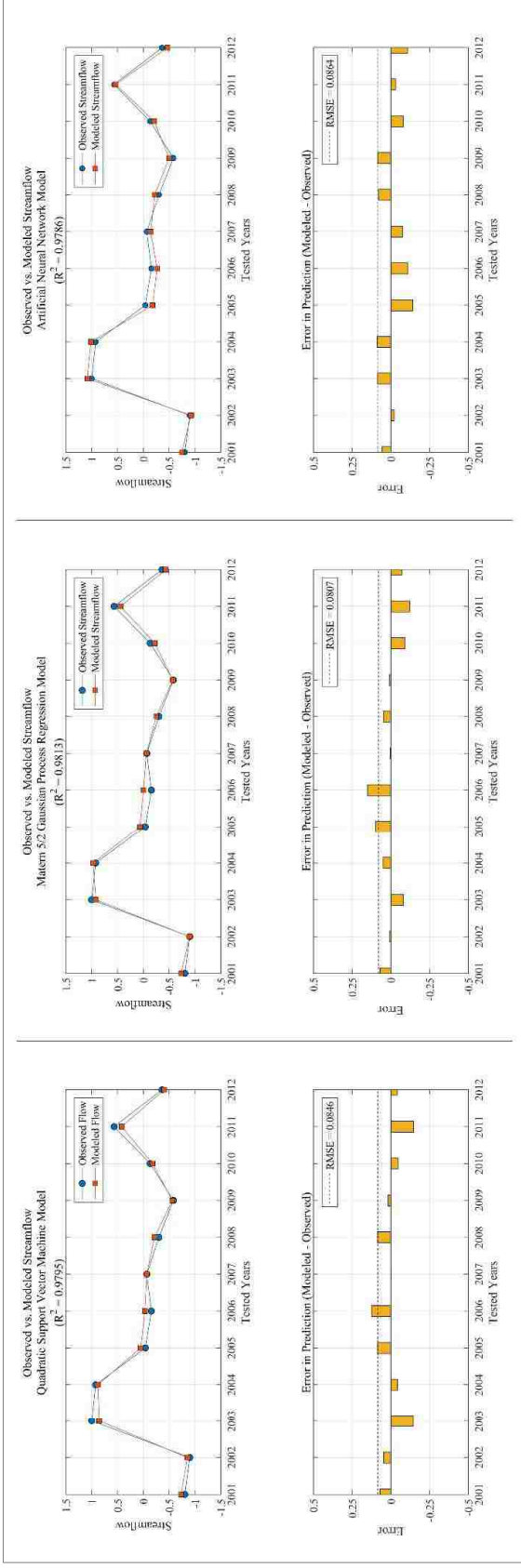
Figure 2. 5: Comparison among model performances during the testing phase (unseen data) with (**left**) quadratic support vector machine, (**middle**) Matern 5/2 Gaussian process regression, and (**right**) artificial neural network model with the Bayesian regularization backpropagation algorithm for the Mid-Atlantics (MA) region.
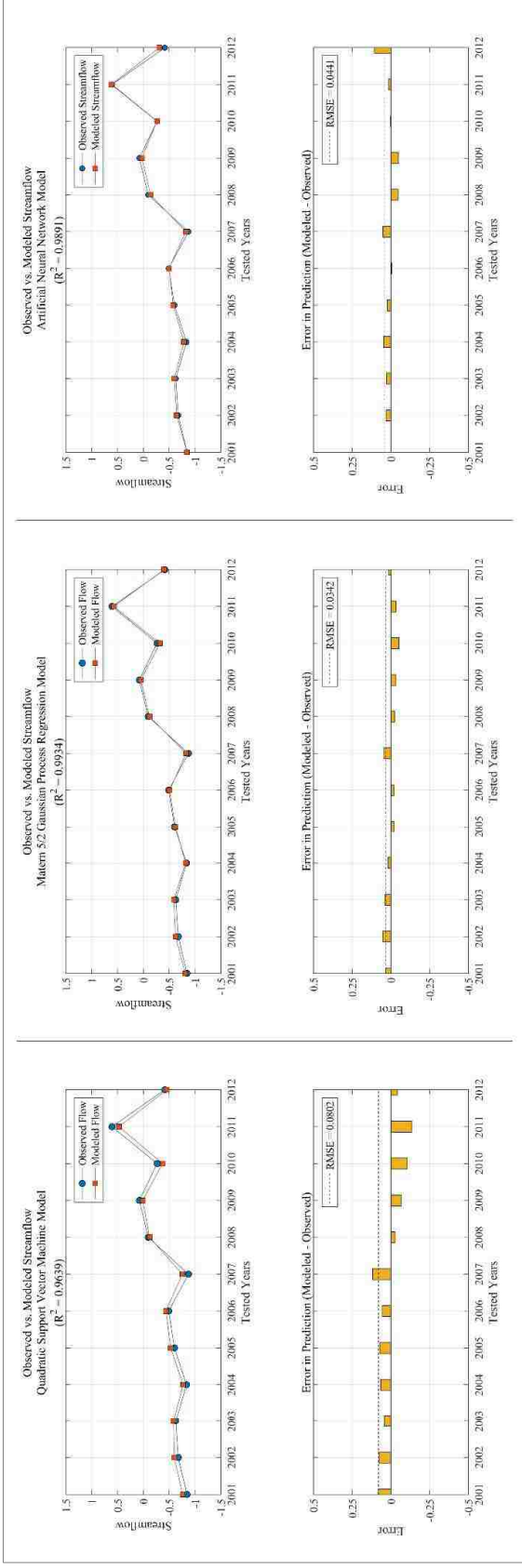
Figure 2. 6: Comparison among model performances during the testing phase (unseen data) with (**left**) quadratic support vector machine, (**middle**) Matern 5/2 Gaussian process regression, and (**right**) artificial neural network model with the Bayesian regularization backpropagation algorithm for the Missouri (MO) region.

39
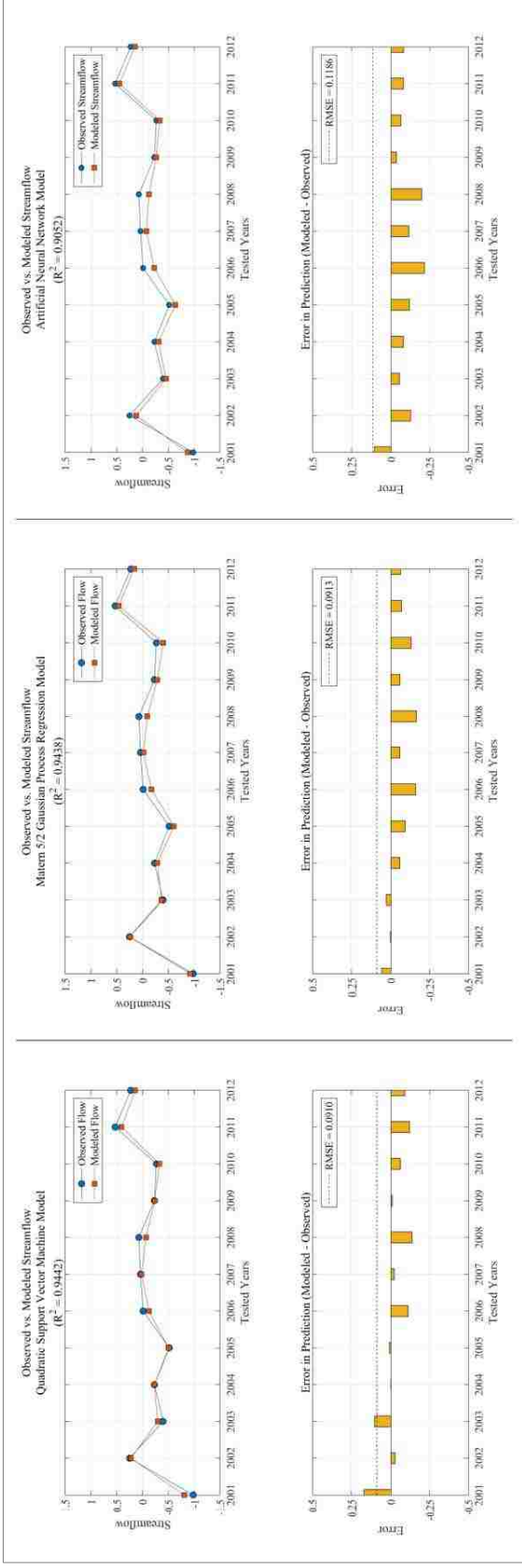
Figure 2. 7: Comparison among model performances during the testing phase (unseen data) with (**left**) quadratic support vector machine, (**middle**) Matern 5/2 Gaussian process regression, and (**right**) artificial neural network model with the cyclical order weight/bias training algorithm for the Pacific Northwest (PN) region.

2.5. Discussion

The original water year and its DSs (Figure 2.2) showed a tendency of having either the positive or negative trends within a region, except for a few central regions where both directional trends were present in close vicinity. The generic patterns of trends and shifts were found to be consistent with previous studies (Sagarika et al., 2014; Tamaddun et al., 2016). A strong coherence in the regional flow behavior was observed across the DSs as well. Smith et al. (1998) indicated that WTs, besides explaining the underlying trends, also provide important insight into the variability and mechanisms of river systems. The current analyses found an increase in the number of stations with trends as the DSs went higher. Noting such behavior of trends may help in understanding the periodic nature of the associated streams. Moreover, the strengthening of trends in higher DSs validates the need for the analysis approach adopted in this study. Though a single station on each stream was selected to avoid spatial bias, results suggest that the directions of trends were usually consistent within a hydrologic region. Assessing multiple stations on a single stream may provide a better understanding of the accompanying river system.

Compared to trends, stations with shifts were more spatially dispersed across the regions (Figure 2.2). Though the locations and directions of shifts were found to be similar to trends in general, a significant number of stations with shifts were found in the central and southern U.S., which was not observed with trends. Similar to trends, the number of stations with shifts also increased as the DSs went higher. Consistency between the trend and shift spatial patterns was observed, even though the former occurs over a long period of time, while the latter indicates an abrupt change. Villarini et al. (2009) determined the direction of trends before and after a shift and found that shifts can strengthen, weaken, or neutralize an existing trend – this explains why

trends and shifts may have a similar spatial pattern. Moreover, the number of shift points across the study period showed an oscillatory alternating pattern in the higher DSs, especially in DS8 (Appendix 2.D) – this behavior was hypothesized to be associated with the climate signals in their SBs and was later evaluated using WTC analyses.

The seasonal analyses revealed a similarity in the spatial patterns of trends and shifts, between fall (winter) and summer (spring) (Appendix 2.C) – which indicated a behavioral change at the end of fall (the beginning of winter) and at the end of spring (the beginning of summer). Like water year, the number of stations with trends and shifts in each season also increased as the DSs went higher. Similar to McCabe and Wolock (2015), this study also found seasonal flows to have strong coherence in terms of trend direction within each region, except for a few central regions where both directional trends and shifts were found in the same season. The change in seasonal trends and shifts can be attributed to the variation in temperature, precipitation, evapotranspiration, and contributions from snow and ice, as suggested by Dettinger and Diaz (2000) and Hamlet et al. (2005). The observed trends and shifts also became stronger as the DSs went higher. Such behavior can be the result of variability in lags (lags in response to large-scale climate variability) that affect seasonal flow behavior (Dettinger and Diaz, 2000). Regions with both directional trends and shifts require further investigation to understand the mechanisms of the conveying river(s).

The multi-resolution trend and shift analyses, discussed so far, suggest the following: (a) more stations of significance as the DSs went higher; (b) concurrence of shift years with the coupled phases of climate signals; (c) tendency of periodic shifts in the higher DSs (Appendix 2.D). Hence, the study hypothesized that such behavior may be attributed to the association between streamflow and the climate signals at their frequency components. Previous studies

exploring large-scale climate signals and their teleconnections, such as the studies by Redmond and Koch (1991) and Kahya and Dracup (1993), suggested a strong correlation between ENSO and the streamflow patterns of the northwestern, northeastern, and north-central regions, which confirm the findings of the current study. McCabe et al. (2007) analyzed the Upper Colorado River Basin (UCRB) flows and concluded that the UCRB flow behavior is associated with several oceanic signals – among them, North Atlantic Ocean has the highest influence. Though the current study did not include any station from the UCRB, a unique association, with significant variation in correlation, was observed between the river basins (hydrologic regions) and each of the climate signals. Stewart et al. (2005) concluded that the variance in streamflow in snowmelt-dominated regions, e.g., western U.S., is highly associated with the phases of PDO. The current study found that ENSO and AMO influence the western regions, e.g., GB and especially PN, even more strongly compared to PDO. Analyzing the world's largest rivers and documenting reasonable physical mechanisms of the oceanic-atmospheric systems, Labat (2008) emphasized the need for WT-based analyses, as attempted in the study, to investigate the teleconnection between climate signals and the hydro-climatological variables. Similar to the current study, Tootle et al. (2005) also found significant coherence between AMO and the eastern U.S. streamflow patterns. Hence, the study made an effort to better explain the associations observed in the previous studies by evaluating coherency in the most significant SBs.

The results showed that ENSO had a higher correlation, compared to PDO and AMO, with the selected regions during the study period across the SBs. For a few regions, the correlations were found to be significantly high ($R_n^2 \sim 1.0$) in certain CS bands, even across the entire study period. This was also observed with the other two climate signals, but with ENSO,

the presence of such higher correlation was more frequent (Figures 2.3 and 2.4). The results also indicated that ENSO had a higher correlation with all the regions, irrespective of their geographic locations in the higher CSs, while AMO had a higher correlation with most of the regions in the lower CSs. Even though PDO originates from the Pacific Ocean, which is located on the west of the U.S., it showed a higher correlation with the eastern regions of the United States. For both PDO and AMO, it is possible that significantly higher correlations were present beyond CS16, as suggested by a few regions since both of these signals oscillate over a decadal to a multi-decadal scale.

The spatiotemporal association between regional streamflow patterns and the climate signals across the CSs, along with their relative phase relationships, may help in understanding some of the physical relationships that were not completely explained in the previous studies. The current study found significantly high correlations between regional streamflow patterns and climate signals in their decomposed time series, which supports the initial hypothesis of the study that such an association can be better explained in their frequency components. The variations in the associations between streamflow patterns and climate signals may help explain some of the unique local phenomena. Regional climate (streamflow) modelers, working on the concepts of lag/lead time approach as a function of large-scale climate variability, may also find the results useful.

Comparison among the ANN, SVM, and GPR models, preceded by PCA and WT suggested comparable results both in the training and validation phase as well as in the testing with unseen data phase. Among the SVM models, quadratic SVM was found to be producing the best results in all the cases tested in the study, while Matern 5/2 was found to be the best performer among the tested GPR models. The ANN models were found to be highly sensitive to

the number of hidden neurons in the model architecture in terms of the model's performance. Bayesian regularization backpropagation learning algorithm, among the other 17 algorithms tested, was found to be producing consistently good results for all the three cases tested in the study. The delayed response (lag-response relationship) of the outputs with respect to the inputs observed in the ANN models were found to be comparable with the lags obtained from the WTC analyses between the climate signals and regional streamflow patterns.

2.6. Conclusions

The study analyzed water year and seasonal trends and shifts (along with their DSs) in 237 unimpaired streamflow stations across the continental U.S. from 1951 to 2012. The spatiotemporal association between regional streamflow patterns and three large-scale climate signals were assessed using WTC. The major findings, some of which confirm the findings of previous works discussed earlier, and the summary results of the study are listed below:

- Positive (negative) trends and shifts in the water year and its DSs were significant in the northeastern and north-central (northwestern and southeastern) regions.

- A few central regions showed both directional trends and shifts – which was not common since most of the regions showed spatial coherency in terms of the trend and shift direction.

- Seasonal trends and shifts suggested unique spatial patterns in the original time series as well as in their DSs. Fall and spring showed the highest positive and negative trends and shifts, respectively, suggesting a behavioral change at the end of these two seasons.

- The number of significant stations with trends and shifts increased as the DSs went higher, with the maximum in DS8. Shifts showed an oscillating behavior in DS8 – which

led to the hypothesis that such behavior at higher SBs was correlated to the frequency components of the climate signals.

- ENSO showed a higher correlation with the regional streamflow in CS8 to CS16, while both PDO and AMO showed higher correlations in the lower CSs (below CS4) and beyond CS16.

- The relative phase relationship suggested a uniform lag-response behavior (either in-phase or a lag of one quarter) between significant regional streamflow patterns and ENSO. For PDO and AMO, no such consistency was observed.

- Comparison among ANN, SVM, and GPR models, preceded by PCA and WT, produced comparable results with significant accuracy in short-term prediction of regional streamflow behavior.

Data availability restricted the current study to analyze with high certainty (or adequate resolution) beyond DS8 for DWT and beyond CS16 for WTC. Decomposing to higher SBs can be helpful in associating streamflow variations with climate signals having multidecadal frequency components. In addition, working with a higher number of stations with longer records may provide a better explanation of the regional change patterns. Considering these limitations, the study attempted to provide an in-depth analysis of the continental U.S. streamflow in response to large-scale climate signals in order to help improve the current understanding of the oceanic-atmospheric systems and their underlying teleconnections with regional streamflow patterns. The multi-resolution associations observed in the study may help improve forecasting models, which may lead to better estimation and regulation of regional flows.

CHAPTER 3: MULTI-SCALE CORRELATION BETWEEN THE WESTERN U.S. SNOW WATER EQUIVALENT AND LARGE-SCALE CLIMATE VARIABILITY OF THE PACIFIC OCEAN

3.1. Introduction

Snow water equivalent (SWE) is a common measurement of the snowpack. According to the Natural Resources Conservation Service (NRCS), SWE refers to the amount of water that is "... *contained within the snowpack ...*". SWE can be thought of as the theoretical depth of water resulting from an instantaneous melting of the entire snowpack. Hence, snowpack in terms of SWE is considered a vital source of runoff in the water supply system across North America (Hunter et al., 2006; McCabe and Dettinger, 2002). The relative contributions of snowpack to water yield are much greater in the mountainous regions of the western United States (U.S.) than many other regions of the country. In these regions, approximately 50%-70% of the annual precipitation falls as snow, and is stored during the winter as snowpack (Palmer, 1988; Serreze et al., 1999); eventually, it affects the runoff of the succeeding seasons. The beginning of April is the time when snow courses attain maximum SWE. The 1 April SWE is used extensively in the western U.S. as an estimate to forecast the spring-summer runoff, and ultimately can be used to predict the annual runoff behavior in the surrounding regions. Understanding the relationships among the factors influencing SWE could be beneficial to forecasters and water managers dealing with critical infrastructure management and irrigation practices (Hunter et al., 2006).

Previous studies have examined the relationship between long-term climate variability and the western U.S. snowpack accumulation using various datasets. Cayan (1996) used snow course data of 60 years from 11 western U.S. states and observed significant anomalies in SWE

across spatial and topographical variations in the western U.S. mountainous regions. The study also found that precipitation had a much higher influence on SWE compared to temperature, which only influenced low-altitude stations. A study by McCabe and Legates (1995) analyzed atmospheric circulation and spatiotemporal patterns of snowpack accumulation in the western U.S. using 700-hectopascal (hPa) height anomalies and 1 April snowpack measurements over a study period of 40 years. They found a strong negative correlation between the variables studied. Another study found that 1 April SWE showed more than a 100% coefficient of variance, which was comparable with variation in seasonal precipitation patterns in some of the western states (Changnon et al., 1991). The study also suggested that snow course records could be used as a regional climate indicator of snow accumulation during the spring in the Rocky Mountains.

Besides analyzing the direct influence of climate on the western U.S. snowpack, studies have examined the role of major climate indices on the hydrology of the western United States (Kahya and Dracup, 1993; Carrier et al., 2016; Pathak et al., 2018). The El Niño Southern Oscillation (ENSO) and the Pacific Decadal Oscillation (PDO), both resulting from the Pacific Ocean, are considered to be two of the major large-scale oceanic-atmospheric climate signals that affect the western U.S. hydrology (Barnett et al., 1999; Beebee and Manga, 2004; Sagarika et al., 2015). Shifts in pressure cell locations and changes in their intensities cause trade winds to get stronger or weaker. This results in changes in the locations and velocities of oceanic currents – both of these cause upwelling of colder water from the bottom of the ocean, and move warmer ocean-surface-water in specific directions, for example, east or west near the equator in the case of ENSO. Hence, sea-surface temperature (SST) fluctuations in multiple locations of the Pacific Ocean are initiated. The variations in pressure cells, coupled with the SST fluctuations, affect the direction, movement, and productivity of the storm tracks by affecting rates of oceanic

evaporation and atmospheric moisture content. ENSO, a natural cycle observed in the eastern Pacific Ocean with a periodicity of two to seven years, alternates between two distinct phases, El Niño (positive or warm phase) and La Niña (negative or cold phase) (Redmond and Koch, 1991). PDO, which occurs on a timescale of 25 to 50 years, originates from the North Pacific Ocean, has a larger zone of influence compared to ENSO (Trenberth and Fasullo, 2007). Similar to ENSO, PDO also varies between warm and cold phases. Studies observing climate indices have also emphasized the teleconnection between the oceanic climate systems and the global hydrologic processes (Coscarelli et al., 2013; Sagarika et al., 2016). SST fluctuation alters the availability of moisture from the oceanic surface currents and eventually affects the formation of storm systems. Hence, SST fluctuations have the potential to influence hydro-climatological variables such as precipitation, snowpack, streamflow, runoff, and soil moisture.

Time series associated with hydro-climatological variables are complex in nature, as they are nonlinear and usually do not follow a normal probability distribution (Jevrejeva et al., 2003). Several studies have focused on understanding the change patterns and frequencies (periodicities) of such time series (Cheo, 2016; Tamaddun et al., 2016). Among the various methods for analyzing non-normal distributions having complex periodicities, wavelet transforms (WTs) have been suggested as useful tools to extract information from a complex time series (Lau and Weng, 1995). WTs determine the most significant frequencies influencing a time series while simultaneously preserving the time dimension (Percival and Walden, 2000). The history, classification, and theory of WTs can be found in the works of David and Rajasekaran (2009) and Torrence and Compo (1998).

Considering the advantages of using WT (Yiou et al., 2000), in order to observe variability in data, this study adopted the concept of continuous wavelet transform (CWT), a

49

method used for feature extraction (Foufoula-Georgiou and Kumar, 1995). To understand how two time series are correlated, concepts of cross wavelet transform (XWT) and wavelet coherency (WTC) were adopted. Details regarding XWT and WTC can be found in Tang et al. (2014) and Torrence and Webster (1999). Previous studies examining the relationship of ENSO and PDO to the western U.S. precipitation mostly have focused on winter precipitation in particular rather than on snowpack. Since water from snowpack is the most significant water resource for many western U.S. river systems, SWE is selected as the primary focus of this study. Data were utilized from 323 Snow Telemetry (SNOTEL) sites (stations) of the western U.S. for a study period of 56 years covering 1961 to 2016. This record length is a major extension in terms of the number of stations and the length of data analyzed, compared to previous studies using similar datasets. CWT was used to observe the variability in data, and XWT and WTC were used to illustrate and quantify, respectively, the high common power (association) between the representative time series of the variables. Such an approach has not been used previously with SWE data. This study also compared the association of ENSO/PDO across the western U.S. hydrologic regions, which broadened the scope of the study since the results can be beneficial to regional water managers as well.

3.2. Study Area and Data

The SNOTEL online database of NRCS (http://www.wcc.nrcs.usda.gov/snow/) contains 1 April SWE data for the western United States. The website combines the SNOTEL data, obtained from telemetry systems, and snow course data, obtained from manual snow measurements. NRCS uses several meteor burst communications technology (existing from about 50 to 75 miles above the earth), e.g., radio wave communications, cellular model, satellite, and line of sight, to collect and disseminate data, which are recorded every 15 minutes. Data

were obtained from 323 western U.S. SNOTEL stations from 1961 to 2016, a total of 56 years. Figure 3.1 (bottom left) shows the SNOTEL stations in each state of the western United States. Figure 3.1 (right) shows the stations in each of the six hydrologic regions representing the western United States; these regions are delineated by United States Geological Survey (USGS) in their hydrologic unit map (http://water.usgs.gov/GIS/regions.html).
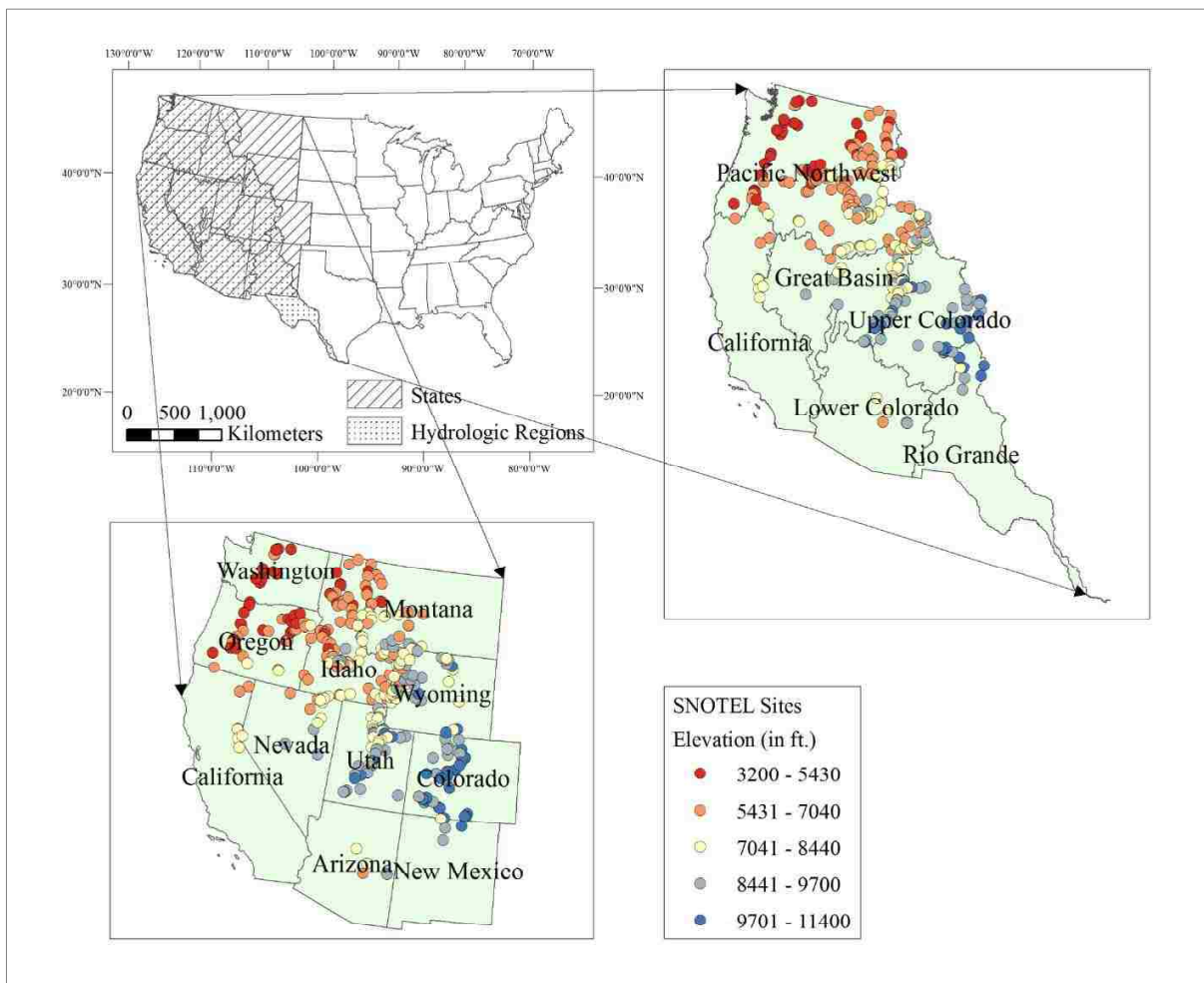
Figure 3. 1: (**Bottom left**) Map showing states of the western U.S. and the 323 SNOTEL stations selected for this study. (**Right**) Map showing the spatial distribution of 258 SNOTEL stations across the hydrologic regions representing the western United States.

The selected regions were Pacific Northwest (PN), California (CA), Great Basin (GB), Lower Colorado (LC), Upper Colorado (UC), and Rio Grande (RG). Out of the 323 stations chosen for the study, 258 stations were found to be in these six hydrologic regions (Table 3.1).

ENSO (NIÑO 3.4) and PDO indices were obtained for the same historical period as SWE. ENSO was represented by the December-January-February (DJF) mean. Two different PDO indices were considered for the analyses. PDO1 represented the DJF mean; while PDO2 represented the October to March (Oct-Mar) mean. ENSO and PDO data were accessed through the online databases of the U.S. National Oceanic and Atmospheric Administration (NOAA) and the Joint Institute for the Study of the Atmosphere and Ocean (JISAO), respectively. Positive and negative indices refer to the warm and cold phases, respectively, for both ENSO and PDO. The analyses were conducted with a monthly lead-time approach, e.g., the DJF (Oct-Mar) means of ENSO/PDO1 (PDO2) of 2015-2016 were used against the 1 April SWE of 2016, which resulted in pre-lagged time series.

Table 3. 1: The number of SNOTEL sites in each hydrologic region along with the average elevation (in ft.) of the sites, the standard deviation of the elevation (in ft.) in a particular region, and the percentage of variance explained by the first principal component (PC1) for that region. The values are rounded to the nearest whole number.

Hydrologic Region	Number of SNOTEL Sites	Average Elevation (ft.)	Std. Dev. Of Elevation (ft.)	% SWE Variance Explained by the PC1
Pacific Northwest (PN)	144	6204	1324	65%
California (CA)	5	6641	1200	79%
Lower Colorado (LC)	6	8261	1032	78%
Great Basin (GB)	46	8322	928	64%
Upper Colorado (UC)	49	9324	883	60%
Rio Grande (RG)	8	9749	795	80%
Total	258			

3.3. Methodology

The following sections contain brief descriptions of CWT, XWT, and WTC, based on the works of Grinsted et al. (2004) and Tang et al. (2014). For further details on the application of WT in the various fields of hydrology as well as for the mathematical formulations, readers may refer to Jevrejeva et al. (2003), Torrence and Compo (1998) and Torrence and Webster (1999).

The analyses process adopted in this study are as follows: first, each of the time-series dataset (in their standardized form) was decomposed using CWT, which showed the variability in the data, represented by the wavelet power spectrum. Second, XWTs were constructed using individual CWTs obtained from the first step. The XWTs illustrated the covariance between the time series involved. Third, significant correlations were determined using WTC, which quantified the correlation using the Monte Carlo approach. All the analyses were conducted using the programming platform MATLAB. Each step and the methods used are described in the following sub-sections.

3.3.1. Observation of Variance in the Data

CWT showed the variability of a time-series dataset at multiple frequency bands across the time period to understand the periodic nature of the time series (if present) (Foufoula-Georgiou and Kumar, 1995). Out of the many wavelet functions, the Morlet wavelet function has been considered to be the most appropriate one for geophysical signal processing (Percival and Walden, 2000), and therefore was chosen for the current study. The first principal component (PC1), referred to as 'SWE1' in the following sections – obtained from a principal component analysis (PCA) using the MATLAB routine – was chosen to represent the variability of data from the 323 stations. This PC1 explained 52% variability of all the stations. For each hydrologic

region, a similar approach was adopted where the PC1 of each region represented the variability

of the respective region as shown in Table 3.1.

3.3.2. Detection of Covariance between Time-Series

The formation of an XWT, obtained from a complex conjugation of two CWTs, revealed

the high common power (covariance) and the relative phase relationship of the two time series in

the time-frequency domain (Grinsted et al., 2004). The relative phase angle provided information

regarding the lag-response behavior between the two time series in the time-frequency domain

(Jevrejeva et al., 2003). The statistical significance of covariance between two time series was

determined against a red noise background (Torrence and Compo, 1998).

3.3.3. Quantification of correlation between time-series

Besides showing significant common frequency bands at different time intervals, WTC

quantified the correlation between the two time series. Unlike XWT, WTC was capable of

determining significant coherency at low common power. In this study, the Monte Carlo

approach (Wallace et al., 1993) was adopted to calculate significant wavelet coherence at a

significance level of 5% against the red noise. Details about how to calculate significance levels

against red noise can be found in the works of Torrence and Compo (1998).

3.4. Results

Figure 3.2 contains the individual CWTs that explain the variability in data, using a

wavelet power spectrum and a global wavelet spectrum. Figure 3.3 shows the XWTs and WTCs

between SWE1 and ENSO/PDO. Figures 3.4 and 3.5 show the WTCs between the regional SWE

and ENSO and the regional SWE and PDO, respectively, for each of the hydrologic regions. The

edge effects, shown by the cone of influence (COI) in the XWTs and WTCs, represent the region of reliability. Since wavelets are not completely localized in time and need to be padded with zero, the results within the COI are more reliable (Grinsted et al., 2004).

3.4.1. Variability (High Power) of Data in SWE1 and ENSO/PDO

From the standardized time series of SWE1 (Figure 3.2a), it was observed that SWE across the western U.S. experienced large fluctuations during the study period. The wavelet power spectrum (Figure 3.2a) generated from the CWT showed higher variability with significance around the 2-year band in 1963, in the 2-to-3-year band from 2008 to 2013, in the 3-to-5-year band from 1974 to 1982, and in the 11-to-15-year band from 1973 to 2011. The significant variability observed in the 11-to-14-year band showed the highest power in the wavelet power spectrum. This was also observed in the global wavelet spectrum, which showed a spike near the 11-to-14-year band.

The wavelet power spectrum (Figure 3.2b) resulting from the CWT of ENSO showed the presence of a few discrete but significant intervals during the study period. Significant variability was observed in the 2-to-4-year band from 1995 to 2000 and from 2008 to 2012, in the 3-to-4-year band from 1969 to 1971, in the 3-to-6-year band from 1977 to 2007, and in the 11-to-13-year band from 1990 to 2011. The highest power was observed in the 3-to-6-year band. In addition, the global wavelet spectrum picked higher power in the 3-to-6-year band and around the 11-to-13-year band.
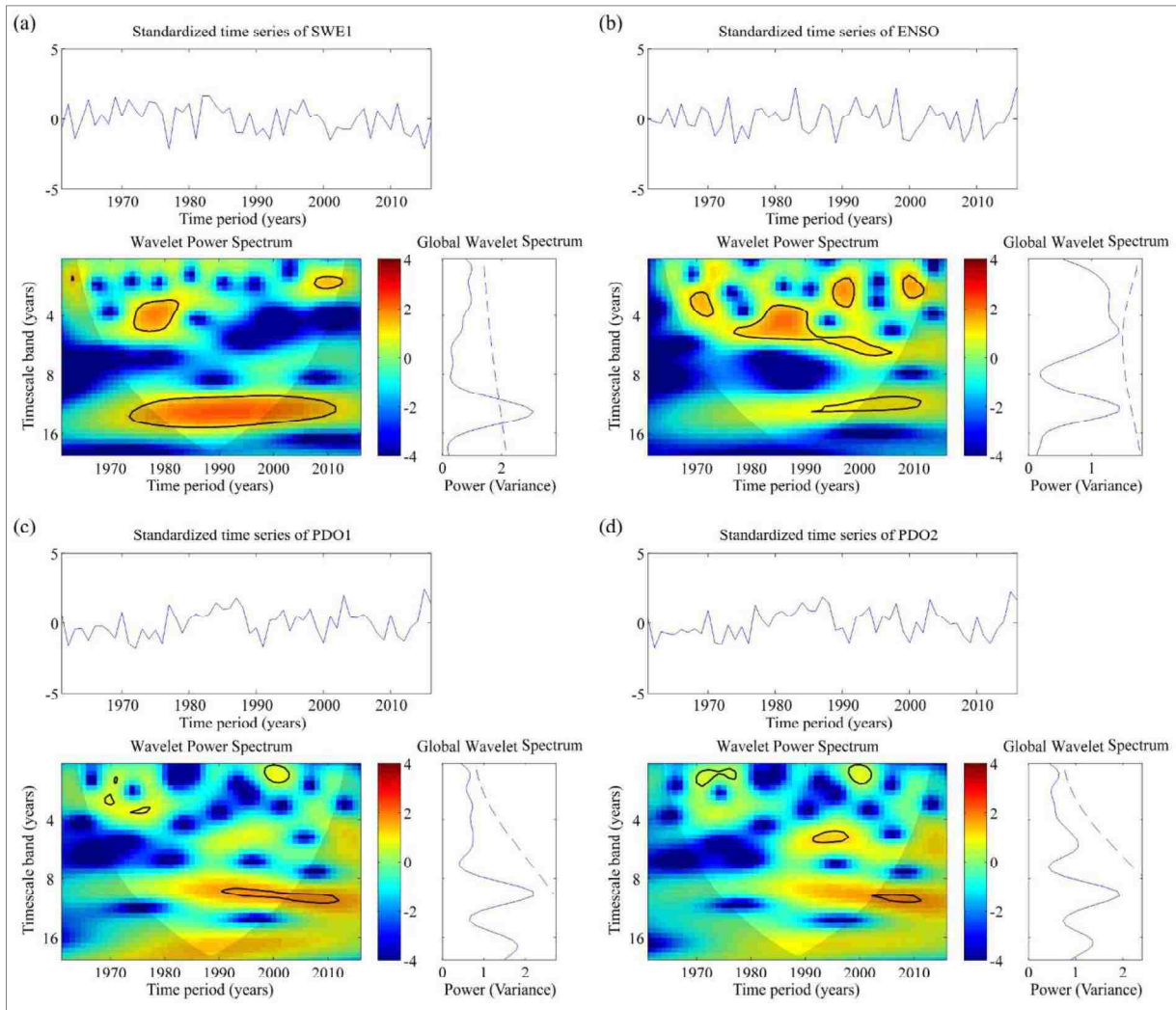
Figure 3. 2: Standardized time series, wavelet power spectra, and global wavelet power spectra of **a**) SWE1, **b**) ENSO, **c**) PDO1, and **d**) PDO2. Red (blue) represents stronger (weaker) power. The thick black contour line marks the 5% significance level against red noise.

56

PDO1 and PDO2 both showed similar bands of significance across the study period (Figures 3.2c and 3.2d). Significant high power was observed in the 2-to-4-year band from 1968 to 1977, in the 2-to-3-year band from 1997 to 2002, and in the 8-to-10-year band from 1990 to 2011 (from 2003 to 2013 in PDO2). PDO2 also showed the presence of significantly high power in the 5-to-6-year band from 1991 to 1998. PDO1 showed high power in this band as well but was not found to be significant. Global wavelet spectra picked the higher power around the 8-to-10-year band for both PDO1 and PDO2. The PDO2 global spectrum showed a small peak near the 5-to-6-year band. Both PDO1 and PDO2 showed higher power above the 16-year band, which were observed in the wavelet power spectra and global wavelet spectra; however, they were not found to be significant. Comparison among the independent datasets, i.e., SWE1, ENSO, and PDO, showed that there is considerable overlap in terms of the time and frequency of their higher variability zones. To detect their common power or covariance, XWT was applied between SWE1 and ENSO, SWE1 and PDO1, and SWE1 and PDO2.

3.4.2. Covariance (High Common Power) between SWE1 and ENSO/PDO

The XWT between ENSO and SWE1 (Figure 3.3a) showed presence of significantly high common power in the 2-to-3-year band from 1973 to 1977, from 1994 to 2000, and from 2007 to 2012, in the 3-to-6-year band from 1968 to 1985, in the 5-to-7-year band from 2001 to 2012, and in the 10-to-15-year band from 1973 to 2012. The relative phase relationship between the two time series is shown by the arrows in the XWT power spectrum. Except for a significant period from 2007 to 2012 in the 2-to-3-year band, all the other timescale bands across different time intervals had arrows pointing towards the right. A rightward (leftward) arrow indicates an in-phase (anti-phase) relationship between the two time series. Figure 3.3a indicates that during the study period, an in-phase relationship between ENSO and SWE1 was dominant, which suggests

57

they were moving in the same direction at the same time. The arrows in the significant intervals showed a tendency of pointing upwards, indicating a lag between ENSO and SWE1. A vertical upward-pointing arrow meant that ENSO led SWE1 by 90° or one-quarter (six months to 4 years depending on the timescale band). Whereas, a vertical downward-pointing arrow indicates a lag of 270° or three-quarter (18 months to 12 years depending on the timescale). As it takes time for the atmosphere to adjust and for storm tracks to redirect and change their productivity, the detected lead reasonably aligns with the currently-understood physical mechanism.

From the XWT between PDO1 and SWE1, high common power was observed around the 3-year band from 1962 to 1965, in the 2-to-3-year band from 1971 to 1979 and from 1997 to 2004, in the 5-to-7-year band from 2009 to 2012, and in the 9-to-12-year band from 1989 to 2010 (Figure 3.3b). High common power in the 12-to-16-year band (and beyond) was present from 1975 to 1995 but was not found to be statistically significant. The arrows indicating a phase relationship were mostly observed to be pointing right (indicating an in-phase relationship), except for an interval from 1962 to 1965. The presence of arrows that had a tendency of pointing upwards suggested that PDO1 led the SWE1 in many instances.

The results suggested that the phase relationship between PDO1 and SWE1 was not consistent or uniform, as the direction of the arrows varied across the study period. The XWT of PDO2 and SWE1 did not reveal any new information as they were quite identical in terms of the location of significant covariance and relative phase relationships. Hence, those results have not been reported in the manuscript.
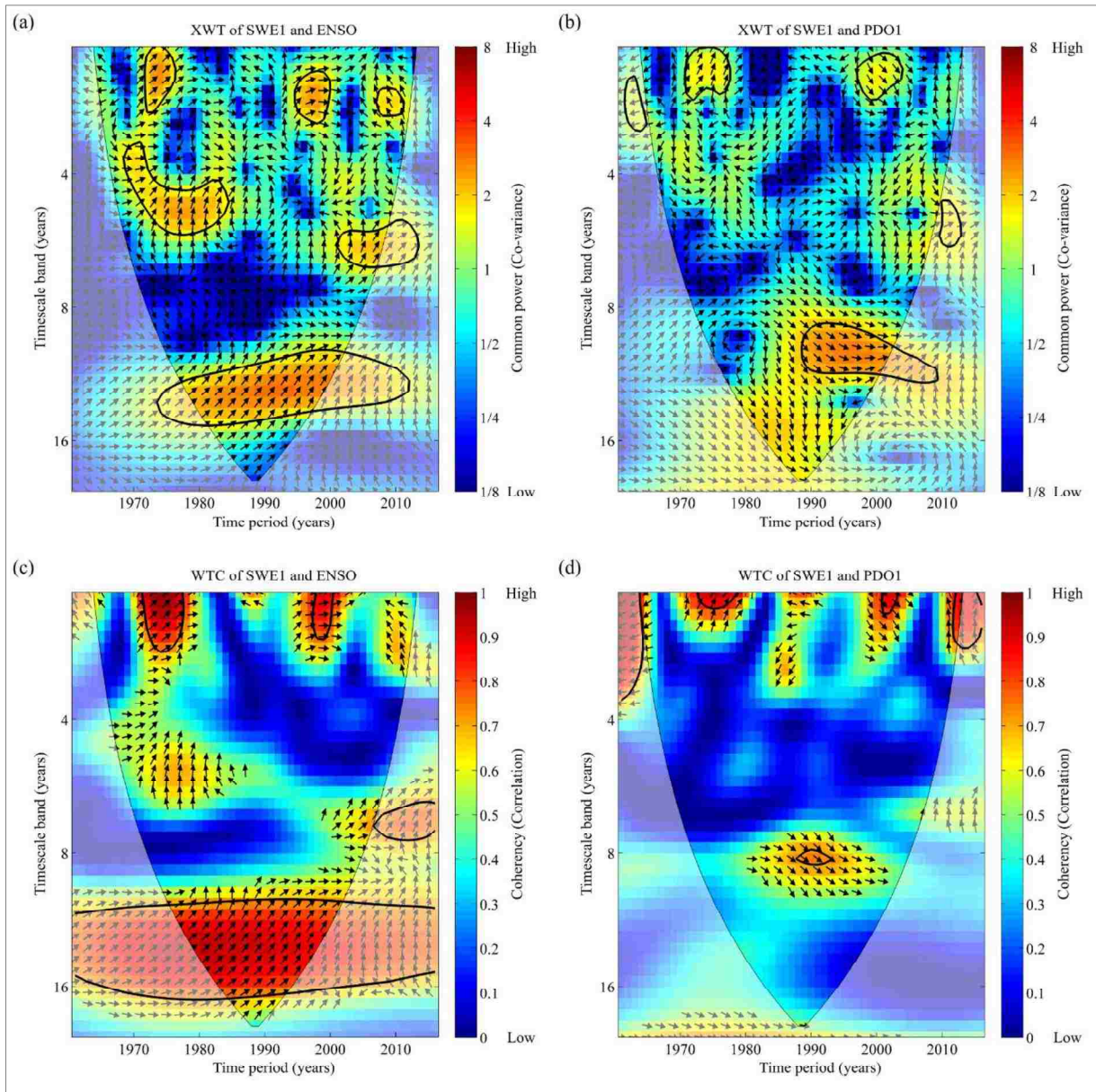
Figure 3. 3: Cross wavelet spectra between **a**) SWE1 and ENSO and **b**) SWE1 and PDO1. Wavelet coherence spectrum between **c**) SWE1 and ENSO and **d**) SWE1 and PDO1. The thick black contour line delineates a 5% significance level against red noise. Red (blue) represents stronger (weaker) power. The COI, which potentially could distort the picture around the edges, is shown by lighter shades. The arrows represent the relative phase relationship between the two time series. Right (left) pointing arrows show an in-phase (anti-phase) relationship, while vertically upward (downward) arrows show that ENSO/ PDO1 leads SWE1 by 90° or one-quarter (270° or three-quarter).

3.4.3. Coherency (Significant Correlation) between SWE1 and ENSO/PDO

The WTC between ENSO and SWE1 showed the presence of high correlation in the 10-to-16-year band throughout the entire study period, i.e., 1961 to 2016 (Figure 3.3c). Correlations varied from 0.8-to-1.0 in this continuous zone. At the significance level chosen in this study (5% against the red noise), a correlation of 0.7 was considered to be significantly high. Correlations as high as 1.0 also was observed in the lower bands, e.g., in the 2-3-year band from 1971 to 1979 and from 1998 to 2001. High correlation values, in the range of 0.7-to-0.8, were observed in the 6-to-8-year band from 2007 to 2016. Instances of high correlation – in the range of 0.6-to-0.7 – were observed at multiple intervals across the study period, especially in the 4-to-6-year band; however, they were not found to be statistically significant against the red noise using the Monte Carlo approach. The arrows, during the significant intervals, were all observed to point towards the right, indicating an in-phase relationship between ENSO and SWE1. In addition, arrows were observed to show a higher tendency to point upwards, especially from 2000 to 2016. The results indicated that ENSO led SWE1 by a phase angle of as high as 90°. Results also indicated that an increase (decrease) in the ENSO index caused an increase (decrease) in SWE1 across significant intervals with high correlation.

The WTC between PDO1 and SWE1 (Figure 3.3d) did not show the presence of a continuous significant band as it was observed in the WTC between ENSO and SWE1. PDO1 and SWE1 were found to be highly correlated in the lower bands, mostly below the 4-year band. The highest correlation – in the range of 0.8-to-1.0 – was observed in the 2-to-3-year band from 1972 to 1979, from 2001 to 2003, from 2011 to 2016, and in the 2-to-4-year band from 1961 to 1964. A high correlation in the range of 0.7-to-0.8 was observed in the 8-to-10-year band from 1988 to 1994. There were instances of higher correlation in the range of 0.6-to-0.8 in the 2-to-3-

year band, in the 6-to-8-year band, and beyond the 16-year band; however, they were not found to be statistically significant. The arrows were observed to point towards the right, except for a significant interval from 1961 to 1964. There were instances where arrows pointed vertically up, which indicated that PDO1 led SWE1 by a phase angle of 90°. In a few instances, the arrows pointed slightly downward. The results suggest that PDO1 and SWE1 changed simultaneously in some of the significant intervals where PDO1 led SWE1, though the relative phase relationships were not consistent or uniform. The WTC of PDO2 and SWE1 (not shown here) did not reveal any new information – in fact, the WTC of PDO2 and SWE1 was found to be quite identical to the WTC of SWE1 and PDO1.

3.4.4. Coherency (Significant Correlation) between regional SWE and ENSO/PDO

Similar to the WTC between ENSO and SWE1, WTCs between ENSO and the regional SWEs revealed the presence of higher correlation across the entire study period for PN and CA in the 8-to-16-year band (Figure 3.4). Unlike SWE1, GB and UC showed the presence of higher correlation (as high as approximately 1.0) of longer duration (at multiple intervals from 1961 to 2000) in the lower timescale bands (below and around the 4-year band). LC and RG showed a similar pattern of correlation with ENSO as was observed with SWE1, though the regional correlation bands showed less duration and lower correlation values. The relative phase relationships across different regions were observed to vary significantly. The direction of the arrows did not show any recognizable pattern, though the arrows in the significant zone of a particular region were observed to be showing the tendency of pointing towards the same direction.
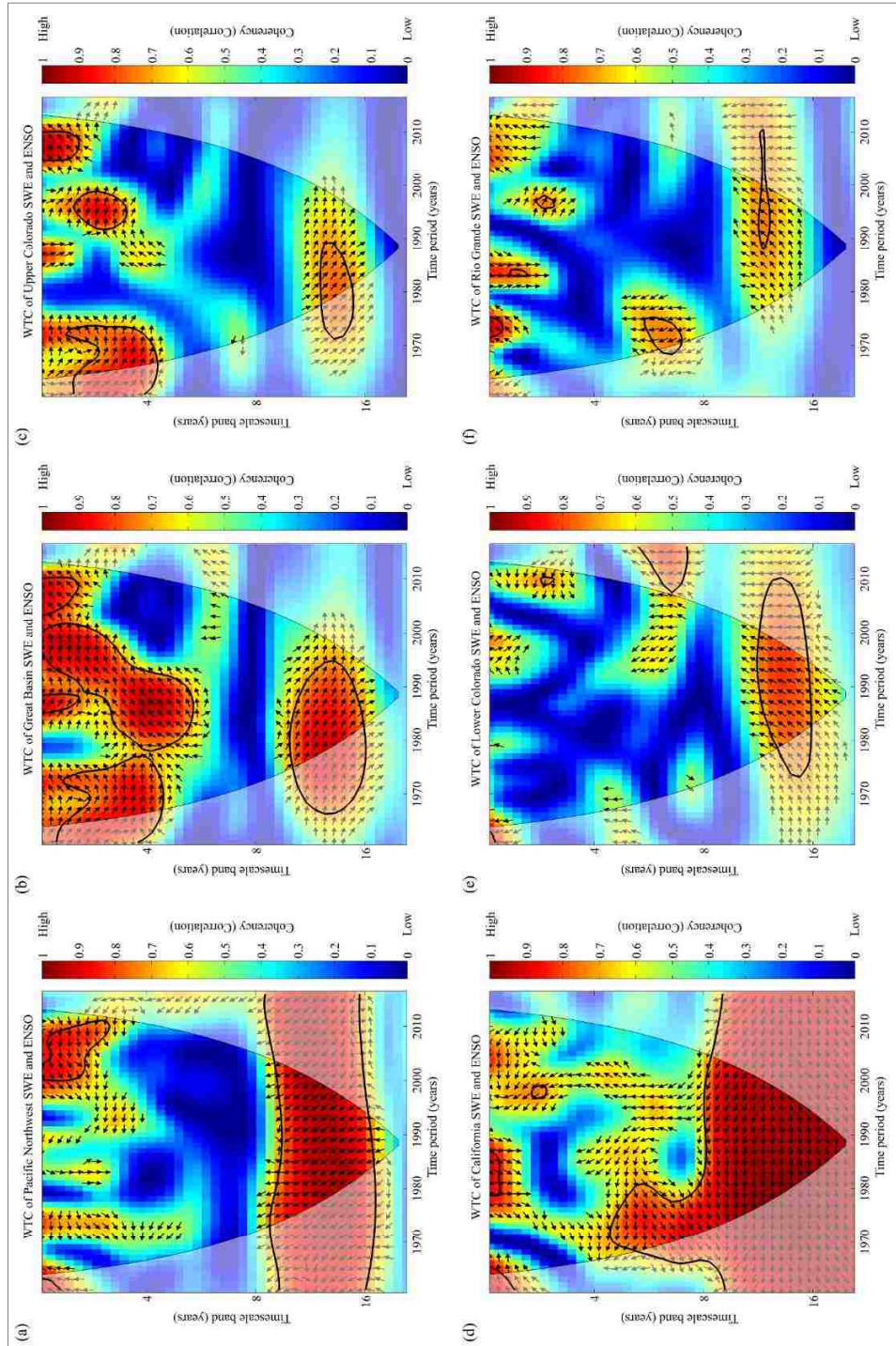
Figure 3. 4: Wavelet coherence spectra between regional SWE and ENSO for **a**) Pacific Northwest, **b**) Great Basin, **c**) Upper Colorado, **d**) California, **e**) Lower Colorado, and **f**) Rio Grande. The thick black contour line delineates a 5% significance level against red noise. Red (blue) represents stronger (weaker) power. The COI, which potentially could distort the picture around the edges, is shown by lighter shades. The arrows represent the relative phase relationship between the two time series. Right (left) pointing arrows show an in-phase (anti-phase) relationship, while vertically upward (downward) arrows show that ENSO leads the respective regional SWE by 90° or one-quarter (270° three-quarter).

WTCs between PDO1 and the regional SWEs of GB, UC, and RG showed a similar pattern (Figure 3.5) to what was observed in the WTC between PDO1 and SWE1. PN showed much higher correlation compared to any other region in the lower timescale bands (in the 2-to-4-year and 4-to-6-year band) at multiple intervals. The presence of high correlation – as high as approximately 1.0 – was observed in the 2-to-6-year band from 2010 to 2016 in PN. CA and LC showed the presence of higher correlation of significant intervals (from 1970 to 1988, from 1973 to 1982, and from 1990 to 2000) around the 4-year and 8-year bands, which were not observed with SWE1. The relative phase relationships were observed to vary across the regions without showing any recognizable pattern. GB, UC, and RG did not show much presence of higher correlation. Regions with a lower elevation of stations and close to the ocean, e.g., PN, CA, and GB, were observed to show a higher correlation with both ENSO and PDO1 compared to the regions with a higher elevation of stations and far from the ocean (inland), e.g., UC and RG (Figures 3.1, 3.4, and 3.5).
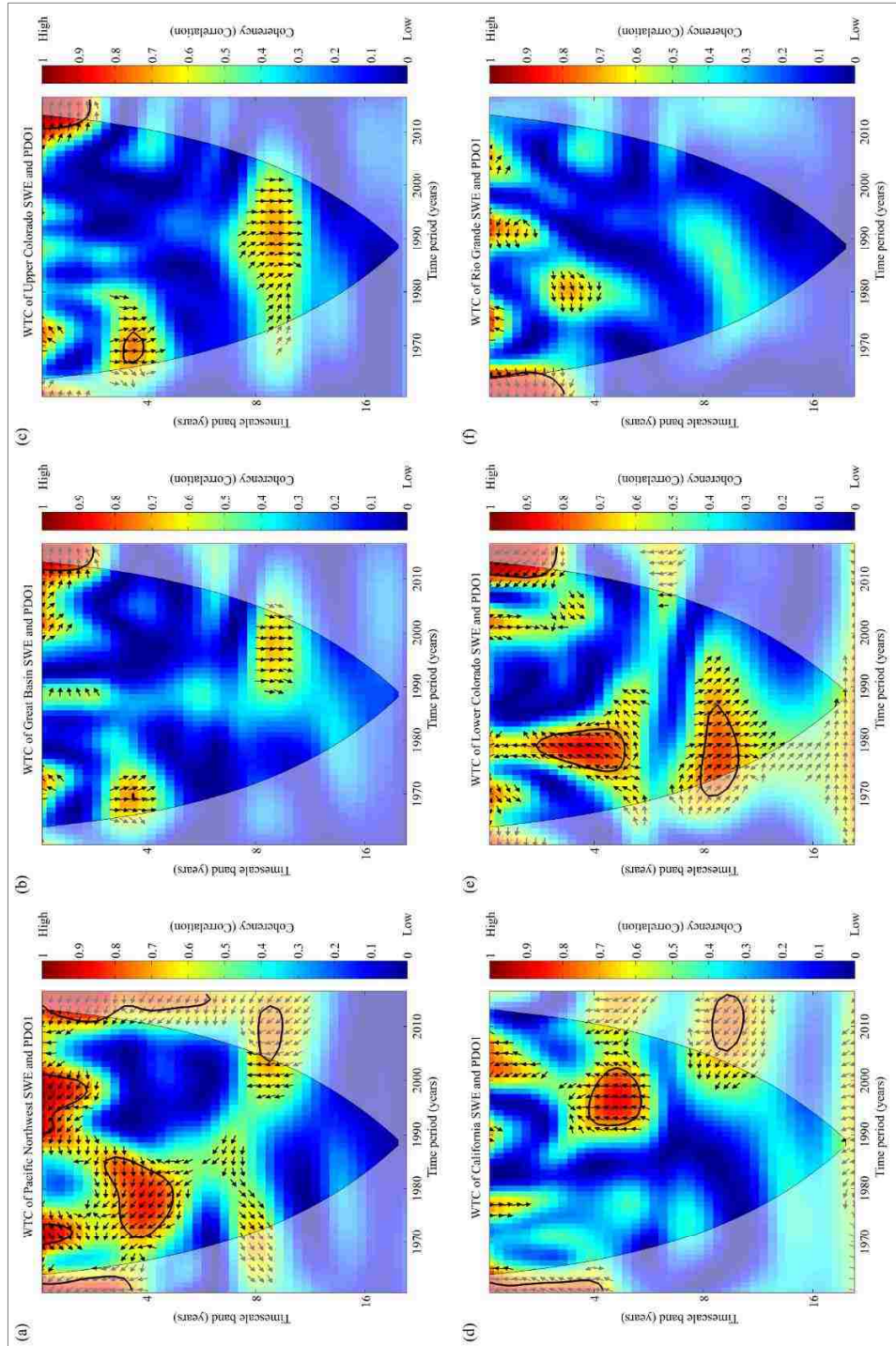
Figure 3. 5: Wavelet coherence spectra between regional SWE and PDO1 for **a**) Pacific Northwest, **b**) Great Basin, **c**) Upper Colorado, **d**) California, **e**) Lower Colorado, and **f**) Rio Grande. The thick black contour line delineates a 5% significance level against red noise. Red (blue) represents stronger (weaker) power. The COI, which potentially could distort the picture around the edges, is shown by lighter shades. The arrows represent the relative phase relationship between the two time series. Right (left) pointing arrows show an in-phase (anti-phase) relationship, while vertically upward (downward) arrows show that PDO1 leads the respective regional SWE by 90° or one-quarter (270° three-quarter).

3.5. Discussion

From the CWT analyses, it was observed that SWE1 had the highest variability in the 11-to-15-year band during a significantly longer duration, from 1973 to 2011 (Figure 3.2a); however, the power was observed to reduce gradually near both the tails of the time series, suggesting less variation during those intervals; the results near the ends of a wavelet power spectrum are also less reliable due to the effect of COI (Grinsted et al., 2004). In addition, there was the presence of higher variability in the lower bands, but of much less duration. It can be inferred from these results that SWE in the western U.S. experienced the highest variation every 11-15 years. A similar pattern of high power was observed across the study period in the ENSO CWT (Figure 3.2b). Although the duration of significant variability was less in the ENSO CWT – from 1990 to 2011 – the entire study period showed high variability in the 10-to-16-year band. Moreover, the patterns observed in the time-frequency power spectrum were similar in the higher bands for SWE1 and ENSO CWTs (Figures 3.2a and 3.2b). ENSO showed the highest variability in the 3-to-6-year band, which may be attributed to the frequency of the ENSO cycle (Bayazit, 2015). Both PDO1 and PDO2 showed the highest variability in the 8-to-10-year band and also beyond the 16-year band; although bands beyond the 16-year were not found to be statistically significant. The tendency of showing variability in the higher bands could be explained by the decadal nature of PDO cycle (Trenberth and Fasullo, 2007). The results indicated overlaps in the time-frequency spectra of SWE1 and ENSO/PDO variability across the study period, especially in the higher bands.

The XWT between ENSO and SWE1 had the highest covariance in the 10-to-15-year band from 1973 to 2012 (Figure 3.3a). This was inferred from their individual CWTs. The results showed high common power in the 3-to-6-year and the 5-to-7-year bands. The relative phase

relationship showed that ENSO led SWE1 in all the significant intervals at different frequency bands. The arrows also suggested that in the majority of the cases, the change in SWE1 and ENSO were in-phase, suggesting a simultaneous change. Hence, it can be interpreted that change in the ENSO index, with a certain lag, caused SWE to change in the same direction across the western U.S. over a long duration.

The XWT between PDO1 and SWE1 revealed that these two time series experienced the highest covariance in the 9-to-12-year band and beyond the 16-year band (Figure 3.3b); although, the bands beyond the 16-year were not found to be statistically significant. PDO2 had similar results as PDO1. The relative phase relationship between PDO1 and SWE1 was not found to be as uniform as ENSO and SWE1. The lag-response behavior of PDO1 and SWE1 did not show any particular pattern. There were instances where PDO1 led SWE with opposing arrows suggesting in-phase and anti-phase relationships in the same frequency band. It was not possible to make any conclusions about the phase relationship of PDO1 and SWE1 from the obtained results. There were certain intervals in the 8-to-12-year band and in the 2-to-3-year band where both ENSO and PDO1 were observed to show high covariance with SWE1; however, the duration of intervals in the lower bands was much less compared to the higher bands.

The results of ENSO and SWE1 WTC revealed that the most significant timescale band influencing the two time series was the 10-to-16-year band. The entire study period was found to be significant in that particular frequency band. Lower bands, e.g.., the 2-to-3-year and the 6-to-8-year bands, also showed a high correlation (Figure 3.3c); although the durations were not found to exceed 10 years in any of the instances. A high correlation was observed in the 4-to-6-year band as well but was not statistically significant. There was much similarity between the

XWT and the WTC of ENSO and SWE1, except for the presence of a continuous zone in the 10-to-16-year band that lasted across the entire study period observed in the WTC. Correlation in certain intervals – e.g., all of the 10-to-16-year and in some 2-to-3-year band – was as high as approximately 1.0. This suggested a direct relationship between ENSO and the western U.S. SWE. The relative phase relationship suggested that ENSO led SWE1 by certain lag; in many cases, they both changed simultaneously in the same direction. This relationship also was observed in the XWT analysis of SWE1 and ENSO.

The WTC between PDO1 and SWE1 did not show much presence of significant intervals across the study period (Figure 3.3d). PDO2 had similar results as PDO1. There were intervals of high correlation – as high as approximately 1.0 – in the lower bands (below the 4-year band); however, the duration of the intervals was not found to be more than 7 years in any of the instances. The 8-to-9-year band showed the presence of high correlation, in the range of 0.7-to-0.8; though, the duration was only a few years. Bands beyond the 16-year also showed the presence of high correlation but were not found to be significant.

The comparison between the two WTCs revealed that ENSO and PDO were both correlated to SWE1 only in the lower timescale bands (below the 4-year band). The results revealed that ENSO had a much higher correlation with SWE1 than did PDO throughout the study period. The results obtained in the study supports the findings of Beebee and Manga (2004), who studied the relationship of ENSO and PDO with the runoff generated from snowmelt in the state of Oregon and found ENSO to have a higher correlation than PDO.

The WTCs obtained from ENSO/PDO1 and the regional SWEs suggested significant variation in terms of their association at various timescales across the study period (Figures 3.4

and 3.5). The regional analyses suggested that even though ENSO/PDO1 was correlated with SWE1 in certain timescale bands across the study period, the individual hydrologic regions experienced a unique association with both ENSO and PDO1. Hydrologic regions comprising of PN, GB, and CA showed a much higher correlation with ENSO compared to the other regions. PN was found to be most significantly correlated with PDO1. Also, it was noted that the regions having stations at lower elevations (Figure 3.1) had a higher correlation (stronger association) compared to the regions with stations at a higher elevation. Besides the effect of elevation, such outcome may also be the result of other factors such as the number of stations per region, the percentage of data variability explained by the PC1, and the spatial location of the region (close to the ocean or inland). Studies suggest that the elevation of the basins, which is sensitive to both air temperature and precipitation, also affect the accumulation of snow and the timing of snowmelt (Cayan, 1996; Dudley, 2017). Analyses of the individual stations within a region can provide a better explanation of the effect of elevation on the observed correlation.

The current analysis did not calculate the exact time lag between ENSO/PDO and SWE from the relative phase relationship indicated in the wavelet power spectra though the results showed that both the indices, especially ENSO, had a uniform lagged relationship with the western U.S. SWE. ENSO, and in some cases PDO, was found to be leading SWE by a few months to close to a decade. Cayan et al. (1999) and Hanson et al. (2004) studied these lag-response behaviors and concluded that the major reasons causing these lags were the cumulative effects of the nature of oceanic-atmospheric fluctuations, the formation and dynamics of winds, and the time required for the formation and melting of snow. Some studies (Trenberth and Hurrell, 1994; Pozo-Vázquez et al., 2001) investigated these lags between climate indices and surface hydrology and found delays from a few months to a few years. Since a lead-time

approach was adopted (the time series were pre-lagged) in this study – e.g., DJF mean of ENSO/PDO and 1 April SWE – the underlying lag expressed by a 90° phase difference did not exactly express a quarterly lag (six months to 4 years depending on the timescale band), rather expressed a lag of slightly higher duration.

The presence of the high correlation in the 10-to-16-year band between ENSO and the western U.S. SWE suggests that they both changed in the same direction (with certain lags) across the entire study period. The presence of such temporal relationship may be attributed to the frequency of the ENSO cycles. On the other hand, PDO was not found to be highly correlated with SWE except for a few short intervals. The results suggested the presence of higher association beyond the 16-year band in PDO; however, they were not found to be statistically significant. It should be noted that phases of PDO change over multiple decades; therefore, it is possible that timescales at higher bands may have higher correlations with SWE. Since this study analyzed timescales up to the 16-year band only, significant intervals at higher timescales may have been missed. The current study did not analyze beyond the 16-year band since the results beyond this band had high uncertainty due to the limitation of the length of the period of record. Analyzing a longer-reconstructed time series may allow evaluating the associations at higher timescales with greater certainty. The findings of the current analyses may result in future research to help better understand the lag-response behavior between the climate indices and SWE at each timescale band. Additionally, the sites (stations) within a particular hydrologic region may be analyzed independently to evaluate the effect of topography in greater details. Methods, such as coupling of wavelet with the artificial neural network, which allows multiple inputs to understand the response of a signal, can be an option for such analysis. Understanding the relationship between other regions of the Pacific Ocean and the western U.S.

SWE can also be potential future research. Since the obtained results are purely statistical in nature, they need to be interpreted in context and with a proper understanding of wavelet power spectra before concluding any specific physical relationship.

Based on the results obtained from the analyses, the major contributions of the study are:

- Use of SNOTEL (1 April SWE) data from 323 western U.S. stations with a time period spanning 56 years: a major extension in the number of stations covered and the length of data analyzed compared to previous studies using similar datasets.
- A wavelet approach in evaluating the correlation between ENSO/PDO and the western U.S. SWE at multiple frequency bands: an approach that has not received much attention with such datasets in the documented literature.
- A hydrologic-region-based analysis to evaluate the regional change of SWE as a response to the change in ENSO/PDO: the results showed how significantly the response of SWE may vary among the adjacent regions.

3.6. Conclusions

The study examined the correlation between ENSO/PDO and the western U.S. SWE over a study period of 56 years using CWT and its derivatives. Application of such methods allowed the study to analyze and correlate regional SWE with oceanic-atmospheric climate indices across multiple timescale bands. The analysis revealed the following:

- ENSO, compared to PDO, had a much higher influence on SWE.
- The temporal associations were observed to be stronger in the higher timescale (lower frequency) bands.

- The effect of ENSO/PDO varied significantly across the adjacent hydrologic regions.

- Regions close to the ocean (inland) and lower (higher) in elevation were observed to show a higher (lower) correlation with ENSO/PDO.

The analyses conducted in this study highlighted the need to work with snow data at even finer spatial resolution since the variation in response among the adjacent regions were observed to be significantly high across the mountainous western United States. Understanding such relationship of snowpack formation and climate indices can be beneficial to climate forecasters and regional water managers.

CHAPTER 4: SPATIOTEMPORAL TREND, SHIFT, AND ENTROPY ANALYSES OF TEMPERATURE, PRECIPITATION, AND POTENTIAL EVAPORATION OF NORTH INDIAN MONSOON DURING THE ENSO PHASES

4.1. Introduction

Studies on extreme climate events, i.e., droughts and floods, across the world, have found that such extremes are likely to be associated with the anomalies in zonal sea surface temperature (SST) fluctuations observed in the oceans. In turn, these fluctuations, coupled with the changes in global and regional atmospheric pressure systems, formation of surface winds, and moisture sources & evaporative demand, cause severe changes in the temperature and precipitation patterns (Diffenbaugh et al., 2015; Seager et al., 2015). Studies also suggest that these extremes are likely being aggravated by global warming (Williams et al., 2015; Yoon et al., 2015). The recent California drought has been of great interest to many climate researchers, (e.g., Griffin and Anchukaitis, 2014; Robeson, 2015). A study by Wei et al. (2016) identified major atmospheric circulation patterns affecting precipitation in California. However, the authors indicated that the contributions from the various components of the hydrologic cycle are yet to be properly understood. As a result, besides analyzing SST anomalies and precipitation patterns, recent studies have incorporated hydro-climatological variables like moisture sources, evaporative demand, and temperature in order to understand these climate extremes more thoroughly (Shukla et al., 2015; Wei et al., 2016; Bhandari et al., 2018). In addition, various combinations of these variables have been found to show significantly different and sometimes inverse correlations with certain climate extremes. A few cases – for example, lower moisture with higher temperature – found to affect the extremes even more severely (Shukla et al., 2015).

Several studies have presented ample evidence to support that climate change has immensely intensified the hydrologic cycle (IPCC, 2013, 2014, and 2019; Carrier et al., 2016; Tamaddun et al., 2018a). This intensification has raised questions (Dirmeyer and Brubaker, 2006; Huntington, 2006; Kramer et al., 2015; Tamaddun et al., 2018b) such as, what is the distribution of this intensification across the different components of the water cycle? How do changes in the amount of precipitation affect other components? What are the consequences of these changes in climate patterns? Some researchers have suggested that increased (decreased) precipitation can cause increased (decreased) vegetation, which in turn may cause an increase (decrease) in evapotranspiration (Levis et al., 2000; Bounoua et al., 2010). Other studies have suggested that increased evapotranspiration resulting from increased vegetation may potentially affect the CO_2 concentration, which in turn can act as a cooling mechanism to reduce the temperature (Sellers et al., 1996; Guillevic et al., 2002; Bonan, 2008). These studies have shown how the dynamics among hydro-climatological variables might bring about a change in the long-term patterns and have reinforced the need for multi-variable analyses to predict and confront climate extremes (Ahmed et al., 2018; Tamaddun et al. 2019c).

Out of the many different regions of India, the northern region, named as North India in the following sections, currently is of particular interest to many climate researchers (Tiwari et al., 2016a and 2016b; Khare et al., 2016). North India is situated in the Earth's northern temperate zone (Singh, 2010), and has experienced major climate diversity over the years (Dimri, 2013; Rathore et al., 2013; Abeysingha et al., 2016). Temperatures in North India have been recorded as varying over a wide range, from below freezing temperatures in some states to over 50 °C in the deserts (Singh, 2003; Kaul, 1998; Rowell, 1980). Rainfall and snow in North India result from two major weather patterns, i.e., the western disturbances and the Indian

monsoon. The western disturbances, originating from the Atlantic Ocean as well as the Caspian and the Mediterranean Seas, are called extratropical weather phenomena; they carry moisture towards the east over North India (Datta and Gupta, 1968; Dimri, 2004; Wang, 2006). On the other hand, monsoon, a large-scale circulation pattern lasting from June through September each year, carries moisture of the humid southwest summer wind from the Indian Ocean towards the north and provides the vast majority of the annual rainfall to the entire Indian subcontinent. As a result, understanding the behavior of monsoon has been of major interest to climatologists for many years.

The India Meteorological Department (IMD) has observed and recorded monsoon patterns for several decades and has developed multiple stochastic models to forecast the initiation, recession, and strength of the Indian Summer Monsoon Rainfall (ISMR). Out of the many different factors affecting ISMR, the El Niño Southern Oscillation (ENSO) has been considered to be one of the most significant large-scale forces that influence the behavior of ISMR (Ju and Slingo, 1995; Kumar et al., 1999). ENSO is a natural cycle, represented by an index, which records the SST fluctuations originating from the strengthening and weakening of the trade winds (Tamaddun et al., 2017a and 2019b). It is observed in the tropical Pacific and affects the surrounding oceanic-atmospheric systems (Ropelewski and Halpert, 1986: Kahya and Dracup, 1993; Tamaddun et al., 2017b and 2017c). Shifts in pressure cells and changes in their intensity cause trade winds to get stronger or weaker. This results in changes in the locations and velocities of oceanic currents – both of these cause upwelling of colder water from the bottom of the ocean, and move warmer ocean-surface-water in specific directions, for example, east or west near the equator in the case of ENSO. Hence, SST fluctuations in multiple locations of the Pacific Ocean are initiated. ENSO consists of two phases, namely, El Niño, which is the warmer

74

(positive) phase, and La Niña, which is the cooler (negative) phase (Sagarika et al., 2016). Each phase can last from a few months to a year, and they occur every two to seven years. From 1950 to 2012, ISMR was found to be above average or around average in almost all the La Niña years. Contrarily, five of the most prominent droughts in India during that period coincided with the El Niño years (Kumar et al., 2006). A monsoon followed by El Niño does not necessarily result in poor rainfall all the time; however, as studies suggest, there might be other climate and weather factors, e.g., the extent of Himalayan/Eurasian snow, which influences the circulation of monsoon (Kumar et al., 1999; Tamaddun et al., 2017d). Studies have also suggested that other complementary factors to ENSO may affect ISMR, e.g., the Indian Ocean Dipole (IOD), complex coupling and dynamics of multiple variables, and variations in heat flux over different land masses (Webster and Yang, 1992; Ashok et al., 2001; Wang et al., 2005).

The tropical Indian Ocean experiences a basin-wide change after an ENSO event. In the north equatorial Indian Ocean, this change starts in late winter (early spring) and continues until summer. The prolonged influence of ENSO continues into the following seasons, and eventually causes climate anomalies in Southeast Asia, especially during summer (Yang et al., 2007; Xie et al., 2009). Analyzing the phase relationships between ENSO and ISMR, Torrence and Webster (1999) found significant correlations across several timescales, with stronger coherence during intervals of higher variance. Ashok et al. (2001) found that ENSO, along with IOD, affected the rainfall amount immensely from 1958 to 1997. Other researchers observed that IOD could reduce the effect of ENSO on ISMR based on the different phased relationships (Saji et al., 1999; Ashok et al., 2004). This explains why all the years associated with El Niño did not cause a drought in India. Krishnamurthy and Goswami (2000) found a strong correlation between inter-decadal ISMR and ENSO variations. In addition, this study explained the possible reasons for

75

major regional and equatorial circulation patterns, e.g., Hadley circulation and Walker circulation, and how their anomalies caused these variations.

Kumar et al. (2006) suggested that the SST anomalies in the central (eastern) equatorial Pacific strengthen (weaken) the likelihood of droughts during the monsoon. Other studies observed multi-scale, e.g., interannual, quasi-decadal, and decadal variations, relationships among ISMR, Indian Ocean oscillations, and the ENSO phases (Reason et al., 2000; Allan et al., 2003; Gadgil et al., 2004). Besides monsoon rain, temperature variations of the tropical Indian Ocean, along with the prolonged effects of ENSO and the associated heat flux over India, were studied by Wang et al. (2005) and Xie et al. (2009). Yang et al. (2007) concluded that El Niño not only affects SST fluctuations of the Indian Ocean but also plays an important role in the summer climate variability across the Indo-Western Pacific basins. Klein et al. (1999) found that El Niño alters the cloud cover and evaporation configuration of atmospheric circulations, which in turn affect the heat flux of the surrounding basins. Loo et al. (2015) observed major shifts in the intensity and initiation of monsoon after the 1970s, which likely were affected by anomalies in global temperature and precipitation.

Analyzing anomalies in pressure, temperature, wind, and cloud cover over the Indian Ocean in the different phases of ENSO during monsoon, Reason et al. (2000) emphasized that multi-variable analyses need to be conducted across various temporal scales, e.g., annual and seasonal, for a better understanding of the physical relationships and correlation patterns. Some combinations of the interconnected hydro-climatological variables and their extremes, such as lower precipitation levels with higher temperatures, have the potential to cause severe adversity on the hydro-ecological as well as on the socio-economic systems, even though the individual variables may not indicate extreme conditions (Mazdiyasni and AghaKouchak, 2015; Tamaddun

76

et al., 2017e). Considering the advantages of multi-variable analyses as a major motivation, the current study focused on understanding the influence of ENSO on the spatiotemporal change patterns of three hydro-climatological variables – temperature, precipitation, and potential evapotranspiration (PET) – during the monsoon season across North India. In addition, this study determined the all-year (century-wide) trend and shift patterns of the selected variables from 1901 to 2002. The Mann-Kendall test (Mann, 1945; Kendall, 1975) and Pettitt's test (Pettitt, 1979) – both nonparametric in nature – were used to detect the presence of trends and shifts, respectively. To evaluate the distribution (apportionment) of the temporal variability of the historical changes on an annual and seasonal scale, the concept of entropy was applied, which quantitatively measured the dispersion, disorder, and variability in the long-term trends (Shannon, 1948). Moreover, the study provided an extensive literature review of the relevant studies highlighting the relationships between monsoonal change patterns and the ENSO phases and applied the multi-variable analyses approach to provide insights that may explain some of the research questions discussed earlier. The obtained results may help practitioners to prepare for flood and drought risks as a response to the changes in ENSO phases. The major contributions of the study are:

- Evaluation of the long-term trend and shift patterns of temperature, precipitation, and PET across North India at various ENSO phases using non-parametric statistical tests.
- Determination of the spatiotemporal relationships between the selected variables during monsoon and at each of the monsoonal months over a century-wide period.
- Comparison between the major shift points during monsoon and the phases of ENSO, which might have resulted in extreme climate events, throughout the study period.

77

- Analyses of apportionment entropy to quantify how the detected variations were distributed temporally over the years (annually) and during the months (seasonally) of monsoon along the study area.

4.2. Study Area and Data

According to the Geological Survey of India (GSI, 2016), eight states, namely, Chandigarh, Delhi, Haryana, Himachal Pradesh, Jammu & Kashmir, Punjab, Uttarkhand, and Uttar Pradesh, officially form the northern region of India. These eight states consist of 147 districts. Appendix 4 (Table A4.1) contains the names of the individual districts in each of the states. As reported by the IMD, the monsoon or the rainy season lasts from June to September. Temperature, precipitation, and PET data were obtained from 1901 to 2002 on a monthly mean basis for 146 districts as data for one of the districts were unavailable (Figure 4.1). The data were accessed through the online database of the India Water Portal (IWP, 2016). IWP database contains data in downloadable "comma-separated values" format (more commonly known as the CSV format) after initial error correction. Later, the downloaded data were standardized by subtracting the mean and dividing by the standard deviation. Moreover, the methods used in the study (described in the next section) are resilient against outliers and missing data points, which makes them appropriate for the type of analyses adopted in the study. The trend (shift) patterns of the selected variables were evaluated during monsoon at four different combinations of the ENSO phases, namely, (1) the El Niño years, (2) the La Niña years, (3) the non-El Niño years (either the La Niña or neutral years), (4) and the non-La Niña years (either the El Niño or neutral years). The ENSO (Niño 3.4) indices used in this study (Figure 4.2) were accessed through the online database of the United States National Oceanic and Atmospheric Administration (NOAA, 2015). During the study period of 102 years, there were 37 instances that were found to be

78

neutral years, 32 years were found to be El Nino years, and 33 instances were found to be La Nina years. Hence, a total of 70 instances were non-El Niño years, while a total of 69 instances were non-La Niña years.

Besides the trend and shift patterns of the selected variables at each of the four ENSO phases mentioned earlier, the all-year trend and shift patterns during the monsoon as well as during each of the monsoonal months were evaluated. For the temperature and PET trends and shifts, the monthly mean of the monsoon and of each of the monsoonal months was analyzed. For precipitation, the monthly totals were used. The annual and seasonal apportionment entropy were evaluated using the annual data – the sum of all the monthly means, and the seasonal data – the monthly means of each of the monsoonal months.
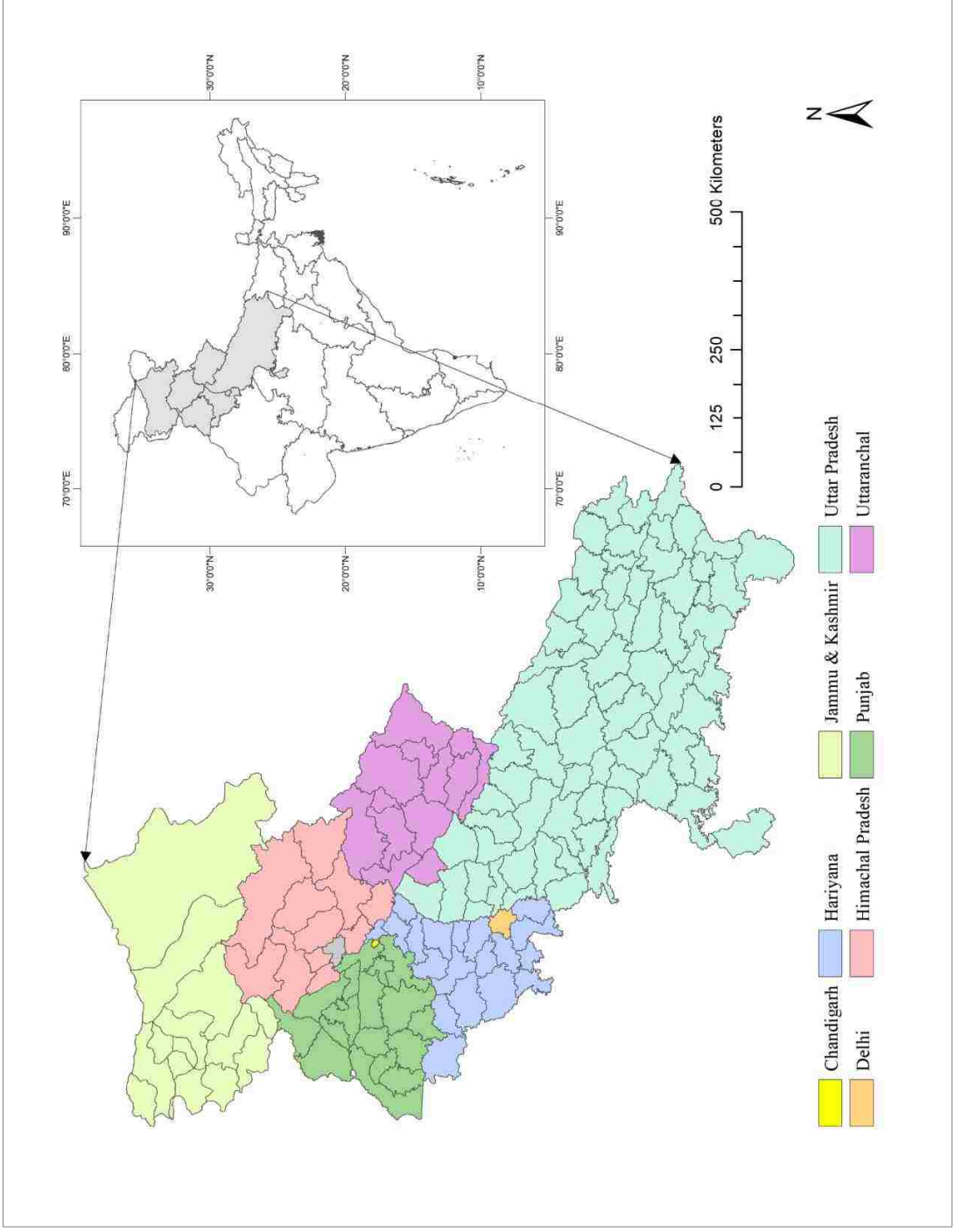
Figure 4. 1: Map showing the selected states representing North India and the constituent districts (data for the gray-shaded district in Himachal Pradesh were unavailable).

80
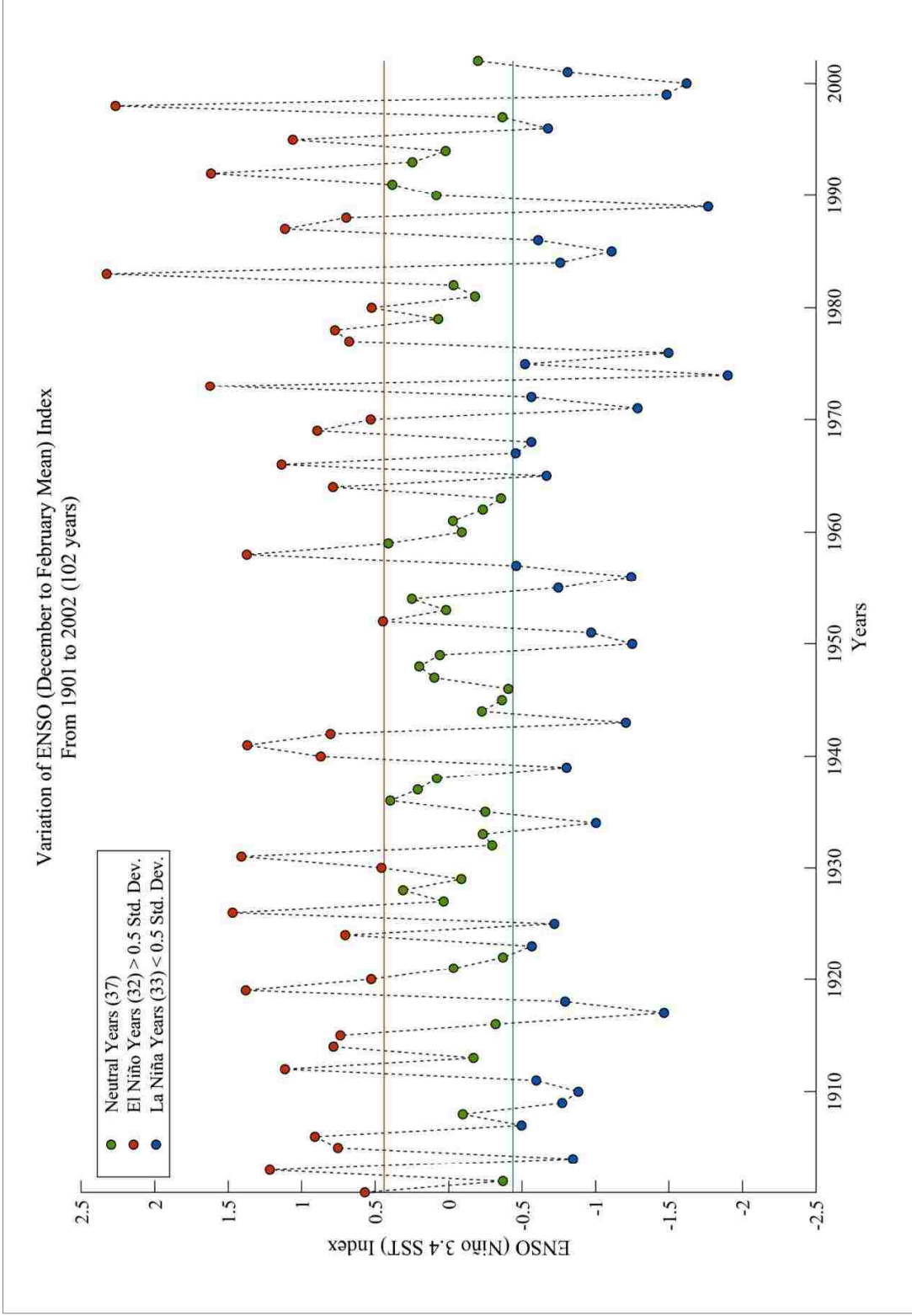
Figure 4. 2: Plot showing the variation of El Niño Southern Oscillation (ENSO, Niño 3.4) index over the current study period. The orange (blue) horizontal line, which delineates 0.5 times the standard deviation above (below) the mean, represents the threshold for El Niño (La Niña).

81

4.3. Methodology

4.3.1. Trend and Shift Tests

Two non-parametric tests – namely, the Mann-Kendall (MK) trend test (Mann, 1945; Kendall, 1975) and the Pettitt's test (Pettitt, 1979) – were used to detect the presence of trends and shifts, respectively. A trend shows the past behavior of a variable that is more likely to be of a monotonic nature and may continue in the future unless an anomaly occurs (Zhang et al., 2001; Tamaddun et al., 2016). The MK trend test is based on the null hypothesis that there is no trend in the time series. The test determines the direction of the trend, which can either be an increase (positive), decrease (negative), or absence of a trend, from the sign of a signum function. In contrast, a shift is an abrupt change in the data distribution, which remains unaltered until the next change occurs (Mauget, 2003; Kalra et al, 2017). Pettitt's test detects the shift in a time series by testing the anomaly between the mean of two independent samples from the same time series. The direction of the shift, which can be either positive (increasing), negative (decreasing), or an absence of a shift, is determined from the maximum and minimum probability estimates based on the significance level used. Non-parametric tests are better suited for hydro-climatological data distributions since such data distributions are more likely to be nonstationary and nonlinear in nature. The resilience against missing data points and robustness against the initial assumption of a normal distribution makes non-parametric tests a preferred choice over traditional statistical tests that have an inherent assumption of nonstationarity and nonlinearity (Milly et al., 2008; Sagarika et al., 2014). Both the tests have been recommended in earlier studies due to their advantages over the other test methods as well as for their higher accuracy. Further remarks about these tests can be found in the works of Lins and Slack (1999), Önöz and Bayazit (2003), Burn (2008), and Villarini et al. (2009). Several modified versions of the MK

test, named MK2, MK3, and MK4, accounting for different types of autocorrelation or persistence, are found in the literature (Tamaddun et al., 2016; Sagarika et al., 2014; Kumar et al., 2009). These modified MK tests were also utilized in this study to analyze the trends. However, the results did not produce noticeable differences from the original results. Hence, descriptions of such methods have been omitted from the study. The lack of noticeable differences from the original test method suggests that autocorrelation or persistence had minimal influence on the datasets used in the study.

To calculate the slope (rate of change or change per unit time) of the observed trends, the Theil-Sen approach (TSA) was employed (Theil, 1950; Sen, 1968). The TSA is nonparametric in nature, which makes it appropriate to be applied in conjunction with the MK test. Moreover, the TSA determines the median slope of all possible pairs, which makes the test robust against possible outliers. Walker's test (Wilks, 2006) was used to determine the global (field) significance of each of the eight states consisting of multiple districts. A confidence interval of 90% ($p \leq 0.10$) was used for the statistical significance tests performed in this study. All the analyses were conducted using the programming platform MATLAB.

4.3.2. Entropy Test

Entropy measures the variance in the temporal distribution of a variable (Mishra et al., 2009). According to Shannon (1948), entropy measures the dispersion (range), uncertainty, anomaly, and variation in data. Such a measure can help distinguish between trends of similar types based on their uniformity over time. A review of entropy applications in the field of hydrology and water resources can be found in the work of Singh (1997). Several indices of entropy can be calculated to measure variability in data (Mishra et al., 2009). For example, while

studying the dynamics in complex systems, such as climate, recent studies have used a new time domain termed natural time (Sarlis et al., 2013; Varotsos et al., 2013) in which the entropy is defined as a dynamic property that captures the time arrow, while the corresponding entropy change under time reversal is used to identify the occurrence (from approaching state to critical state) of extreme scenarios including earthquakes (Sarlis et al., 2018a and b), ENSO events (Varotsos et al., 2016a and b), and quasi-biennial oscillations (Varotsos et al., 2018). In this study, apportionment entropy was used to evaluate the variability in the annual and seasonal (monsoonal) temperature, precipitation, and PET data. The following formulations are based on the works of Shannon (1948) and Mishra et al. (2009). The analyses were conducted using the programming platform MATLAB.

The total annual (seasonal) aggregate, R – aggregated over the study period of 102 years (over the 4 months of monsoon) – of a variable, (i.e., temperature, precipitation, and PET) can be expressed as:

$$R = \sum_{i=1}^{n} r_i \qquad (4.1)$$

where r_i is the annual aggregate amount of a variable during the ith year of the study period (monthly amount of a variable during the ith month of the season), with i = 1 to 102 for annual apportionment (i = 1 to 4 for seasonal apportionment).

The apportionment entropy (AE) of a variable can be written as:

$$AE = -\sum_{i=1}^{n} \left(\frac{r_i}{R}\right) log_2 \left(\frac{r_i}{R}\right) \qquad (4.2)$$

The annual apportionment entropy (AE_a) measured the temporal variability in the annual dispersion of the variable over the study period. Equation 4.2 denotes that when a variable was evenly distributed, on an annual scale, over the study period of 102 years, with a probability of 1/102, AE_a had the maximum value of $\log_2 102$ (or 6.6724). If the apportionment occurred during only one out of the 102 years, with a probability of 1, AE_a would take the minimum value of zero.

Similarly, the seasonal apportionment entropy (AE_s) for the monsoon season was calculated using the June through September monthly mean data. This value varied from zero to $\log_2 4$ (or 2.0). AE_s for all the districts were calculated for each of the 102 years during the study period. For the purpose of representation, the mean AE_s of the 102 years for each of the districts are reported in the study.

4.4. Results and Discussion

This study investigated the change patterns in North Indian hydro-climatological variables – i.e., temperature, precipitation, and PET – influenced by the various ENSO phases during the monsoon season. Initially, trend (shift) patterns were determined in order to observe how the different combinations of the ENSO phases were associated with the change patterns. Later in the study, the all-year trend (shift) patterns were detected during monsoon and at each of the monsoonal months. Finally, to quantify the spatiotemporal variation of the variables, annual and seasonal (monsoonal) apportionment entropies were calculated. Modified MK tests, adjusted for persistence as per Kumar et al. (2009), were applied to the data as well. The results did not show any significant deviation from the standard (original) test results. Hence, only the findings from the standard methods are reported in the study.

4.4.1. Temperature Change Patterns

4.4.1.1. Changes Associated with ENSO

The spatial distribution of trends suggested that the western regions, i.e., Chandigarh, Haryana, and Punjab, as well as a significant portion of Uttar Pradesh, experienced a decreasing trend in all the ENSO phases (Figure 4.3). States, such as Himachal Pradesh, Jammu and Kashmir, and Uttarkhand, did not show much of a presence of significant trends except during the El Niño years. The spatial distribution of districts with significant trends during the El Niño (La Niña) and non-La Niña (non-El Niño) years were found to be comparable. Districts with significant decreasing trends during the El Niño (La Niña) years were found to be the maximum (minimum) among the four ENSO phases analyzed in the study. An increasing trend was observed only during a neutral year. Table 4.1 summarizes the results in terms of the number of districts with significant trends. It can be inferred from the results that the El Niño years, compared to other phases of ENSO, had a higher influence on the decreasing trends in temperature during the monsoon season. The prolonged effect of El Niño on temperature variations of the Indian Ocean and the resulting heat fluxes among various land masses can be attributed as one of the major reasons for the observed variations (Wang et al., 2005; Xie et al., 2009).

The spatial pattern of shifts suggested that the El Niño (La Niña) and non-La Niña (non-El Niño) years had a similar influence on the study area. All the states – or a large portion of them except for Jammu and Kashmir, and Uttarkhand – had significant negative shifts during the El Niño and non-La Niña years (Figure 4.4). Districts in Uttarkhand and Uttar Pradesh, which did not show the presence of shifts during the El Niño or non-La Niña years, were found to be

significant during the La Niña and non-El Niño years. This feature of the shift patterns suggested that the two opposing phases of ENSO influenced certain regions of North India in distinct ways (Figure 4.4). The El Niño (La Niña) years showed similar spatial patterns as the non-La Niña (non-El Niño) years. The maximum (minimum) number of districts with significant negative shifts was observed during the non-La Niña (La Niña) years (Table 4.1).

4.4.1.1. All-Year Change Patterns

The all-year trend patterns suggested that the entire states of Haryana and Punjab, as well as the western regions of all the remaining states, experienced decreasing trends either during the entire four-month summer monsoon or in any of the monsoonal months (Figure 4.5). The eastern regions of Himachal Pradesh, Jammu and Kashmir, Uttarkhand, and Uttaranchal did not show a significant presence of trends. The monthly variation of trends showed that from June to September, the spatial location of districts with significant trends shifted from the southwest towards the north, then shifted back towards the southwest (Figure 4.5). This change in spatial distribution could be explained by the direction of the monsoon circulation, which carries humid summer winds from the southwest direction in June and sweeps across the Indian subcontinent by moving north; eventually, these winds move back to the southwest of India in September. Table 4.2 lists the number of districts with significant trends during the monsoon and in each of the monsoonal months. The range of TSA slopes during the monsoon and the monsoonal months also showed the overall inclination towards decreasing trends (Table 4.3). The TSA slopes suggest that the month of June experienced the highest variation in temperature over the study period. Decreasing trends in temperature in many parts of North India also were observed in the mean temperature trends from 1951 to 2010 by Rathore et al. (2013), which support the findings of the current study.

The all-year shift patterns suggested that except for a few districts in the eastern part of Jammu and Kashmir and Uttar Pradesh, the remainder of North India experienced negative shifts either during the monsoon or in any of the monsoonal months (Figure 4.6). Similar to the trends, the shift patterns showed a northbound movement followed by a southbound movement in districts having significant shifts during the individual monsoonal months. Table 4.2 summarizes the results in terms of the number of districts with significant shifts. Table 4.4 shows the earliest and latest shift along with the major intervals having a higher number of shift points in temperature during the study period. A comparison of the shift points (Table 4.4) with the ENSO indices (Figure 4.2) showed that most of the shift points coincided with the El Niño and non-La Niña years. Previous studies and historical events (Kumar et al., 1999; Kumar et al., 2006), causing climate extremes, were found to be consistent with the major shift points detected in the current study. For both the trend and shift patterns, states with field significance were observed to vary across the months (Figures 4.5 and 4.6).
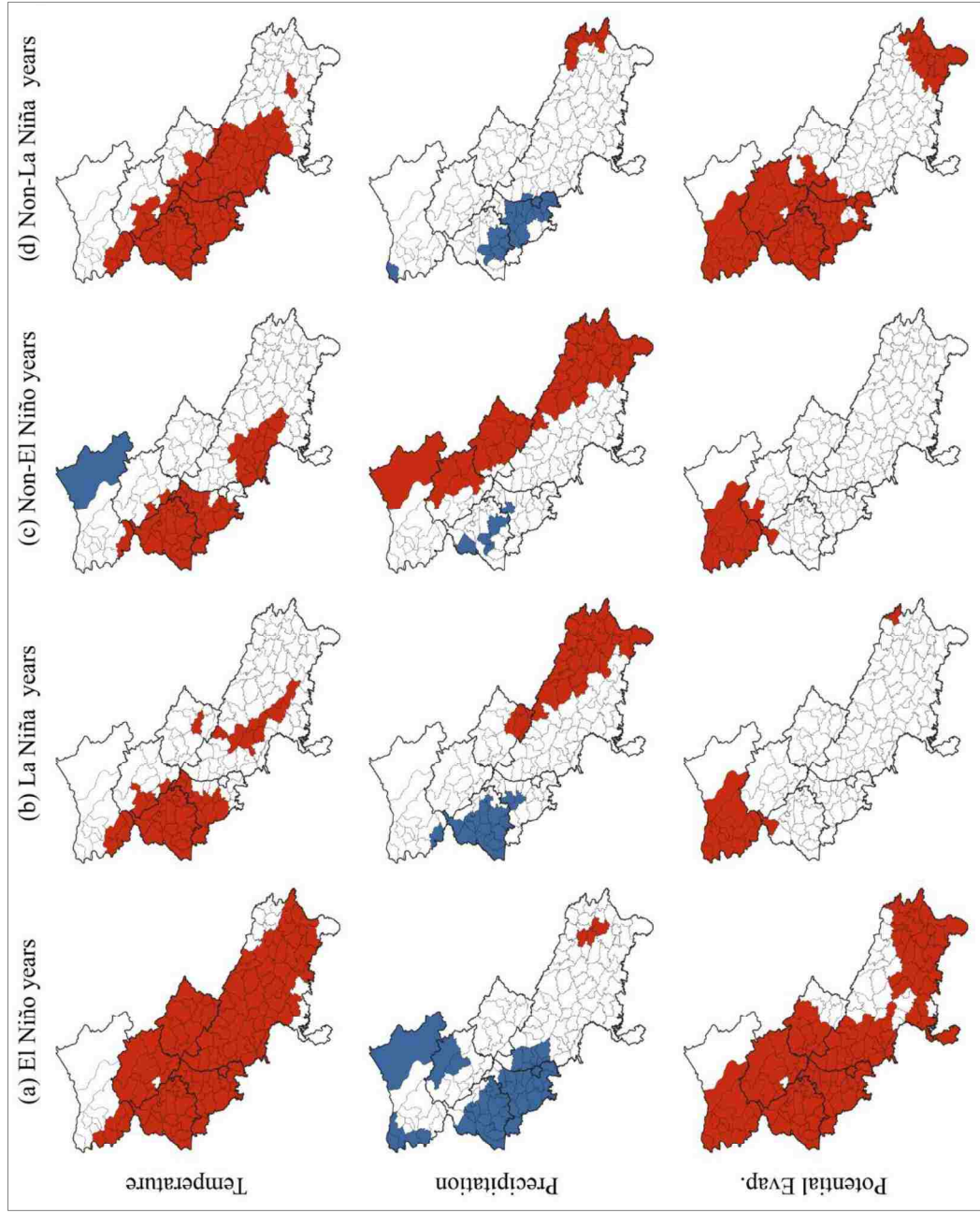
Figure 4. 3: Maps showing the spatial distributions of districts with significant trends in the monsoon season under the MK test for temperature, precipitation, and potential evapotranspiration in the (**a**) El Niño, (**b**) La Niña, (**c**) non-El Niño, and (**d**) non-La Niña years. Blue (red) represents districts with increasing (decreasing) trend.

89
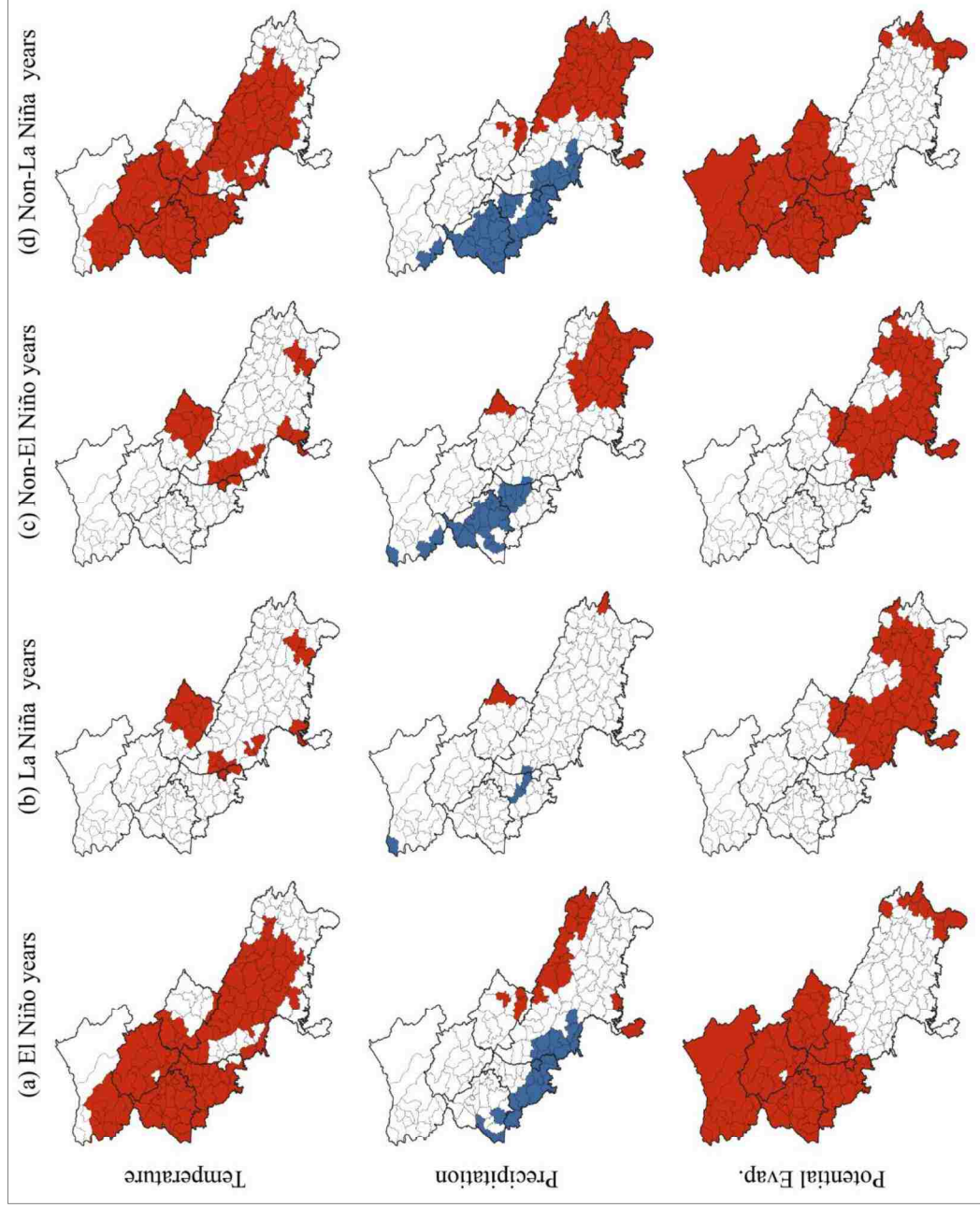
Figure 4. 4: Maps showing the spatial distributions of districts with significant shifts in the monsoon season under the Pettitt's test for temperature, precipitation, and potential evapotranspiration in the (**a**) El Niño, (**b**) La Niña, (**c**) non-El Niño, and (**d**) non-La Niña years. Blue (red) represents districts with a positive (negative) shift.

Table 4. 1: The Number of districts (out of a total of 146) with significant increasing or decreasing trends and shifts in temperature, precipitation, and potential evapotranspiration during the different ENSO phases.

		El Niño years		La Niña years		Non-El Niño years		Non-La Niña years	
		Increasing	Decreasing	Increasing	Decreasing	Increasing	Decreasing	Increasing	Decreasing
Temperature	Trends	–	125 (86%)	–	47 (32%)	1	53 (36%)	–	84 (58%)
	Shifts	–	99 (68%)	–	20 (14%)	–	23 (16%)	–	102 (70%)
Precipitation	Trends	43 (29%)	3 (2%)	16 (11%)	33 (23%)	5 (3%)	47 (32%)	20 (14%)	6 (4%)
	Shifts	22 (15%)	18 (12%)	4 (3%)	2 (1%)	23 (16%)	25 (17%)	41 (28%)	41 (28%)
Pot. Evap.	Trends	–	120 (82%)	–	15 (10%)	–	15 (10%)	–	78 (53%)
	Shifts	–	88 (60%)	–	52 (36%)	–	52 (36%)	–	88 (60%)

Table 4. 2: The Number of districts (out of a total of 146) with significant increasing or decreasing trends and shifts in temperature, precipitation, and potential evapotranspiration during monsoon and at each of the monsoonal months.

		Monsoon		June		July		August		September	
		Increasing	Decreasing	Increasing	Decreasing	Increasing	Decreasing	Increasing	Decreasing	Increasing	Decreasing
Temperature	Trends	–	109 (75%)	–	49 (34%)	–	76 (52%)	–	60 (41%)	–	92 (63%)
	Shifts	–	122 (84%)	–	99 (68%)	–	86 (59%)	–	76 (52%)	1 (1%)	113 (77%)
Precipitation	Trends	35 (24%)	32 (22%)	23 (16%)	6 (4%)	24 (16%)	33 (23%)	25 (17%)	38 (26%)	–	–
	Shifts	45 (31%)	43 (29%)	43 (29%)	7 (5%)	31 (21%)	38 (26%)	41 (28%)	40 (27%)	–	1 (1%)
Pot. Evap.	Trends	–	93 (64%)	–	14 (10%)	–	31 (21%)	–	31 (21%)	–	53 (36%)
	Shifts	–	140 (96%)	–	93 (64%)	–	89 (61%)	–	113 (77%)	–	146 (100%)

4.4.2. Precipitation Change Patterns

4.4.2.1. Changes Associated with ENSO

A distinct separation across North India was observed between the districts with increasing and decreasing trends in the spatial patterns of trends. During the various ENSO phases, the western regions, i.e., Delhi, Haryana, and Punjab, a significant portion of Jammu and Kashmir, and a few districts in Himachal Pradesh and Uttar Pradesh, experienced increasing trends (Figure 4.3). Decreasing trends were localized in the eastern regions, i.e., significant portions of Himachal Pradesh, the entire state of Uttarkhand, and the eastern part of Uttar Pradesh. The maximum numbers of districts with increasing (decreasing) trends were observed during the El Niño (non-El Niño) years (Table 4.1). In some instances, the direction of the trends reversed when the ENSO phase changed from El Niño to non-El Niño. As suggested by previous studies, these variations could be explained by factors that either could strengthen or weaken the effects of ENSO on the monsoon (Saji et al., 1999; Ashok et al., 2004; Charles, 1997). Other studies suggest that the teleconnection has different correlations based on the time scales (i.e., interannual, quasi-decadal, or decadal), which might affect long-term trend patterns (Torrence and Webster, 1999; Reason et al., 2000; Gadgil et al., 2004).

Similar to the trend patterns, shift patterns of precipitation also showed a spatial separation between the districts with positive and negative shifts (Figure 4.4). Spatial patterns in the various ENSO phases showed that both the El Niño and neutral years played a significant role in the precipitation shift patterns across North India. In the various ENSO phases, the western regions, i.e., Delhi, Haryana, and Punjab, as well as a few western districts of Jammu and Kashmir and Uttar Pradesh, showed positive shifts (Figure 4.4). Negative shifts were

observed only in the eastern part of Uttar Pradesh and in a few districts of Uttarkhand. This showed that North India experienced both positive and negative shifts during the various ENSO phases even though the shifts were spatially separated and localized to certain regions. In the precipitation trends, there were instances in which the direction of the trend reversed with the change of the ENSO phase from El Niño to La Niña; however, precipitation shift patterns did not show such a reversal in direction. The La Niña (non-La Niña) years had the minimum (maximum) number of districts with significant shifts (Table 4.1).

4.4.2.2. All-Year Change Patterns

In the all-year trend patterns, the western regions, i.e., Delhi, Haryana, and Punjab as well as a few western districts of Jammu and Kashmir, and Uttar Pradesh, experienced increasing trends either during the monsoon or in any of the monsoonal months (Figure 4.5). Decreasing trends were observed in the eastern districts of Uttarkhand and Uttar Pradesh and in a few of the western districts of Uttar Pradesh. (Figure 4.5). A greater tendency towards decreasing trends in the eastern regions was observed by Rathore et al. (2013). Monthly trends followed similar spatial patterns, although the number of districts with trends varied significantly across the monsoonal months (Table 4.2). July and August showed a higher number of districts with significant trends compared to June. This monthly variation could be explained by the timing of the monsoon circulation. Since the monsoon season starts in June and ends in September, it can be inferred that the effects of the monsoon developed fully during July and August. Since the monsoon recedes in September, it might be possible that the change in wind direction does not result in causing significant change. This also was observed in the TSA slope values for September (Figure 4.5), as the slopes during September did not follow any spatial pattern; rather,

they were quite arbitrary in nature (Table 4.3). Comparison of TSA values suggested that July and August experienced a higher change over the study period.

Similar to the all-year trend patterns, the all-year shift patterns also showed a separation in the locations of districts with significant positive and negative shifts (Figure 4.6). Southwestern districts of Uttar Pradesh showed positive shifts but did not show increasing trends in the trend pattern. Similar to the trend pattern, September did not show significant shifts except for a single district with a negative shift in Uttar Pradesh. The northbound movement followed by a southbound movement of the districts with significant trends (shifts) occurring from June to August could also be explained by the direction of the monsoon circulation as discussed earlier. The monthly variation (Table 4.2) showed a similar generic spatial pattern of positive and negative shifts – for the western and the eastern regions, respectively – but varied significantly in terms of the number of districts with significant shifts (Figure 4.6). Table 4.4 shows the locations of the major shift points in precipitation during the study period. The shift points observed mostly coincided with the non-La Niña years, as was observed by comparing the results with Figure 4.2. States with field significance were observed to vary across the various monsoonal months in both the trend and shift patterns.
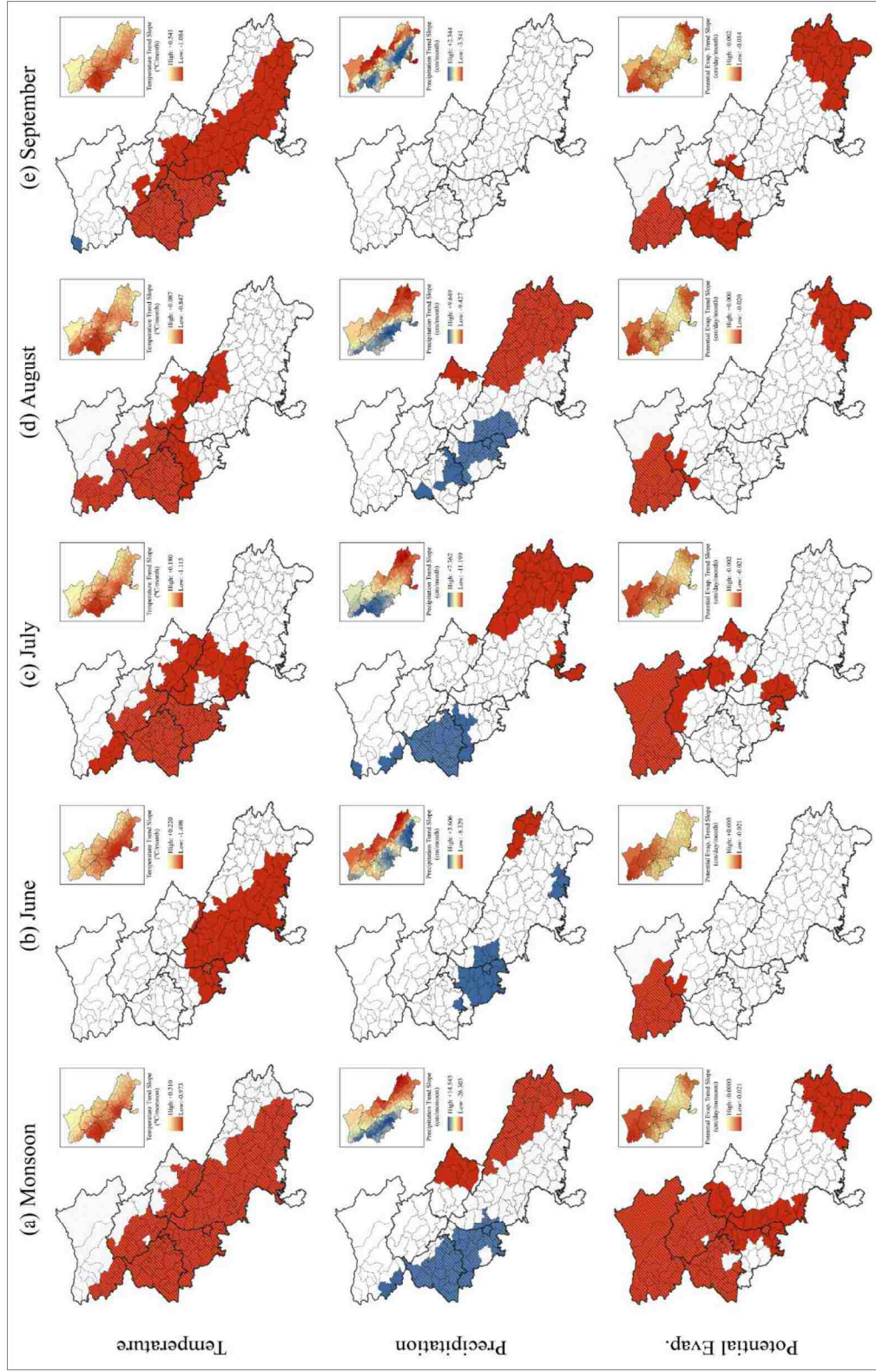
Figure 4. 5: Maps showing the spatial distributions of districts with significant trends under the MK test for temperature, precipitation, and potential evapotranspiration in (**a**) monsoon and the monsoonal months of (**b**) June, (**c**) July, (**d**) August, and (**e**) September. Blue (red) represents districts with increasing (decreasing) trend. The inset maps show the spatial dispersal of the slope values of the trends obtained from the TSA (shown as the total change over the study period). States with light gray hatches represent the presence of field significance.

95
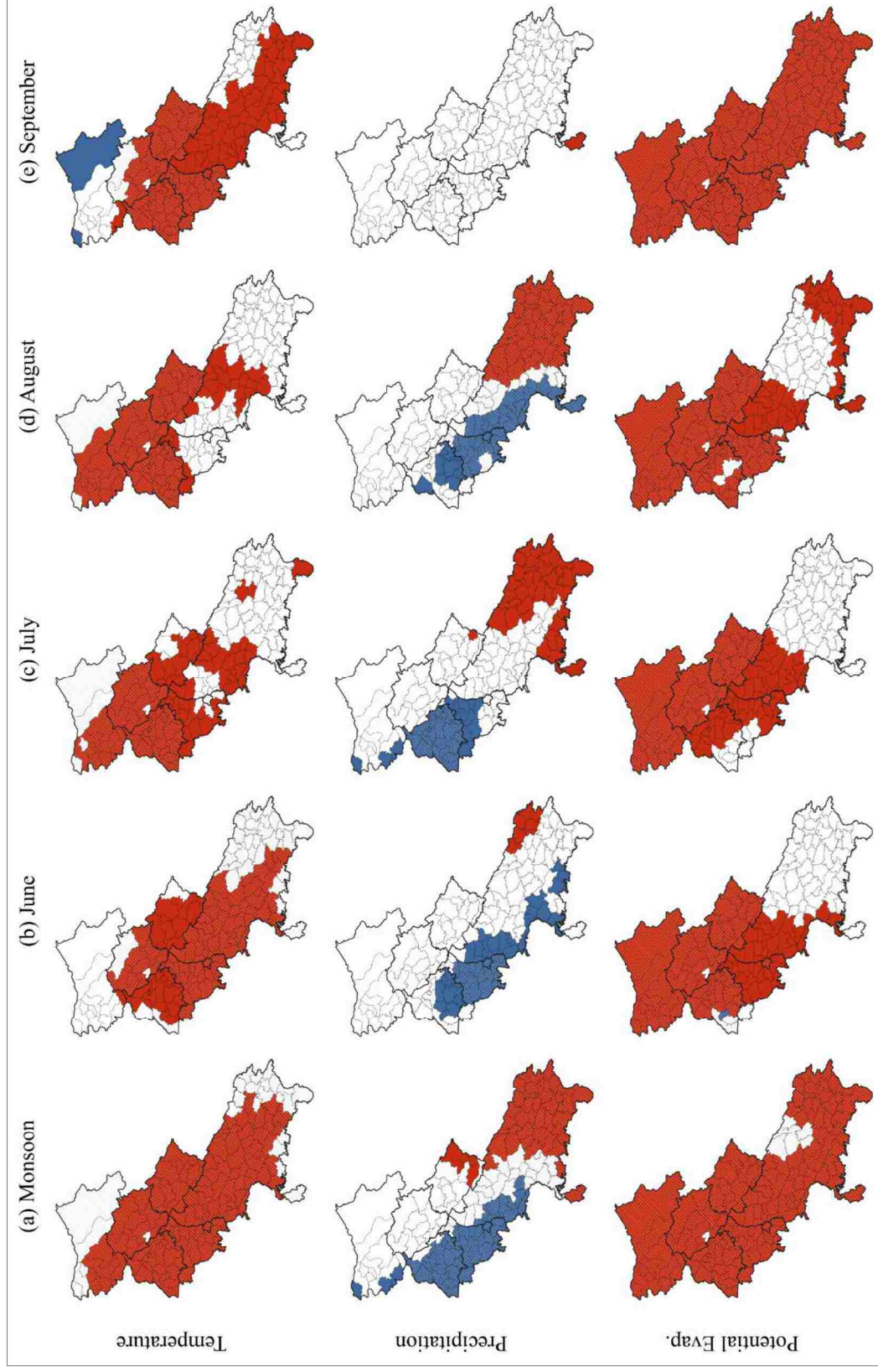
Figure 4. 6: Maps showing the spatial distributions of districts with significant shifts under the Pettitt's test for temperature, precipitation, and potential evapotranspiration in (**a**) monsoon and the monsoonal months of (**b**) June, (**c**) July, (**d**) August, and (**e**) September. Blue (red) represents districts with a positive (negative) shift. States with light gray hatches represent the presence of field significance.

Table 4. 3: The range of all-year Theil-Sen approach (TSA) slopes (shown as the total change over the study period) of temperature, precipitation, and potential evapotranspiration during monsoon and at each of the monsoonal months.

	TSA (Slope) Range (shown as the total change over the study period)				
	Monsoon	June	July	August	September
Temperature (°C/time unit) Range (95% confidence interval)	-0.97 to +0.31 (-0.54 to -0.45)	-1.50 to +0.22 (-0.70 to -0.59)	-1.12 to +0.18 (-0.60 to -0.51)	-0.85 to +0.09 (-0.39 to -0.32)	-1.08 to +0.54 (-0.50 to -0.39)
Precipitation (cm/time unit) Range (95% confidence interval)	-26.30 to +14.55 (-3.08 to 0.50)	-8.33 to +3.61 (0.34 to 0.91)	-11.20 to +7.34 (-2.29 to -0.48)	-9.43 to +9.65 (-1.89 to -0.08)	-3.54 to +2.34 (0.06 to 0.41)
Pot. Evap. (cm/day/time unit) Range (95% confidence interval)	-2.56 to -0.04 (-0.007 to -0.006)	-0.63 to +0.16 (-0.003 to -0.002)	-0.65 to -0.06 (-0.007 to -0.006)	-0.62 to +0.00 (-0.006 to -0.005)	-0.42 to -0.06 (-0.007 to -0.006)

Table 4. 4: The location in time of the earliest and latest significant shift of temperature, precipitation, potential evapotranspiration. The major intervals, with years without significant shifts in between, show the location where the majority of the significant shift points were detected in the study.

	Earliest Shift	Latest Shift	Major Intervals
Temperature	1908	1997	1915-1932 1947-1973 1985-1986
Precipitation	1905	1996	1908-1917 1920-1934 1939-1978 1980-1996
Pot. Evap.	1920	1976	1920-1930 1941-1958 1970-1975

4.4.3. Potential Evapotranspiration Change Patterns

4.4.3.1. Changes Associated with ENSO

All the states of North India, or a significant portion of them, were observed to experience decreasing trends during the El Niño years in the PET trend patterns (Figure 4.3). The states showed hardly any significant trends during the La Niña and non-El Niño years, except for a portion of Jammu and Kashmir and a district each in Himachal Pradesh, Punjab, and Uttar Pradesh. This suggested that the effect of ENSO phases on PET was not evenly distributed across the districts. With fewer districts of significance in Uttar Pradesh, the non-La Niña years had a similar spatial pattern as the El Niño years. The La Niña years and non-El Niño years also showed similar spatial patterns. The maximum (minimum) number of districts with decreasing trends was observed during the El Niño (La Niña and non-El Niño) years (Table 4.1). Similar to the temperature trends, the effect of neutral years, compared to the El Niño and La Niña years, on the change patterns of PET was observed to be less significant (Figure 4.3). Previous studies have suggested that El Niño has a much higher potential of altering the evaporation configuration around Indian Ocean basins, which eventually could affect the temperature of those basins (Klein et al., 1999), as was found in the current study, especially during the El Niño and non-La Niña years.

The spatial distribution of PET shift patterns revealed that all the districts, except for a few districts in Uttar Pradesh, experienced negative shifts either during the El Niño or the La Niña years (Figure 4.4). The comparisons revealed that the neutral phases did not play a significant role in the shifts, as the El Niño (La Niña) years had exactly the same spatial patterns as the non-La Niña (Non-El Niño) years. This suggested that the districts experiencing shifts

during the El Niño and La Niña years were mutually exclusive (Figure 4.4). The El Niño (non-La Niña) years had a higher number of districts with negative shifts compared to the La Niña (non-El Niño) years (Table 4.1). In the PET trend patterns, the same districts showed the presence of trends during both the El Niño and La Niña years. This was not observed in the shift patterns of PET, which suggests that the El Niño and La Niña years were associated with or influenced the PET shifts of the northern and southern regions of North India mutually exclusively.

4.4.3.2. All-Year Change Patterns

The all-year trend patterns revealed that most of the decreasing trends were observed in the northwestern regions, i.e., Himachal Pradesh, Punjab, and Jammu and Kashmir, as well as in the southeastern districts of Uttar Pradesh either during the monsoon or in any of monsoonal months (Figure 4.5). The central part of Uttar Pradesh and the entire state of Uttarkhand did not show much presence of trends in any of the monsoonal months. The monthly variation (Table 4.2) of trend patterns showed that June and July had districts with decreasing trends, mostly in the northern regions; meanwhile, August and September had decreasing trends both in the northern and southern regions (Figure 4.5). Compared to the temperature and precipitation trend patterns, the change in PET across the months did not follow a northbound and a subsequent southbound movement. However, northern regions showed a higher number of districts with trends in the first half of the season, while southern regions had a higher number of districts with trends in the second half of the season. The TSA values (Table 4.3) suggested that June experienced the greatest change in PET over the study period (Figure 4.3). Moreover, the results suggested that the decreasing trend in temperature did not necessarily cause a decreasing trend in PET – at least not during all the months of the monsoon (Figure 4.5). The decreasing trends in

PET and its anomaly with temperature trends could be explained by the stressed crops and reduced vegetation across India (Singh et al., 2003; Kohli et al., 2006).

In the all-year shift patterns, all the districts of North India were observed to experience negative shifts either during monsoon or in any of the monsoonal months. Some mid-southeastern and southeastern districts of Uttar Pradesh did not show the presence of a trend during June, July, and August (Figure 4.6). However, during September, all of North India experienced negative shifts. Except for one district in June, which could be considered as an anomaly, no presence of positive shifts was observed across the study period during the monsoon season or in any of the monsoonal months. The locations of the major shift points in PET during the study period are shown in Table 4.4. Comparing the results with Figure 4.2 showed that the shift points coincided with both the El Niño and La Niña years, but not so much with the neutral years. Districts all across North India experienced shifts, while mostly northern and southern regions showed the presence of trends – which was a significant difference between the PET trend (Figure 4.3) and PET shift patterns (Figure 4.5). For both the all-year trend and shift patterns, states with field significance were observed to vary across the monsoonal months.

4.4.4. Entropy

4.4.4.1. Temperature Entropy

The AE_a suggested that the temperature change was distributed quite evenly over the study period (102 years) across most of North India (Table 4.5), except for a few northeastern regions that experienced apportionment over approximately 98 years (Figure 4.7). The spatial distribution suggested that the southeastern and northwestern regions had higher AE_a values compared to the rest of the study area. The AE_s of temperature suggested that the temperature

change also was quite uniform across the monsoonal months, with the lowest AE_s value referring to a change apportioned over 3.86 months (Table 4.5). The spatial pattern of AE_s was found to be more dispersed across the different districts compared to the AE_a pattern. This variation was more prominent in the comparison between the standardized AE_a and AE_s values (Figure 4.7). For most districts, annual variation was observed to be close to the mean value, which was not the case for seasonal variation. The results showed that a variation in AE_s was much higher than in AE_a, even among nearby districts. This suggests that the different months of monsoon affected change patterns differently for each district; however, on an annual scale, the change was much more uniform across years. A comparison between the trends in temperature (Figure 4.3) and the entropy distribution of temperature (Figure 4.7) suggested that many districts with significant decreasing trends had higher entropy values, indicating an even distribution of change over the study period.

4.4.4.2. Precipitation Entropy

The values of the precipitation AE_a were found to be apportioned over approximately 97 to 100 years (Table 4.5) across the districts, which suggested that the variation in precipitation was less evenly distributed over the study period compared to the variation in temperature (Figure 4.7). On the other hand, the AE_s of precipitation was found to be apportioned over 3.00 to 3.67 months, indicating higher monthly variation across the monsoonal season (Table 4.5). The spatial distribution of both the AE_a and AE_s were found to be similar for the mid-eastern and southeastern regions having higher entropy values, and the mid-western and northwestern regions having lower entropy values. This similarity of apportionment was evident when comparing the standardized AE_a and AE_s values (Figure 4.7), which suggested that the nearby districts had similar temporal variations. A comparison between the precipitation trend patterns

(Figure 4.5) and precipitation entropy distribution (Figure 4.7) suggested that districts with increasing (decreasing) trends had lower (higher) entropy. This could be an important feature when trying to understand trend patterns. The results imply that even though some districts showed increasing trends, their temporal distribution was less evenly distributed over the years, as well as across the monsoonal months when compared to the districts with decreasing trends. This suggested that the overall trend pattern of precipitation has decreased with much greater uniformity, compared to the increase, during the study period. This could be an important insight regarding the increasing trends observed during the El Niño years. Although the difference in apportionment was found to be only three years (97 and 100 years for districts with the lowest and highest entropy, respectively), the results certainly showed how apportionment entropy could explain trend patterns with greater insight.
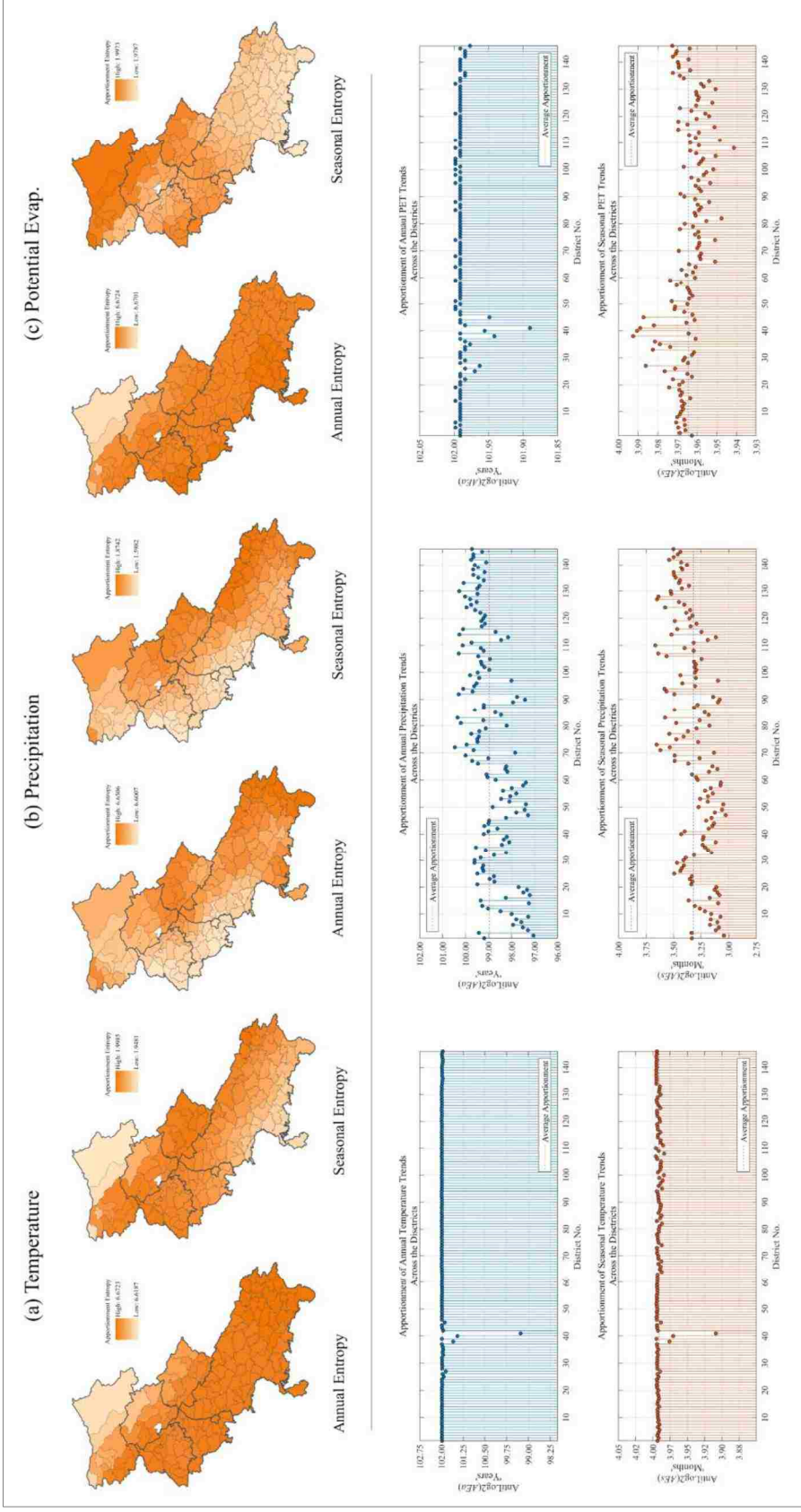
Figure 4. 7: (Top) Maps showing the spatial distribution of the annual and seasonal apportionment entropy for (**a**) temperature, (**b**) precipitation, and (**c**) potential evapotranspiration. (**Bottom**) Plots showing the variation in the standardized annual and seasonal variation of the apportionment entropy index across all the districts for the chosen variables. Appendix 4 (Table A4.1) contains the names and numbers of the individual districts in each of the states.

Table 4. 5: The range of annual and seasonal apportionment entropy of temperature, precipitation, and potential evapotranspiration across the study period of 102 years and along four months of monsoon.

	Annual Apportionment Entropy (AE$_a$)		Seasonal Apportionment Entropy (AE$_s$)	
	Range (from 0 to 6.6725)	Apportionment (years) (from 1 to 102)	Range (from 0 to 2)	Apportionment (months) (from 1 to 4)
Temperature (95% confidence interval)	6.6187 to 6.6723	98.27 to 101.99 (101.89 to 101.99)	1.9481 to 1.9985	3.86 to 3.99 (3.98 to 3.99)
Precipitation (95% confidence interval)	6.6007 to 6.6506	97.05 to 100.47 (98.82 to 99.09)	1.5982 to 1.8742	3.02 to 3.67 (3.29 to 3.34)
Pot. Evap. (95% confidence interval)	6.6701 to 6.6724	101.84 to 101.99 (101.98 to 101.99)	1.9787 to 1.9973	3.94 to 3.99 (3.963 to 3.965)

4.4.4.3. Potential Evapotranspiration Entropy

On an annual scale, the AE$_a$ of PET showed that the variations observed were quite evenly distributed (apportionment of approximately 102 years) over the study period (Table 4.5). The AE$_s$ of PET showed higher values of apportionment over almost all the months of monsoon; however, the spatial distribution was found to be quite different than what was observed in the AE$_a$ (Figure 4.7). Even though the actual range within which the values varied (1.9787 to 1.9973) was quite narrow (Table 4.5), the variation was quite high among the adjacent districts. The results showed that the spatial pattern of districts with higher and lower apportionment indices was quite opposite in the AE$_a$ and AE$_s$. Higher AE$_a$ values were observed in the mid-western and southern regions, while the northeastern regions showed lower AE$_a$ values. This pattern was reversed in the AE$_s$ distribution (Figure 4.7). The reversed behavior was more evident when comparing the standardized AE$_a$ and AE$_s$ values (Figure 4.7). Although both the annual and the seasonal variations suggested an even distribution temporally, the reversal in their

spatial distribution suggested that the variation in PET during monsoonal months was opposite from the long-term annual variation. A comparison of PET trend patterns (Figure 4.5) and PET entropy distribution (Figure 4.7) revealed that many of the districts with significant decreasing trends showed higher AE_a values, indicating that the change was fairly even.

The analyses of entropy for each of the variables showed how the change patterns were distributed temporally across the years and the monsoon season. In the cases when a variable experienced both the increasing and decreasing trends, the entropy revealed if one of the trends was more prevalent over the years (or across the season) or both had similar temporal distribution. Thus, the conjunction of the entropy analysis with the trend test (coupled with slope detection) provides greater insight into the nature of a trend.

4.5. Conclusions

In this study, three hydro-climatological variables, i.e., temperature, precipitation, and PET, were analyzed over century-wide data (from 1901 to 2002) to evaluate the influence of various ENSO phases on the change patterns across North India during the monsoon season. Trend and shift patterns in 146 districts in eight North Indian states were analyzed, and the annual and the seasonal (monsoonal) apportionment entropy that quantified the temporal distributions of the change patterns were evaluated. Besides the effects of ENSO, the all-year (century-wide) monsoonal change patterns were analyzed to determine the effect of each of the monsoonal months on the long-term patterns. Results suggested that the El Niño years, compared to the La Niña and neutral years, had a much greater influence on the change patterns of the variables. The all-year change patterns suggested a significant decrease in the temperature and PET trends and shifts across North India, while the precipitation change patterns (both increasing

and decreasing) were found to be region-specific. The entropy analyses suggested that the highest variation in the long-term change pattern occurred in precipitation data, whereas temperature and PET experienced more variation during the monsoon season compared to changes over the years.

Major physical and dynamic relationships affecting the monsoon season due to the change in ENSO phases in the Indian subcontinent were compiled and discussed in this study based on the previous literature. By analyzing multiple hydro-climatological variables of North India, the study illustrated how various variables can be affected by the different phases of ENSO. Climate researchers and policymakers may find the results useful to understand the variability resulting from the various ENSO phases during the north Indian monsoon season. Such understanding may help devise strategies to mitigate the adverse effects of climate extremes.

CHAPTER 5: COMPARISON OF TRENDS AND SHIFTS IN THE OBSERVED AND MODELED (CMIP5) TEMPERATURE AND PRECIPITATION PATTERNS OF THE COLORADO RIVER BASIN UNDER SHIFT AND PERSISTENCE

5.1. Introduction

Understanding of trends in various hydro-climatological data, under the influence of climate change, to yield practical solutions to the existing and imminent threats, is a major topic of research in the scientific community, especially among the climate data modelers (Asrar et al., 2012; Arnell, 2011; Shakya et al., 2019). The recent assessment reports (AR5 and AR6) of the Intergovernmental Panel on Climate Change (IPCC) (IPCC, 2014 and 2019) has provided a synthesis of results for policymakers based on simulation results provided by phase five of the Coupled Model Intercomparison Project (CMIP5) (Taylor et al., 2012). Many studies, both on the continental and regional scales, have focused on historical as well as projected temperature and precipitation trends in the multi-model CMIP5 data to examine extreme climate conditions (Wuebbles et al., 2014; Lynch et al., 2016; Nyaupane et al., 2018; Chen et al., 2019). A study by Kumar et al. (2013) evaluated the effects of persistence, i.e., clustering behavior in the hydro-climatological observations, in the long-term trends on a global scale and compared the results against multiple observed datasets. The study suggested that the CMIP5 models are capable of capturing the effects of persistence in temperature better than precipitation. Presence of persistence, e.g., positive serial correlation, has been considered as one of the major reasons of uncertainty in hydro-climatological data since it reduces the effective sample size, which leads to an overestimation of variance, and overestimates the probability of a significant trend (Hamed and Rao, 1998; Yue et al., 2002; Koutsoyiannis, 2003). Another important feature of nonstationary hydro-climatological data is the presence of shifts (abrupt changes) in the data

distributions (Villarini et al., 2009). A non-stationary time series experiences changes in the distribution function over time, which may lead to a significant change in variance. Villarini et al. (2009) suggest that a trend is "*likely to continue in the future*", whereas a change point (shift point) implies "*shift from one regime to another, and the status is likely to remain the same until a new regime shift occurs*". Ignoring the effect of shift points (SPs) in trend analyses may lead to ambiguous results. Figure 5.1 (left) shows an example of how ignoring an SP in the data distribution may lead to erroneous detection of trends (a similar example was shown by Villarini et al. (2009) to illustrate that performing a trend test before considering the SP may result in a detection of erroneous significant trend). However, if the presence of an SP was considered, the two subseries – before and after the SP – independently do not suggest statistically significant trends (note the horizontal slopes in Figure 5.1). More details on the importance of detecting SPs in association with trends can be found in the works of Villarini et al. (2009) and Mallakpour and Villarini (2016). Studies like Kalra et al. (2008), Miller et al. (2008), and Sagarika et al. (2014) have also used trend and shift detection tests – however, these studies considered trends and shifts to be independent of each other, at least when applying the tests. A recent study by Serinaldi and Kilsby (2015) suggests that the shift detection tests are also affected by the presence of trends and persistence, especially by the short term persistence (STP). Hence, de-trending the data (if required) and removal of persistence, before the trend and/or shift detection tests, becomes imperative to produce results with higher reliability.

In this study, simulated temperature and precipitation time series of CMIP5 (referred to as CMIP5 temperature and precipitation models in the later sections of the manuscript) for the Upper and Lower Colorado River Basins (UCRB and LCRB, respectively) were analyzed to determine the presence of significant trends and shifts with respect to persistence. A total of 41

temperature and 25 precipitation CMIP5 models were analyzed over a study period of 104 years, i.e., from 1901 to 2004. For each model, a significant SP was detected (if present) using the Pettitt's test (Pettitt, 1979), followed by the analyses of trends before and after the significant SP using the Mann-Kendall (MK) test (Mann, 1945; Kendall, 1975). Both the Pettitt's and the MK tests are of nonparametric in nature, which makes them appropriate for climate data distributions that are often subject to non-stationarity and non-normality (Kumar et al., 2009). Villarini et al. (2009) compared among multiple parametric and non-parametric tests to detect both shifts and trends and concluded that the Pettitt's and the MK test were the most reliable ones in detecting shifts and trends, respectively. For the shift detection test, trend-free-pre-whitening (TFPW), based on Yue et al. (2002), was applied as suggested by Serinaldi and Kilsby (2015), to remove the effect of STP from the models. Several modified MK tests were applied, based on Kumar et al. (2009), to determine the effects of both the long-term persistence (LTP) and STP on the identified trends. To evaluate the ability of CMIP5 models to capture the observed trends, under the influence of SPs and persistence, data from the Climate Research Unit Time Series version 3.10 (CRU-TS) were analyzed. Both the CMIP5 and CRU-TS datasets were analyzed at identical spatial and temporal resolutions.

Based on literature review of the recent studies (Villarini et al., 2009; Venema et al., 2012; Williams et al., 2012), this study hypothesized that trend analyses are better explained if SP detection tests are included prior to the trend tests as was explained earlier with the example in Figure 5.1. Hence, the first objective of the study was to detect SPs in both the modeled and observed datasets and to evaluate the presence of trends independently before and after the SPs. Studies also suggest the importance of the removal of persistence preceding both the trend and shift detection tests. Therefore, as the second objective, the study evaluated the effects of

persistence on the detected trends and shifts. As the final objective, the efficacy of CMIP5 models to match the observed trends, considering both the significant SPs and persistence, was evaluated across the Colorado River Basin (CRB).

5.2. Study Area and Data

Data from 41 temperature and 25 precipitation CMIP5 models (https://cmip.llnl.gov/) were obtained (in terms of anomalies calculated with respect to 1961-1990 mean to be consistent with the observed data) from 1901 to 2004 for the UCRB and LCRB. The basin boundaries were obtained from the USGS hydrologic unit map (https://water.usgs.gov/GIS/huc.html). For each model, only the first ensemble member was considered in the analyses. The obtained data were re-gridded (as suggested by Kumar et al. (2013) using an area-average preserving method) to a common spatial resolution of 2.5° x 2.5°, which resulted in a total of 22 grid cells (boxes or squares) for the entire CRB (Figure 5.1). Grid cells 1 to 10, 14, and 15 had the majority of their portions in LCRB, while grid cells 11 to 13, and 16 to 22 had the majority of their portions in UCRB (Figure 5.1). The observed CRU-TS temperature and precipitation time series data (in terms of anomalies with respect to 1961-1990 mean) (https://crudata.uea.ac.uk/cru/data/hrg/) were up-scaled from 0.5° x 0.5° to 2.5° x 2.5° using an area-average preserving method as well, as suggested by Kumar et al. (2013) and Mitchell and Jones (2005), to match the modeled data resolution. For both the datasets, mean annual time series data were produced by aggregating the monthly temperature and precipitation data. Appendix 5 (Table A5.1) lists the names of all the CMIP5 models analyzed in the study. Figure A5.1 (Appendix 5) shows the temperature and precipitation anomaly data obtained from the CMIP5 model simulations (as multi-model averages) and CRU-TS observations across the study period for each of the grid cells.
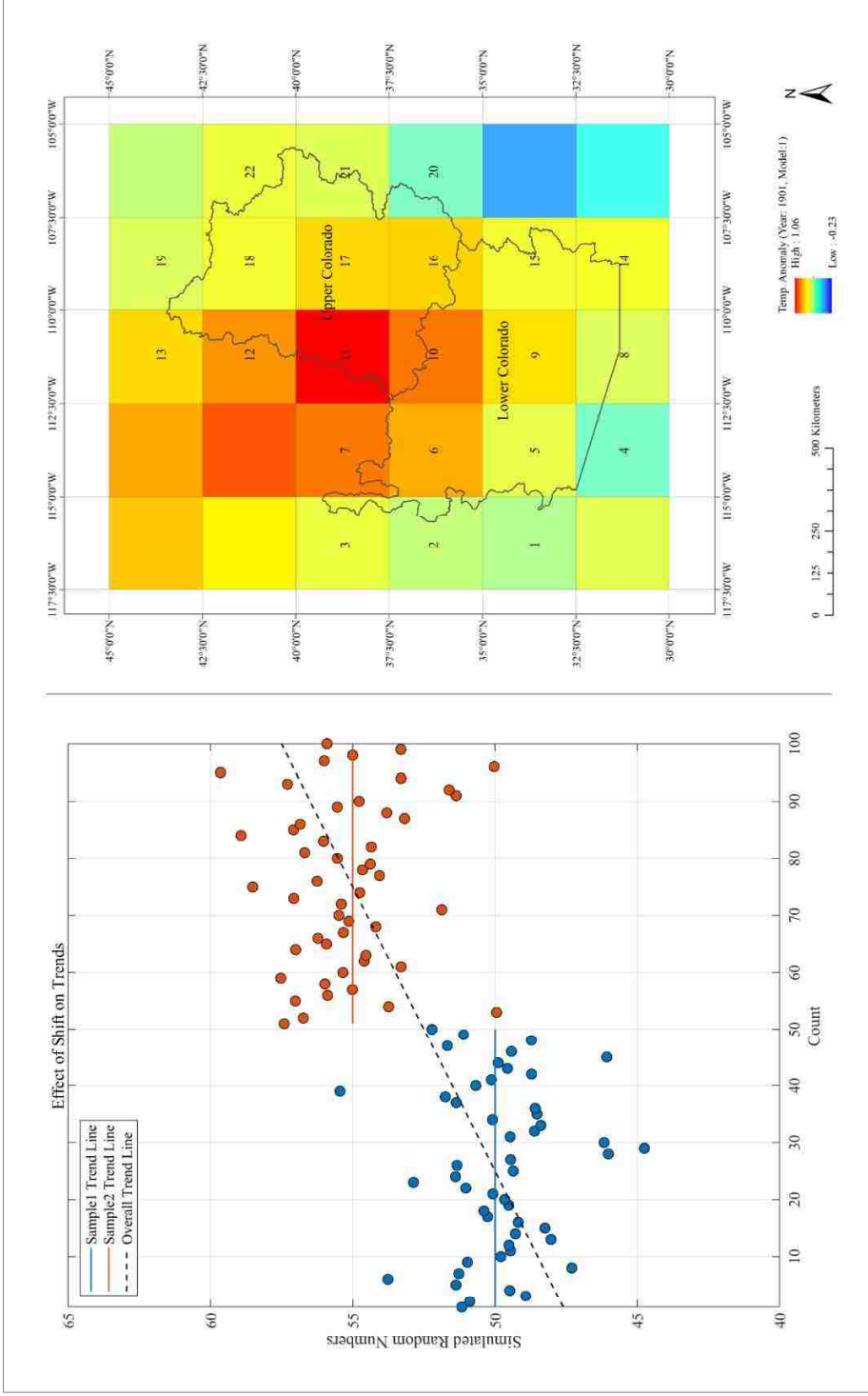
Figure 5. 1: **(Left)** An example showing the effect of a shift point (SP) on trend analysis. The first (blue) and second (orange) samples (drawn from normal distributions), both with a sample size of 50, have a mean of 50 and 55, respectively, with a variance of 5. The blue and orange horizontal lines show the trend lines of the first and second samples, respectively. The black dashed line shows the overall trend line between the two samples ignoring the SP. **(Right)** Map showing the upper and lower Colorado River Basins across the selected grid cells. Each grid cell had 41 temperature and 25 precipitation values (from different simulation models) at each year of the study period (i.e., 1901 to 2004). For example, this map shows the variation in temperature anomaly across the grid cells in the year 1901 in model 1.

111

5.3. Methodology

For the trend analyses, four different versions of the MK test (Mann, 1945; Kendall, 1955), adopted from Kumar et al. (2009), were applied. Similar modified versions of the MK test were found in the literature relating to determination and quantification of trends (Tamaddun et al., 2016). The first version, referred to as the MK1 in the following sections, is the original form of the MK test (Lettenmaier et al., 1994). The second version, referred to as the MK2, is a modified MK test with TFPW, as explained by Yue et al. (2002), and considers the effect of STP or lag-1 autocorrelation in the data distribution. The third version, referred to as the MK3, is a modified MK test that takes into account all the significant autocorrelation structures present in a time series (Hamed and Rao, 1998). The fourth version, referred to as the MK4, is a modified MK test that considers the effect of LTP, also known as the Hurst phenomenon (Hamed, 2008) in the hydrology literature (Koutsoyiannis, 2003). The MK test, at its core, is based on the null hypothesis that the time series has no trend. The test determines the direction of a trend, which can be either positive, negative, or absence of a trend, based on the first MK test statistic (obtained from a signum function). Later, another test statistic is determined (from the first test statistic), which gives the significance level of rejecting the null hypothesis. The modified versions of the MK test, as mentioned earlier, checks for the presence of autocorrelation (Kumar et al., 2009), and based on the type of autocorrelation, either modifies the time series (MK2 applies prewhitening) before determining the significance of the MK test, or adjusts the formula to determine the test statistic (MK3 and MK4). Hence, a time series under MK1 may suggest a trend at a certain significance level, however, the same time series may not be statistically significant under MK2, MK3, or MK4, or vice versa. Besides the MK test, Theil-Sen approach (TSA) (Theil, 1950; Sen, 1968) was adopted to quantify the magnitude of the trends. TSA is

112

nonparametric in nature, hence it is considered appropriate to be applied in conjunction with the MK test. TSA determines the median slope of all the possible pairs in a time series. Thus, the test is robust against possible outliers.

Pettitt's test (Pettitt, 1979), with and without TFPW (Yue et al., 2002), was used to determine the presence of significant SPs in the data distributions, as was suggested by Serinaldi and Kilsby (2015). The Pettitt's test (Pettitt, 1979), at its core, detects the shift (using a signum function similar to the MK test) in a time series by testing the anomaly between the mean of two independent samples from the same time series. The detected shift, which can be either positive, negative, or an absence of a shift, is then tested for a probability estimate based on the significance level used. The TFPW process removes the trend (de-trending) from a time series by subtracting the slope of the trend (Yue et al., 2002) and then removes the serial correlation from the de-trended time series. Hence, with TFPW, the Pettitt's test becomes more reliable in cases of time series with underlying trends. Depending on the presence of a significant SP, each of the time series was divided at the SP, and all the MK tests were applied before and after the SP separately. This approach of detection of an SP and then applying the MK tests prior to and after the SP has been labeled as "Shift-Trend" in the following sections. A confidence level of 90% (significance level of 10% or $p \leq 0.10$) was used for the significance of all the tests.

5.4. Results

5.4.1. Shift-Trends in Temperature Data

The majority of the CMIP5 temperature models at each of the grid cells suggested a positive shift (Appendix 5, column four (+/-) of Table A5.2) between 1940 and 1980 (according to the SPs one standard deviation above and below the mean SP) (Figure 5.2a). The overall range

of the SPs was found to be slightly wider (around 1920 to 1980). The mean SPs of all the CMIP5 models had a significantly narrow range, i.e., between 1960 and 1970, except for the grid cell 11, which experienced an earlier shift. The mode of SPs across the CMIP5 models (Table A5.2) suggest that almost all the grid cells had shift points between 1960 and 1980. A few models at each grid cells showed negative shifts, but the numbers were very few compared to the positive shifts (Table A5.2). The effect of STP on the SPs was found to vary across the grid cells – for some grid cells, the mean SP was shifted by more than a decade (e.g., grid cell 3, and 13-15) (Figure 5.2a).

Comparison between the trends before and after the shifts showed that the total number of models at each grid cells with the positive trends increased by approximately a factor of three after the shifts (last row of Table A5.2). On the contrary, negative trends were hardly observed after positive shifts, even though there were models with negative trends before the shifts. Both MK3 and MK4 had a smaller number of models with trends, whereas MK2 had a higher number of models with trends compared to MK1 (both before and after the SPs) (Table A5.2). The LCRB had a higher number of models with positive trends compared to the UCRB, both before and after the SPs. Contrarily, UCRB had a higher number of models with negative trends compared to the LCRB before the shifts. There was only one model with a negative trend after the SP in the UCRB (under MK1 and MK2), while the negative trends in the LCRB were all neutralized after the SPs (Table A5.2). The effect of positive shifts in the detected trends was also evident from the TSA trend slopes evaluated before and after the shifts. Figures 3a and 3b show that the mean trend slope across the grid cells increased by a factor of 10 after the shift. The median TSA slopes, both before and after SPs, were all found to be positive across the models at each grid cell.

The CRU-TS temperature data showed a higher variation among the SPs across the grid cells as compared to the mean SPs of the modeled data. Almost all the grid cells had a positive SP between 1930 and 1980 (Figure 5.2b). The effect of STP was found to be higher in the CRU-TS data since the majority of the grid cells did not show significant SPs after applying TFPW. Grid cells without a significant SP were infilled by the average of the significant SPs found across the basin (named as the basin-mean-SP) in Figure 5.2b. The effect of shifts in the detected trends was found to be less in the CRU-TS temperature data – especially in MK3 and MK4 – as the total number of grid cells with significant trends were comparable before and after the significant shifts (Appendix 5, Table A5.3). In MK1 and MK2, the number of grid cells with positive trends was close to double after the positive shifts. Except for the two grid cells in the LCRB, the direction of the trends in all the other grid cells was positive, both before and after the positive shifts (Table A5.3). The UCRB had a higher number of grid cells with positive trends compared to the LCRB, which was opposite of what was found among the CMIP5 models. The mean TSA trend slopes across the grid cells showed a significant rise, an increase by a factor of 4, after the positive shifts (Figures 5.3c and 5.3d). The rate of increase in the slope values, from before the shifts to after the shifts, was found to be higher in the central grid cells compared to the eastern and western grid cells.

A basin-wide analysis revealed a noticeable increase in the basin-mean trend slope (obtained by averaging the slopes of all the grid cells within the CRB) after a significant shift – both in the modeled and observed datasets (Figure 5.3e). Though the modeled mean shift (1962) (obtained from averaging all the SPs within the CRB) occurred a decade later than the observed mean shift (1952), the increase in slope after the shift was found to be quite comparable (within the same order and consistent direction) with the observed data. The modeled mean slope

115

changed from +0.0023 to +0.0232 (increased by a factor of 10), while the observed mean slope changed from +0.0038 to +0.0157 (increased by a factor of 4) (Figure 5.3).

5.4.2. Shift-Trends in Precipitation Data

In the CMIP5 precipitation models, it was difficult to conclude on the general direction of the shifts since the number of models with positive and negative shifts at many of the grid cells was comparable (equal in some instances) (Appendix 5, column four (+/-) of Table A5.4). Besides, only a small proportion of the precipitation models showed a significant shift compared to the temperature models (last row of Table A5.4). However, for the entire CRB, a higher tendency towards negative shifts was observed from the analyses. The SPs at each grid cells across the majority of the models were found between 1920 and 1980 (according to the SPs one standard deviation above and below the mean SP as well as in the overall range) (Figure 5.2c). The mean SPs among the models at each grid cells were found within a narrower range (i.e., between 1930 and 1960). There was no significant mode among the SPs across the models (Table A5.4). The effect of STP was found to be higher among the CMIP5 precipitation models, as TFPW shifted the mean SPs by more than a decade for some of the grid cells, e.g., cells 3-5, cell 11, and cells 14-16 (Figure 5.2c).

A neutralizing tendency, in terms of the direction of the trends, was observed between the trends before and after the shifts. The number of models with positive trends after the shifts was reduced to close to one half compared to before the shifts (last row of Table A5.4). Models with negative trends were hardly present after the shifts, except for one model under the MK3 in the UCRB. MK1, MK2, and MK4 had comparable results – both before and after the shifts (Table A5.4). MK3 had the highest number of models both with positive and negative trends. The
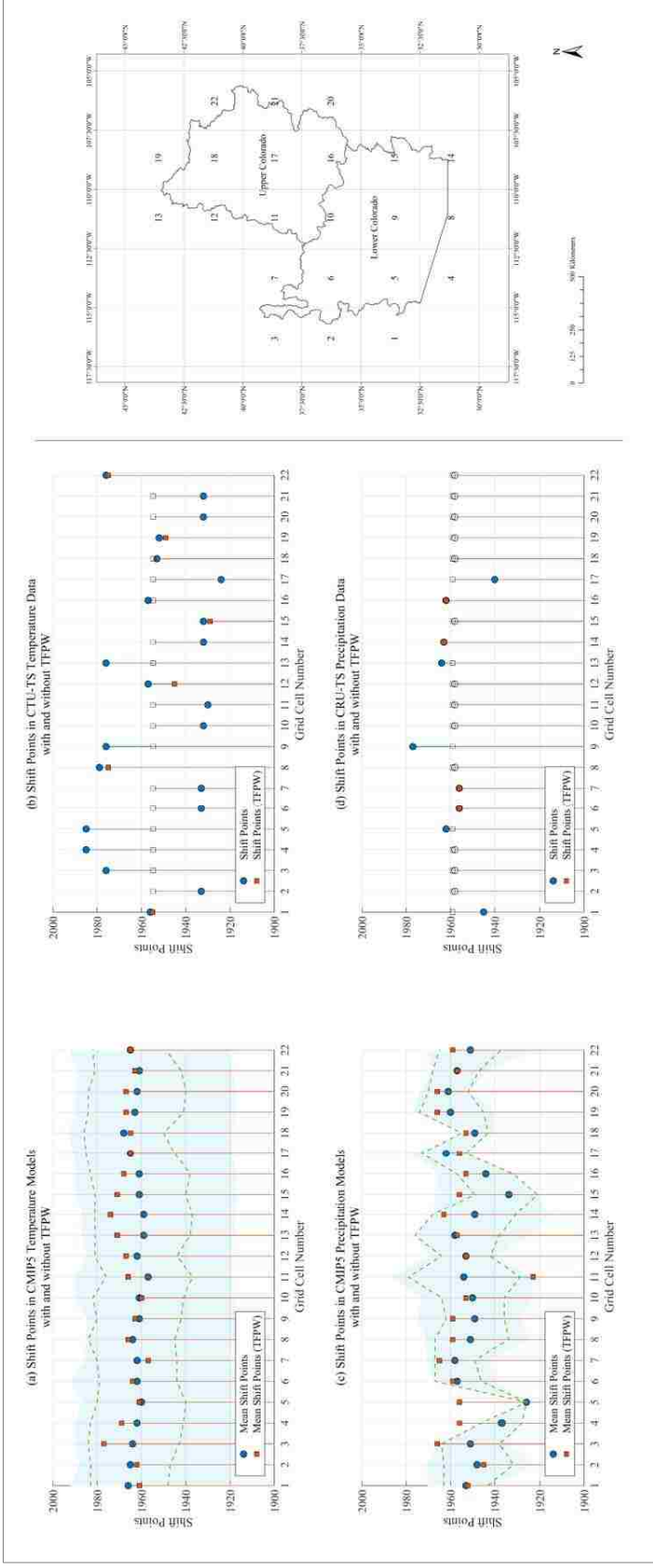
Figure 5. 2: Plots showing the shift points (SPs) in the CMIP5 and CRU-TS temperature (**a** and **b**) and precipitation (**c** and **d**) data across the grid cells with (orange) and without (blue) the trend-free-pre-whitening (TFPW). The light blue shaded regions, in (**a**) and (**c**), delineate the range of SPs among all the CMIP5 models. The green dashed lines, in (**a**) and (**c**), mark one standard deviation above and below the mean SP detected across the CMIP5 models. For visual comparison, grid cells without a significant SP, at $p \le 0.10$, in (**b**) and (**d**), were infilled with the basin-mean-SP. Filled and unfilled symbols, in (**b**) and (**d**), refer to significant and insignificant SPs, respectively, at $p \le 0.10$. Grid cells 1-10, 14, and 15 are located in LCRB, while grid cells 11-13, and 16-22 are located in UCRB. (**Right**) Map showing the position of the grid cells in UCRB and LCRB.

117

LCRB had a higher number of models with positive trends both before and after the shifts than the UCRB (Table A5.4). The LCRB also had a higher number of models with negative trends before the shifts, but all the trends were neutralized after the shifts. From the TSA trend slopes, it was difficult to determine the general direction of the precipitation trends across the grid cells (Figures 4a and 4b). Before the shifts, the mean TSA slope was found to be slightly above zero, with the eastern and western grid cells having relatively positive slopes and the central grid cells having relatively negative slopes. After the shifts, the mean TSA slope was found to increase, but that increase can be attributed to the absence of significant SPs in many of the modeled data distributions – which overestimated the overall mean trend across the CRB. The TSA slopes after the shifts showed a higher rate of increase among the central grid cells compared to the eastern and western grid cells.

The effect of STP was not conclusive as for the majority of the grid cells (Appendix 5, Table A5.5) – both with and without TFPW – did not show significant SPs in the CRU-TS precipitation data (Figure 5.2d). The results of the different versions of the MK tests were quite similar and showed only negative trends both before and after the shifts. In fact, MK1, MK2, and MK4 had exactly the same results (Table A5.5). The majority of the shifts were found to be positive, which neutralized the pre-existing negative trends and resulted in the absence of trends after the shifts. The LCRB had a higher number of grid cells with negative trends compared to the UCRB – both before and after the shifts (there was only one grid cell with negative shift in the LCRB after the shift) (Table A5.5). The mean TSA slope across the grid cells before the shifts was close to zero (slightly negative) (Figure 5.4c). Many of the grid cells did not have a significant shift, which produced inconsistency in the estimation of trend slopes. As the grid cells without significant shifts had no trend after the shift (such grid cells had a trend for the entire

118

study period represented as a trend before the shift in Figure 5.4c), those cells did not contribute in calculating the mean slope after the shift – and hence, those cells fell on the no trend line in Figure 5.4d (shown by unfilled symbols). Therefore, the mean slope was found to decrease after the shift since the negative slopes were found to be of higher magnitude compared to the positive slopes among the grid cells with significant shifts (Figure 5.4d). A higher magnitude of negative slopes among a handful number of grid cells (all the grid cells did not have a significant shift) may have created a negative bias in the mean slope after the shift. The eastern grid cells, both before and after the shifts, showed fewer slopes compared to the western grid cells. Many of the grid cells that did not show a significant SP had positive trends across the entire study period.

The basin-wide analysis did not produce a satisfactory comparison as the basin-mean slopes (obtained by averaging the slopes of all the grid cells within the CRB) were found to be inconsistent between the modeled and observed datasets. The modeled data showed an increase (from 0.0091 mm/year to 0.0195 mm/year) in the basin-mean slope (obtained from averaging all the SPs within the CRB) while the observed data suggested a decrease (from -0.0039 mm/year to -0.0109 mm/year) (Figure 5.4e). Unlike the temperature models, precipitation models experienced the mean shift (obtained from averaging all the SPs within the CRB) earlier (1951) than the observed shift (1958) (Figure 5.4e). The distribution of the observed data revealed that the grid cells with decreasing trends had a higher influence on the basin-wide mean.
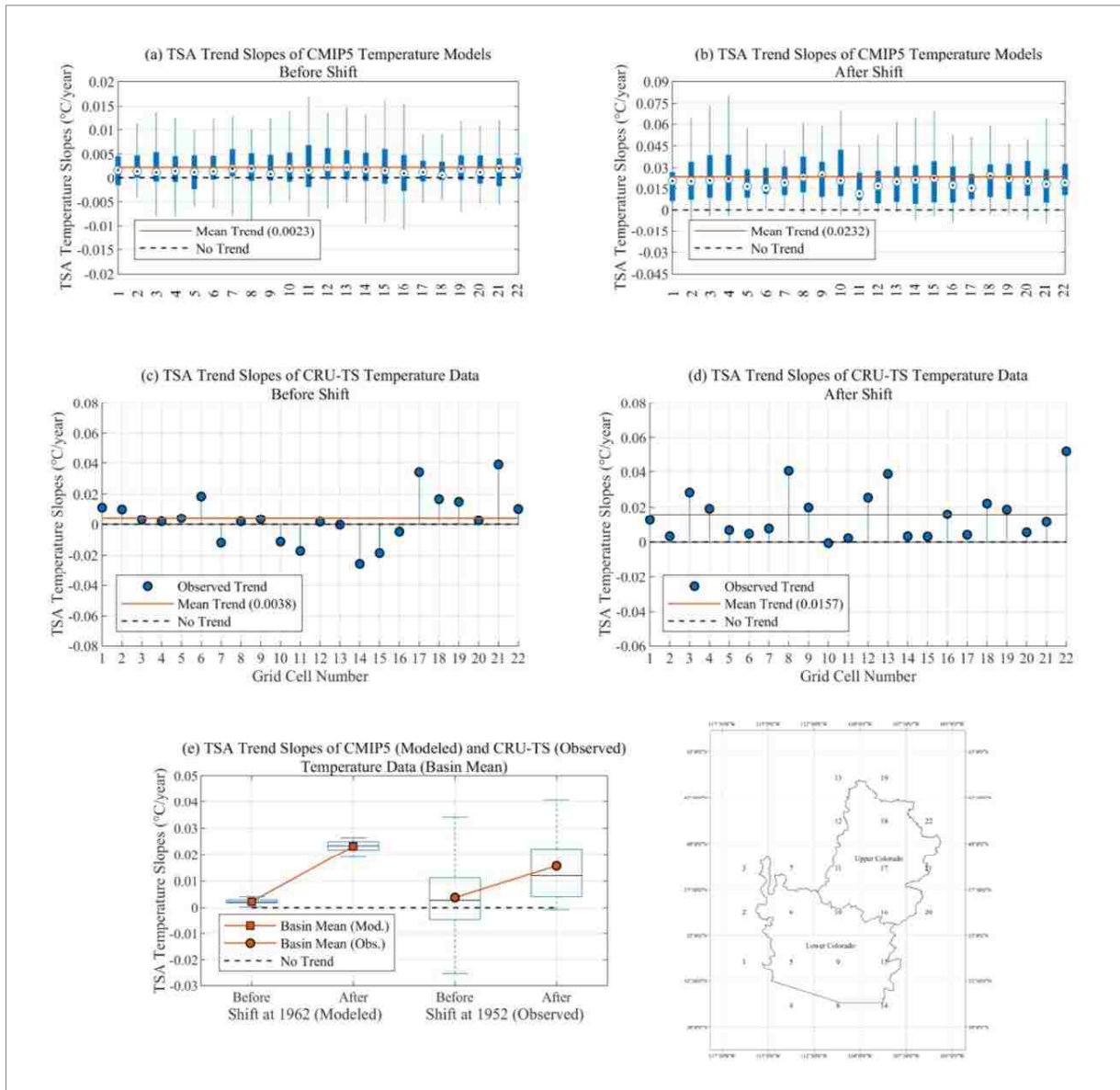
Figure 5. 3: Box plots showing the distribution of the Theil-Sen approach (TSA) trend slopes across the CMIP5 (**a** and **b**) and CRU-TS (**c** and **d**) temperature data before and after a significant shift at each of the selected grid cells. The black (dashed) horizontal lines mark the "No trend" line. The orange lines show the average TSA trend slope across all the grid cells. (**e**) Plots showing the basin-mean TSA slope before and after the shift in the CMIP5 and CRU-TS temperature data. The orange line connecting the basin means, before and after the shift, shows the change in slope due to the shift. The box plots in (**e**) show the distribution of the SPs across all the grid cells for visual comparison. The box plots show the 25th, 50th, and 75th percentile, while the whiskers represent the minimum and maximum values. Grid cells 1-10, 14, and 15 are located in LCRB, while grid cells 11-13, and located 16-22 are in UCRB. (**e**) 95% confidence intervals of the basin mean slope for the CRU-TS data (CMIP5 models) before and after the shift were -0.0027 to 0.0104 (0.0019 to 0.0027) and 0.0097 to 0.0216 (0.0223 to 0.0241) °C/year, respectively.

120

5.5. Discussion

The ability of CMIP5 simulation models to match the observed trends under the influence of shifts and persistence was evaluated in this study. The Pettitt's test, preceded by TFPW (Yue et al., 2002) was used to detect the significant SPs, as was suggested by Serinaldi and Kilsby (2015). Compared to the CMIP5 temperature models, the precipitation models experienced a higher influence of STP (Figures 2a and 2c) as the mean SP of some of the grid cells moved by more than a decade after the TFPW. Such movement in SP can be attributed to the absence of significant SPs in some of the modeled data distributions after applying TFPW – which can produce a bias in the mean SP. In the observed data distributions, the effect of STP was higher as the majority of the grid cells did not show any significant SP after TFPW (Figures 2c and 2d). However, for such grid cells having SPs both before and after TFPW, the locations of the SPs were found to be comparable. The results suggest that the effect of STP was higher in both the modeled and observed precipitation data compared to the temperature data. Other prewhitening techniques, e.g., AR(1)-based prewhitening and fGn-based prewhitening, can be evaluated in future studies to verify the obtained results. However, the results may not vary significantly as was suggested by Serinaldi and Kilsby (2015).

The CMIP5 temperature models had a narrower range of mean SPs compared to the observed data (Figure 5.2). Furthermore, the temperature models showed the tendency of detecting significant SPs at a later date compared to the observed data. The variation of SPs among the adjacent grid cells was much higher in the CMIP5 precipitation models compared to the temperature models. The results of the modeled and observed precipitation datasets were not highly comparable as many of the grid cells in the observed data did not have a significant SP. Contrary to the temperature models, the precipitation models detected the SPs earlier than the

observed SPs. Such a tendency was also evident from the basin-wide shift of temperature and precipitation (Figures 3e and 4e). This suggests an overall bias (a tendency of detecting shifts earlier or later than the observed shifts) in the modeled data distributions.
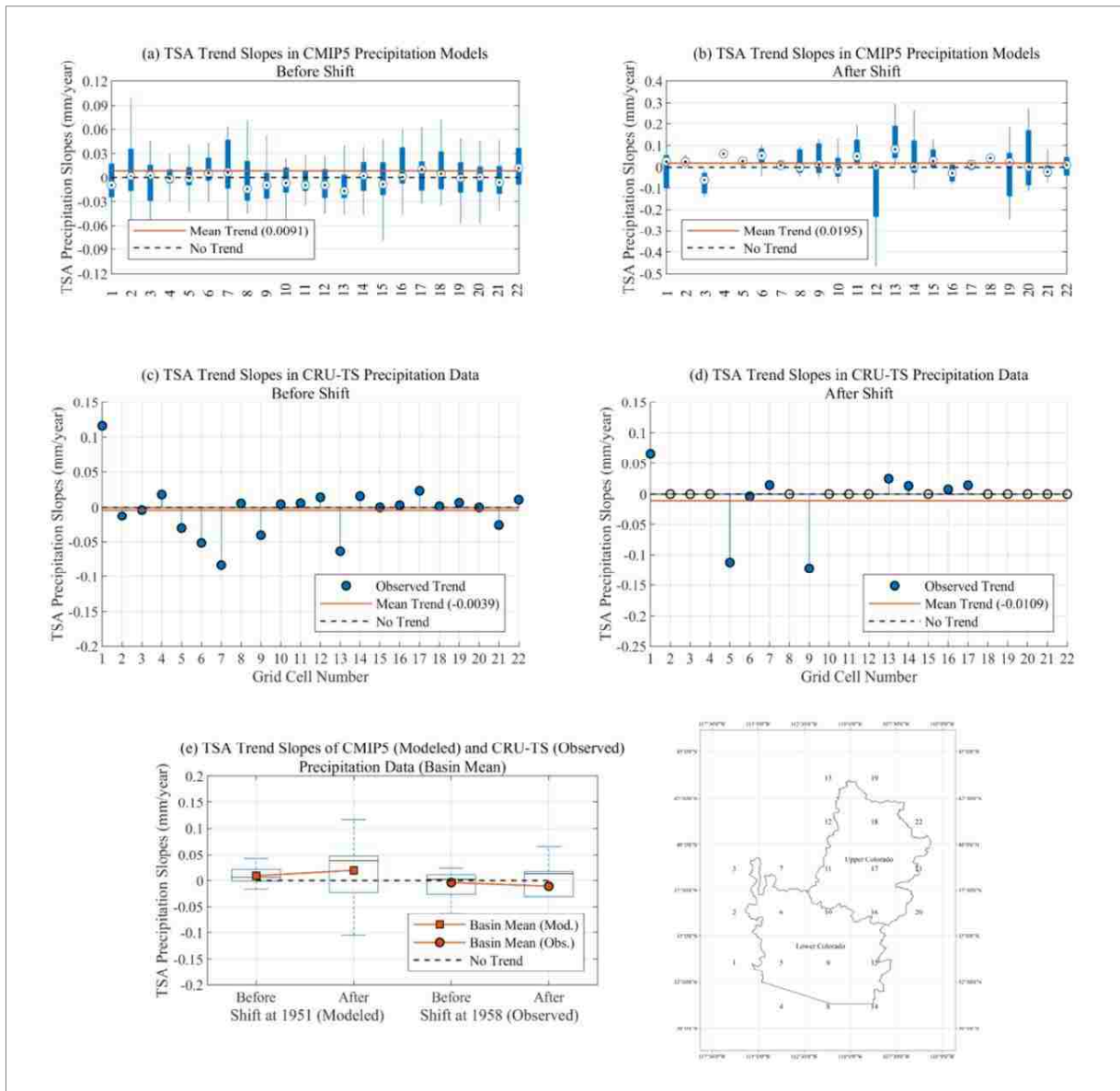
Figure 5. 4: As in Figure 5.3, but for precipitation data. For visual comparison, grid cells without a significant SP, at $p \leq 0.10$, in (**d**), were infilled with zero slopes (no trend), as shown by unfilled symbols. Grid cells 1-10, 14, and 15 are located in LCRB, while grid cells 11-13, and 16-22 are located in UCRB. (**e**) 95% confidence intervals of the basin mean slope for the CRU-TS data (CMIP5 models) before and after the shift were -0.0201 to 0.0124 (0.0026 to 0.0155) and -0.0522 to 0.0305 (-0.0027 to 0.0416) mm/year, respectively.

122

The analyses suggest that the SPs across the grid cells (also the basin-mean-SP) were located within a range of a few decades for both the temperature and precipitation models. Previous studies have looked into the correspondence between the phases of large-scale climate variabilities originating from the SST fluctuations (i.e., El Niño Southern Oscillation, Pacific Decadal Oscillation, and Atlantic multidecadal oscillation) and the station-based hydro-climatological data of the CRB (Tamaddun et al., 2017; Kalra et al., 2017; Nowak et al., 2012). The obtained results were found to be fairly consistent with the shifts observed in the previous studies (Pathak et al., 2017; Rahaman et al., 2019). The range of results among the models and their inherent uncertainty due to natural climate variability was discussed by Deser et al. (2012a and b), which may explain the comparable SPs across the models. The study also mentions the importance of large-scale fields on the downscaled local climate models. Future studies may consider the findings of the study in inter-model and inter-variable analyses of the models as a response to large-scale climate variabilities.

The effect of persistence on trends was found to be consistent between the variables in the modeled and observed datasets. Both the temperature datasets (modeled and observed) were more greatly influenced by STP as TFPW (MK2) increased the number of significant models when compared to MK1, while the numbers of significant models were fewer in MK3 and MK4 (Tables A5.2 and A5.3). The precipitation data distributions were found to be highly influenced by the significant autocorrelation structures with a higher number of significant models in MK3 compared to the other MK tests (Tables A5.4 and A5.5). Studies suggest that the effect of persistence can have different associations among correlated variables even within a particular region (Kumar et al., 2009). The consistency between the modeled and observed datasets

observed in the persistence of a variable can be compared to other hydrologic basins to evaluate its uniformity across a larger study area in future studies.

The effect of shifts on the detected trends was found to be much higher in temperature compared to the precipitation datasets. The positive shifts in the temperature datasets increased the trend slopes significantly after the shifts. The slopes – both before and after the shifts – were found to be fairly consistent between the modeled and observed datasets. However, the rate of increase, from before the shift to after the shift, was higher in the CMIP5 models. Before the shifts, the slopes varied from the eastern to the western grid cells, but they were found to be consistent (all positive) after the shifts, which suggests a basin-wide shift towards a positive trend in both the modeled and observed datasets. Though CMIP5 temperature models overestimated the magnitude of the trend, both before and after the shifts, the models satisfactorily captured the observed trend slopes.

In the precipitation datasets, the absence of significant SPs may have led to a bias in the estimation of trends since the effective number of grid cells (while calculating the mean slope) was inconsistent between the modeled and observed distributions as well as between before the shift cases and after the shift cases (Figure 5.4). Some of the CMIP5 models did not have a significant SP, which overestimated the variance of the trend slopes and may have produced biased results. A similar occurrence of bias was found in the observed data as many of the grid cells did not have a significant SP. Though the trend slopes between the modeled and observed datasets were incomparable (and hence inconsistent), both the datasets showed a lack of SPs in their distributions. This suggests that the precipitation and temperature trends in the CRB did not experience identical changes over the study period. The presence of shifts, in strengthening or neutralizing an existing trend, was much higher in the temperature trends compared to the

124

precipitation trends. The influence of modeled and observed datasets varied across the UCRB and LCRB without any noticeable consistency within the variables. However, before the shifts, especially in the temperature data, the eastern and western grid cells showed higher slopes, while after the shifts, the central grid cells showed higher slopes. The observed variation from east to west can be a scope of research for future studies.

5.6. Conclusions

This study evaluated the effects of SPs and persistence on the trend analyses of the CMIP5 temperature and precipitation models for the entire CRB across 104 years. The obtained results were compared against the observed CRU-TS datasets. The results showed that the trends in temperature models were relatively consistent with the observed trends – both in the direction and magnitude. For both the precipitation datasets, the absence of significant SPs in many of the grid cells led to incomparable and inconsistent results. The variation in SPs among the adjacent grid cells was higher in the modeled precipitation and observed temperature data. Both the temperature datasets showed a higher influence of STP in their detected trends (MK2), while both the precipitation datasets were highly influenced by the significant autocorrelation structures of the time series (MK3).

The major contributions of this study are:

- A shift-trend approach was adopted where the direction and magnitude of the trends were evaluated independently before and after significant SPs for both the modeled and observed datasets. This allowed the current study to evaluate the effect of shifts in strengthening or neutralizing the pre-existing trends.

- The effect of persistence was thoroughly examined not only for the trend tests but also for the detection of SPs. The trend analyses revealed that the effects of persistence varied between the variables, but they were consistent between the modeled and observed datasets. The SPs were found to be influenced by persistence in both the datasets with higher influence on the observed datasets.

- The inconsistencies detected between the CMIP5 and observed datasets – under the influence of SPs and persistence – can be helpful in improving the models. The observed biases can be helpful to practitioners who highly depend on data-driven modeling.

Future studies may look into the uncertainties related to large-scale climate variability and the modeled distributions. The inclusion of multiple ensemble members can also be another scope of research. Comparing the results with adjacent hydrologic basins may provide important insights regarding other possible biases in the CMIP5 models.

CHAPTER 6: CONTRIBUTIONS AND RECOMMENDATIONS

6.1. Summary

Climate warming has affected hydrologic processes in various ways – one of them involves changes in the behavior and intensification of the hydrologic cycle. The adverse consequences of these changes have increased under the changing climate as the rapid increase in population stresses limited water resources. Water managers have expressed concerns regarding the aftermath associated with access to fresh water as a response to the change in climate. Hence, the primary objective of the work presented in this dissertation was to evaluate the change patterns, i.e., a gradual change known as the trend, and an abrupt change known as the shift, of multiple hydro-climatological variables, namely, streamflow, SWE, temperature, precipitation, and PET, in association with the large-scale oceanic-atmospheric climate signals. Moreover, both observed datasets and modeled simulations were used to evaluate such change patterns to assess the efficacy of the modeled datasets in emulating the observed trends and shifts under the influence of uncertainties and inconsistencies. A secondary objective was to utilize the detected change patterns in designing data-driven prediction models, e.g., ANN, SVM, and GPR models, coupled with data pre-processing techniques, e.g., PCA and WT. The study was not solely limited to the hydrologic regions of the conterminous U.S.; rather it was extended to include an analysis of northern India to appraise the differences in the spatiotemporal variation on a broader scale.

The first task examined two research questions: (1) What are the spatiotemporal trend and shift patterns of the conterminous U.S. streamflow in association with large-scale oceanic-atmospheric climate signals across multiple frequency bands? (2) How effective are data-driven

models, e.g., ANN, SVM, and GPR, when coupled with data pre-processing techniques, e.g., PCA and WT, in predicting short-term streamflow behavior? The task was based on the research basis that detection of trends and shifts across multiple frequency bands may provide a better understanding of the nature of the change patterns, especially when such changes have been found to be associated with the oscillatory behavior of large-scale oceanic-atmospheric climate signals such ENSO, PDO, and AMO. Since these signals contain multiple frequency components and alternating phases when changing over a long time, associating the streamflow change patterns with these signals across various frequency bands can be of significant importance. The detected intra-variation and inter-covariation between streamflow and the climate signals across multiple frequency bands may have the potential to improve the predictive ability of the data-driven models, e.g., ANN, SVM, and GPR, when coupled and designed properly. Hence, the study analyzed water year and seasonal trends and shifts (along with their DSs) in 237 unimpaired streamflow stations across the continental U.S. from 1951 to 2012. The spatiotemporal association between regional streamflow patterns and three large-scale climate signals were assessed using WTC. The major findings and the summary results of this task were: positive (negative) trends and shifts in the water year and its DSs were significant in the northeastern and north-central (northwestern and southeastern) regions; a few central regions showed both directional trends and shifts. This was not common since most of the regions showed spatial coherency in terms of the trend and shift direction; seasonal trends and shifts suggested unique spatial patterns in the original time series as well as in their DSs. Fall and spring showed the highest positive and negative trends and shifts, respectively, suggesting a behavioral change at the end of these two seasons. The number of significant stations with trends and shifts increased as the DSs went higher, with the maximum in DS8. Shifts showed an

oscillating behavior in DS8 – which led to the hypothesis that such behavior at higher SBs was correlated to the frequency components of the climate signals; ENSO showed a higher correlation with the regional streamflow in CS8 to CS16, while both PDO and AMO showed higher correlations in the lower CSs (below CS4) and beyond CS16; the relative phase relationship suggested a uniform lag-response behavior (either in-phase or a lag of one quarter) between significant regional streamflow patterns and ENSO. For PDO and AMO, no such consistency was observed. Comparison among the ANN, SVM, and GPR models, preceded by PCA and WT, produced comparable results with significant accuracy in predicting short-term streamflow behavior.

The second task inspected two research questions: (1) How do the large-scale oceanic-atmospheric climate signals originating from the Pacific Ocean affect the western U.S. SWE across multiple frequency bands? (2) Which regions of the western U.S. have maintained a consistent phase relationship, in terms of SWE, with the large-scale climate signals originating from the Pacific Ocean; and how does the lag-response behavior change across multiple frequency bands? This task was formulated based on the assumption that association between regional western U.S. SWE and the large-scale oceanic-atmospheric climate signals originating from the Pacific Ocean, e.g., ENSO and PDO, can be better explained in their frequency components since these signals contain multiple frequency components. Such signals also alternate between phases when changing over a long time. The detected correlation between SWE and the climate signals across multiple frequency bands may provide a better insight into their spatiotemporal relationships and may explain their phase relationships with greater detail. Hence, the study examined the correlation between ENSO/PDO and the western U.S. SWE over a study period of 56 years using CWT and its derivatives. Application of such methods allowed

129

the study to analyze and correlate regional SWE with oceanic-atmospheric climate indices across multiple timescale bands. The analysis revealed the following: ENSO, compared to PDO, had a much higher influence on SWE. The temporal associations were observed to be stronger in the higher timescale (lower frequency) bands. The effect of ENSO/PDO varied significantly across the adjacent hydrologic regions; regions close to the ocean (inland) and lower (higher) in elevation were observed to show a higher (lower) correlation with ENSO/PDO.

The third task investigated two research questions: (1) What are the spatiotemporal trends and shift patterns of temperature, precipitation, and potential evapotranspiration in the north Indian monsoon (and its comprising months) across the last century during the phases of ENSO? (2) What is the rate of change (slope) of the trends and how are the trends distributed (apportioned) along the years and through the months of monsoon? Large-scale oceanic-atmospheric climate signals, such as ENSO and their phases have been found to influence global hydro-climatological patterns in various ways based on the geography and the seasonal variation of a region. Among the different regions of India, the northern part of the country has been observed to experience many different climate extremes, e.g., storms, droughts, and floods, over the years. Since monsoon is the single most important season for the region, evaluation of the temperature, precipitation, and PET patterns (both trends and shifts) across the last century, especially during the various phases of ENSO, can be of great value to regional water management. A proper quantification, e.g., the rate of change and apportionment, of the trends can also be helpful in evaluating temporal variation across the years and through the months of monsoon, which lasts from June to September. Moreover, as the literature suggests, the multi-variable analyses approach adopted in this task may help investigators to understand the response of regional hydrology to large-scale climate signals such as ENSO. Hence, in this task, three

hydro-climatological variables, i.e., temperature, precipitation, and PET, were analyzed over a century-wide period (from 1901 to 2002) to evaluate the influence of various ENSO phases on the change patterns across North India during the monsoon season. Trend and shift patterns in 146 districts in eight North Indian states were analyzed, and the annual and the seasonal (monsoonal) apportionment entropy that quantified the temporal distributions of the change patterns were evaluated. Besides the effects of ENSO, the all-year (century-wide) monsoonal change patterns were analyzed to determine the effect of each of the monsoonal months on the long-term patterns. Results suggested that the El Niño years, compared to the La Niña and neutral years, had a much greater influence on the change patterns of the variables. The all-year monsoonal change patterns suggested a significant decrease in the temperature and PET trends and shifts across North India, while the precipitation change patterns (both increasing and decreasing) were found to be region-specific. The entropy analyses suggested that the highest variation in the long-term change pattern occurred in precipitation data, whereas temperature and PET experienced more variation during the monsoon season compared to changes over the years.

The fourth and final task examined two research questions: (1) What are the direction and magnitude of temperature and precipitation trends in the CRB along the last century in the observed and modeled (CMIP5) gridded datasets? (2) How do the shifts alter the direction and magnitude of the trends and what are the influences of various types of persistence, e.g., short and long-term autocorrelation, on the observed and modeled trends? Comparison between observed and modeled datasets provides a set of qualitative and quantitative metrics to evaluate the accuracy of the modeled datasets, especially when such modeled datasets are heavily used for hydro-climatological prediction, such as the CMIP5. Assessment of trends (both in direction and magnitude) in the observed and modeled datasets can be helpful in correcting the bias (if any) in

131

the modeled datasets. Moreover, such trends can highly be influenced by the presence of shifts, which can alter or moderate an existing trend. An undetected shift may result in a poor estimation of a trend. Besides, the presence of persistence, i.e., autocorrelation in data, can overestimate a trend unless it is removed before the application of trend detection tests. Hence, this study evaluated the effects of SPs and persistence on the trend analyses of the CMIP5 temperature and precipitation models for the entire CRB across 104 years. The obtained results were compared against the observed CRU-TS datasets. The results showed that the trends in temperature models were relatively consistent with the observed trends – both in the direction and magnitude. For both the precipitation datasets, the absence of significant SPs in many of the grid cells led to incomparable and inconsistent results. The variation in SPs among the adjacent grid cells was higher in the modeled precipitation and observed temperature data. Both the temperature datasets showed a higher influence of STP in their detected trends (MK2), while both the precipitation datasets were highly influenced by the significant autocorrelation structures of the time series (MK3).

6.2. Contributions

The first task analyzed water year and seasonal trends and shifts (along with their DSs) in 237 unimpaired streamflow stations across the continental U.S. from 1951 to 2012. The spatiotemporal association between regional streamflow patterns and three large-scale climate signals were assessed using WTC. Major contributions of this task are: detection of trends and shifts of the conterminous U.S. streamflow in the original as well as decomposed time series of the water year and seasonal data using non-parametric statistical tests; determination of spatiotemporal association between the regional streamflow and large-scale oceanic-atmospheric climate signals originating from both the Pacific and Atlantic Oceans; testing of data-driven

models coupled with data pre-processing techniques to predict short-term streamflow behavior; and evaluation of relative phase relationships (lag-response behavior) among the climate signals and the regional streamflow across multiple time scales along the study period. This is the first study in the documented literature that couples trend and shift detection tests with spectral component (frequency) analyses on a continental scale, and analyzes the change patterns in association with multiple large-scale climate signals. Such robust analyses may help explain the physical mechanisms of the oceanic-atmospheric systems that affect the U.S. streamflow. The results may also be useful in developing forecasting models based on the multi-resolution associations observed in the study, which may lead to making better water management decisions.

The second task examined the correlation between ENSO/PDO and the western U.S. SWE over a study period of 56 years using CWT and its derivatives. Application of such methods allowed the study to analyze and correlate regional SWE with oceanic-atmospheric climate indices across multiple timescale bands. Major contributions of this task are: multi-scale correlational analysis of the western U.S. SWE, both state-wise and hydrologic region-wise, in response to Pacific Ocean climate signals; and evaluation of relative phase relationships (lag-response behavior) among the climate signals and the regional western U.S. SWE across multiple time scales along the study period. The record length used in this study is a major extension in terms of the number of stations and the length of data analyzed, compared to previous studies using similar datasets. CWT was used to observe the variability in data, and XWT and WTC were used to illustrate and quantify, respectively, the high common power (association) between the representative time series of the variables. Such an approach has not been used previously with SWE data. This study also compared the association of ENSO/PDO

133

across the western U.S. hydrologic regions, which broadened the scope of the study since the results can be beneficial to regional water managers as well.

In the third task, three hydro-climatological variables, i.e., temperature, precipitation, and PET, were analyzed over a century-wide data (from 1901 to 2002) to evaluate the influence of various ENSO phases on the change patterns across North India during the monsoon season. Trend and shift patterns in 146 districts in eight North Indian states were analyzed, and the annual and the seasonal (monsoonal) apportionment entropy that quantified the temporal distributions of the change patterns were evaluated. Besides the effects of ENSO, the all-year monsoonal change patterns were analyzed to determine the effect of each of the monsoonal months on the long-term patterns. Major contributions of this study are: evaluation of the long-term trend and abrupt shift patterns of temperature, precipitation, and PET across north India at the various ENSO phases using non-parametric statistical tests; determination of the spatiotemporal relationships between the selected variables during monsoon and at each of the monsoonal months over a century-wide period; comparison between the major shift points during monsoon and the phases of ENSO, which might have resulted in extreme events, e.g., flood or drought, throughout the study period; and analyses of entropy (apportionment entropy) to quantify how the detected variations were distributed temporally over the years (annually) and during the months (seasonally) of monsoon along the study area. Moreover, major physical and dynamic relationships affecting the monsoon season due to the change in ENSO phases in the Indian subcontinent were compiled and discussed in this task based on an extensive literature review. The obtained results may help practitioners to prepare for flood and drought risks as a response to the changes in ENSO phases.

The final task evaluated the effects of SPs and persistence on the trend analyses of the CMIP5 temperature and precipitation models for the entire CRB across 104 years. The obtained results were compared against the observed CRU-TS datasets. The major contributions of this task are: adoption of a shift-trend approach where the direction and magnitude of the trends are evaluated independently before and after significant shift points for both the modeled and observed datasets; a thorough examination of the effect of persistence not only for the trend tests but also for the detection of shift points; and determination of the inconsistencies detected between the CMIP5 and observed datasets – under the influence of shift points and persistence. This task detected certain biases in the CMIP5 models in detecting the SPs (tendency of detecting shifts earlier or later than the observed shifts) and also in quantifying the trends (overestimating the trend slopes) – such insights may be helpful in evaluating the efficacy of the simulation models in capturing observed trends under uncertainties and natural variabilities.

6.3. Limitations

Though all the tasks attempted to take a robust approach when it came to formulating the underlying research basis and in selecting and designing the appropriate methods to analyze the data, certain limitations were still unavoidable. Data availability restricted the first task to analyze with high certainty (or adequate resolution) beyond DS8 for DWT and beyond CS16 for WTC. Hence, associating streamflow variations with climate signals having multidecadal frequency components was not possible in this task. Moreover, not all the hydrologic regions had a sufficient number of stations within them to provide an explanation of the regional change pattern.

Similar to the first task, since the second task analyzed timescales up to the 16-year band only, significant intervals at higher timescales may have been missed. This task also did not analyze beyond the 16-year band since the results beyond this band had high uncertainty due to the limitation of the length of the period of record. Analyzing a longer-reconstructed time series may allow evaluating the associations at higher timescales with greater certainty.

For the third task, the relationships obtained and the trends detected were purely based on the analyses of obtained data – which are in many cases subject to collection and calibration error (especially for the regions outside the U.S.). Even though the obtained results were compared against some of the studies concerning with the major physical and dynamic factors affecting the monsoon season, none of those factors were directly considered in the study. Other variables, which may affect the Indian monsoon, e.g., wind direction and velocity, heat fluxes over land masses, and coupling of multiple climate signals originating from different oceans, were not considered in the study.

In the fourth task, the uncertainties related to large-scale climate variability were not considered while comparing the modeled and observed distributions. Besides, among the many ensemble members of the CMIP5 simulation models, only the first ensemble members from each model were tested. The inclusion of multiple ensemble members could be a task for future research. Moreover, comparisons were only made between the modeled and observed datasets of the CRB – other hydrologic regions may not show similar associations and biases in the modeled datasets under uncertainties.

Finally, the results reported are statistical in nature; hence, in some cases, the detected relationships or the evaluated change patterns may be counter-intuitive. The outcomes of

statistical tests are helpful in understating the relationships. However, one must be cautious while interpreting the results, as outcomes from statistical tests can on occasion produce a Type I 'false positive' error, depending on the chosen level of significance.

6.4. Recommendations for future work

The primary objective of the work presented in this dissertation was to evaluate the change patterns, i.e., a gradual change known as the trend, and an abrupt change known as the shift, of multiple hydro-climatological variables, namely, streamflow, SWE, temperature, precipitation, and PET, in association with the large-scale oceanic-atmospheric climate signals, i.e., ENSO, PDO, and AMO. Moreover, both observed datasets and modeled simulations were used to evaluate such change patterns to assess the efficacy of the modeled datasets in emulating the observed trends and shifts under the influence of uncertainties and inconsistencies. A secondary objective of this study was to utilize the detected change patterns in designing data-driven prediction models, e.g., ANN, SVM, and GPR, coupled with data pre-processing techniques, e.g., PCA and WT. However, there are a few aspects of the study that could be improved for greater validity in the results or to apply the results in future work. Future extension or replication of similar techniques should consider the following improvement opportunities:

- For both the first and the second tasks, decomposing to higher SBs can be helpful in associating streamflow or SWE variations with climate signals having multidecadal frequency components. In addition, working with a higher number of stations with longer records may provide a better explanation of the regional change patterns.

137

- Application of data-driven models coupled with data pre-processing techniques could be replicated for other regions and with different hydro-climatological variables to test the effectiveness of the methods, algorithms, and model architectures.

- For the third task, other factors, which may affect the Indian monsoon, e.g., wind direction and velocity, heat fluxes over land masses, and coupling of multiple climate signals originating from different oceans, could be considered to increase confidence in the obtained relationships.

- For the fourth task, future studies may look into the uncertainties related to large-scale climate variability and the modeled distributions. The inclusion of multiple ensemble members could be a task for research. Comparing the results with adjacent hydrologic basins may provide important insights regarding other possible biases in the CMIP5 models.

- The detected associations among the climate signals and multiple hydro-climatological variables can be evaluated and/or simulated with physically-based or pseudo-physically-based models to understand the underlying mechanisms with higher precision.

- As all the results reported in these tasks are statistical in nature and are based completely on the quality of the obtained data and the accuracy of the methods used in the respective tasks, any extension in terms of data availability, and/or modification of test methods for a more robust and comprehensive analysis is always a future prospect of research.

APPENDICES

Appendix 1

Chapter 1 has no additional/supplementary material.

Appendix 2.A

The original water-year and seasonal data were decomposed into a set of relatively simpler subseries known as approximation coefficients (AC) and detail coefficients (DC) by putting them through a low pass and high pass filter, respectively. The resulting subseries corresponded to the lower frequencies and higher frequencies of the original time series. At each decomposition level, the resulting DC corresponded to the lower DS, while the resulting AC was further decomposed to obtain a new set of DC and AC. This process was continued until the ACs produced a sufficient resolution (certainty). Three DSs, named as DS2, DS4, and DS8 represented the time-series data at the SBs of two, four, and eight years, respectively. Based on the literature cited in the main text, the SBs were obtained at every 2^n scale, where n is the decomposition level with an initial value of n = 1.0. Hence, two, four, and eight years corresponded to the first three decomposition levels for this study. Figure 2.1 (right) shows that after three decompositions, the time series associated with the third AC hardly showed any presence of periodic behavior. In other words, the resolution or the amount of certainty in the wavelet time-frequency spectrum diminished as the decomposition levels (DSs) went higher. Readers may also refer to Karthikeyan and Nagesh Kumar (2013) for more explanations regarding wavelet approximations and details.

Appendix 2.B

Table A2.B 1: Number of stations with significant positive (Pos.) and negative (Neg.) trends under the Mann-Kendall (MK) test in water-year and seasonal data along with their decompositions.

Time-series Data	Number of Stations with Significant Trends			
	Original Pos. (Neg.)	DS2 Pos. (Neg.)	DS4 Pos. (Neg.)	DS8 Pos. (Neg.)
Water year	46 (11)	69 (17)	93 (31)	93 (46)
Fall	67 (9)	97 (12)	126 (29)	134 (36)
Winter	52 (9)	62 (31)	87 (28)	83 (40)
Spring	28 (25)	40 (39)	55 (47)	66 (71)
Summer	39 (20)	62 (32)	76 (32)	82 (45)

Table A2.B 2: Number of stations with significant positive (Pos.) and negative (Neg.) shifts under the Pettitt's test in water year and seasonal data along with their decompositions.

Time-series Data	Number of Stations with Significant Shifts			
	Original Pos. (Neg.)	DS2 Pos. (Neg.)	DS4 Pos. (Neg.)	DS8 Pos. (Neg.)
Water year	77 (23)	93 (41)	136 (63)	150 (72)
Fall	105 (12)	120 (14)	151 (45)	174 (60)
Winter	68 (36)	76 (54)	110 (57)	126 (74)
Spring	36 (40)	49 (61)	77 (90)	100 (106)
Summer	55 (35)	73 (50)	112 (61)	147 (66)

Appendix 2.C

The spatial pattern of trends was more irregular with the seasons when compared to the water year trends. Nevertheless, seasons showed the presence of spatial coherence or region-specific trends (Figure A2.C1). In fall and its DSs, positive trends were mostly observed in the northeastern regions, whereas negative trends were prevalent in the northwestern regions (Figure A2.C1). Trends located on the extreme east and west regions, i.e., NE, MA, and PN, showed a higher rate of increase in the number of stations with trends compared to the central regions as the DSs went higher. Consequently, regions with field significance also increased as the DSs went higher. During winter and its DSs, besides the northwestern regions, negative trends were also observed in some of the mid-eastern regions, while positive trends mostly were located in the northeastern and central regions (Figure A2.C1). The increase in the number of stations with trends was observed to be higher in the western regions, i.e., PN and CA, compared to the eastern and central regions as the DSs went higher. At DS4 and DS8, all the regions showed field significance.

In spring and its DSs, stations with trends showed quite a different pattern when compared to the other seasons. Stations with negative trends were found in the eastern regions; such trends were almost absent during the other seasons (except for a few stations during winter) (Figure A2.C1). With the increase in DSs, NE, MA, SAG, PN, and CA showed a higher increase in negative trends compared to the other regions, while the central regions showed an increase in stations with positive trends. In summer and its DSs, stations with positive trends mostly were located in the northeastern and north-central regions, while negative trends were prevalent in the northwestern regions (Figure A2.C1). Eastern regions, e.g., NE, MA, and OH, showed the maximum increase in stations with positive trends, while the increase in negative trends was

found to be the highest in PN as the DSs went higher. In both spring and summer, with the increase in DSs, more regions showed field significance.

Stations with shifts during the seasons (Figure A2.C2) followed similar patterns as the trends during the seasons. In fall and its DSs, positive shifts were found in the northeastern regions, while negative shifts were located in the western regions (Figure A2.C2). The increase in stations with negative shifts was higher in the western regions, e.g., PN; while stations with positive shifts were observed to increase in the eastern regions, e.g., NE and MA. All the regions showed field significance in DS4 and DS8. In winter and its DSs, negative shifts were observed in the southeastern regions, which were not present in fall, while positive shifts were located in the northeastern and central regions (Figure A2.C2). The rate of increase in the number of stations with negative shifts was higher compared to the rate of increase in stations with positive shifts as the DSs went higher. The majority of the stations with negative shifts were located in SAG and PN, while stations with positive shifts were more spatially dispersed across the regions with a higher concentration in the eastern regions, i.e., NE and MA. Similar to fall, all the regions showed field significance in DS4 and DS8.
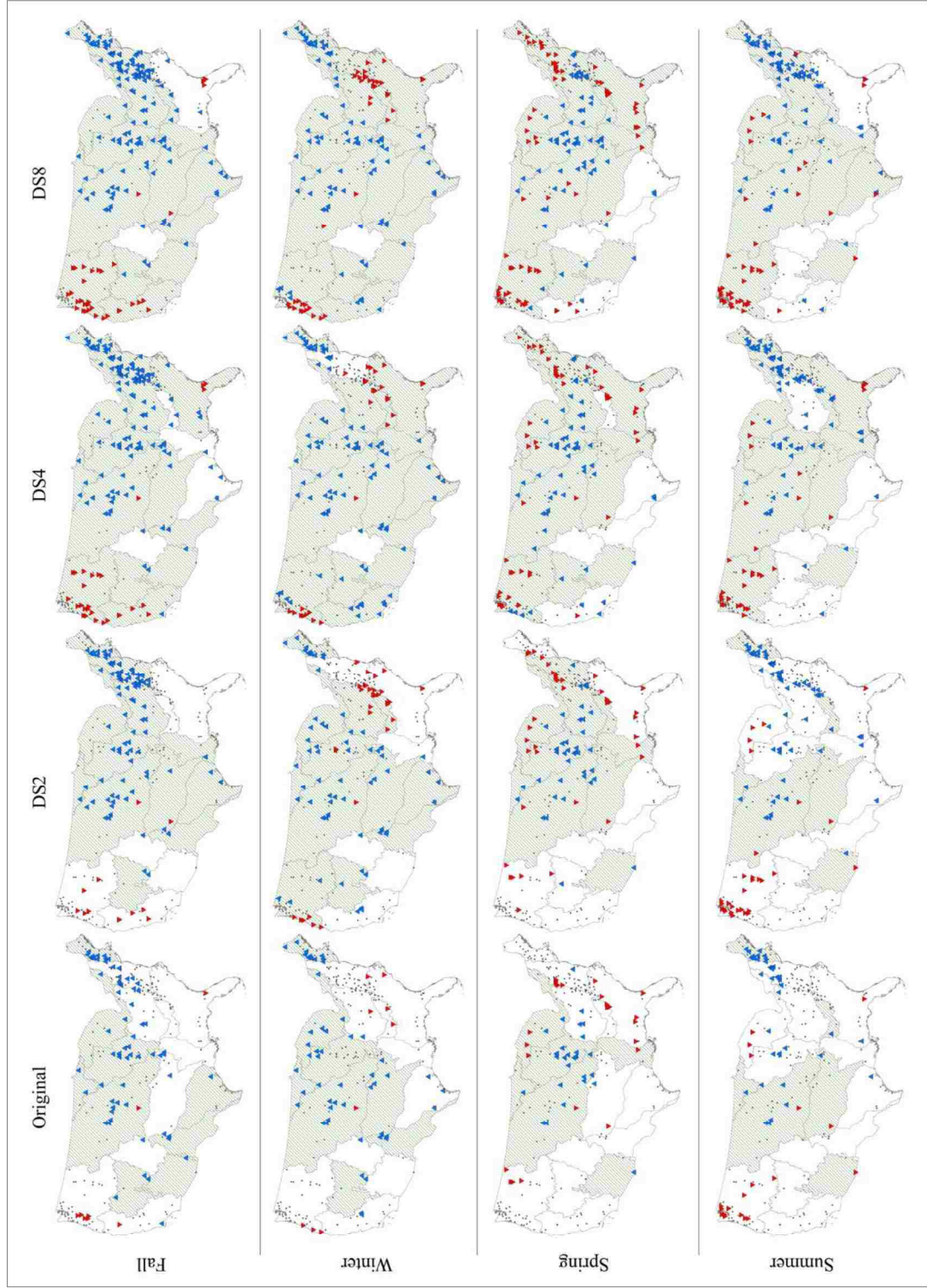
Figure A2.C 1: Location of stations with significant trends under the MK test for the seasonal data and their DSs. Upward (downward) pointing blue (red) triangles represent significant positive (negative) trends. Shaded regions represent field significance.

143

In spring and its DSs, negative shifts were observed in the eastern and northwestern regions, while positive shifts were found in the north-central regions (Figure A2.C2). The results show that similar to fall and winter, with the increase in DSs, stations with significant shifts also increased. A high concentration of stations with negative shifts was observed in NE, SAG, GL, and PN. MA, OH, and UMS showed a high concentration of stations with positive shifts. The number of regions with field significance was fewer compared to fall and winter in the lower DSs. However, all the regions showed field significance in DS8. In summer and its DSs, positive shifts were observed in the northeastern regions, while negative shifts were predominant in the northwestern regions (Figure A2.C2). The number of stations with negative shifts showed a much higher increase in PN, while positive shifts increased in NE and MA as the DSs increased. Similar to spring, all the regions were found to be field significant in DS8.
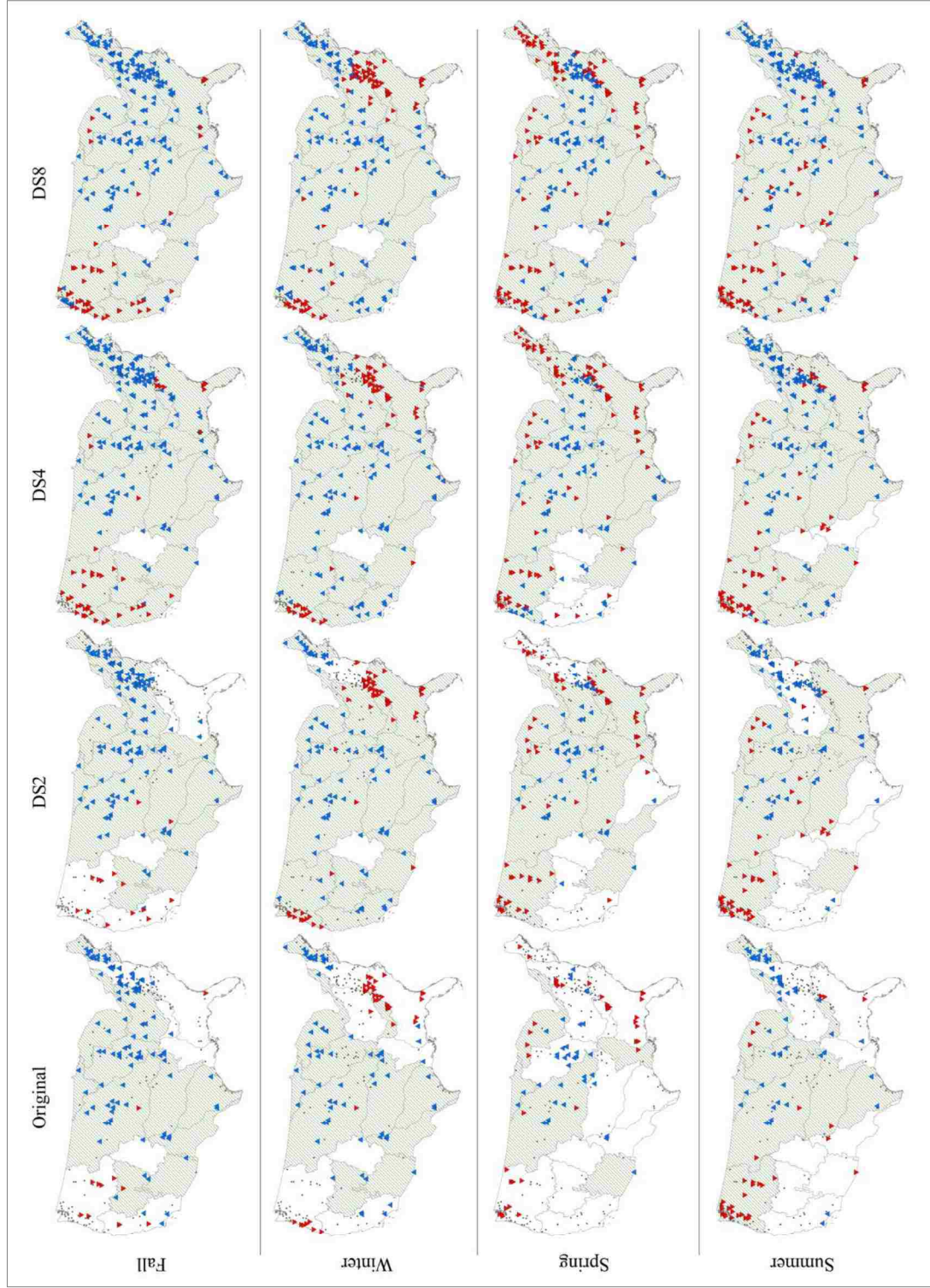
Figure A2.C 2: Location of the stations with significant shifts under the Pettitt's test for the seasonal data and their DSs. Upward (downward) pointing blue (red) triangles represent significant positive (negative) trends. Shaded regions represent field significance.

Appendix 2.D

The number of stations with significant shifts during the study period in water year and its DSs is shown in Figure A2.D1. A higher number of stations with shifts were found from the 1960s to 1980s in all the time series. The results showed that the location in time and direction of the shifts varied across the DSs. DS2 and DS4 showed similarity in their shifts distributions, while DS8 showed an oscillatory alternating reverse pattern – a series of years with positive shifts followed by a series of years with negative shifts. Moreover, in DS2 and DS4, there were instances where both directional shifts occurred in the same year, which was rarely observed in the original water year and DS8.

As seen in Figure A2.D1, the occurrence of shifts showed an oscillating tendency in the higher SBs, especially in DS8. As a result, the shift years were compared against the years associated with the coupled phases of the climate signals, i.e., ENSO, PDO, and AMO, to detect their concurrency during the study period, since climate signals also show oscillating trends. Both the ENSO (El Niño and La Niña) phases were compared against the PDO (warm or cold) and AMO (positive or negative) phases to observe their coupled effects on the regional streamflow. The majority of the stations with shifts that coincided with the PDO cold years were found to shift during the La Niña years (Figure A2.D2). Both positive and negative shifts were found during the La Niña years, while only positive shifts were found during the El Niño years. During the PDO warm years, both positive and negative shifts were observed during the El Niño and La Niña years, though the number of stations with significant shifts was much less when compared to the PDO cold years. The remaining stations with shifts were spread out across the study area without any visible spatial pattern.
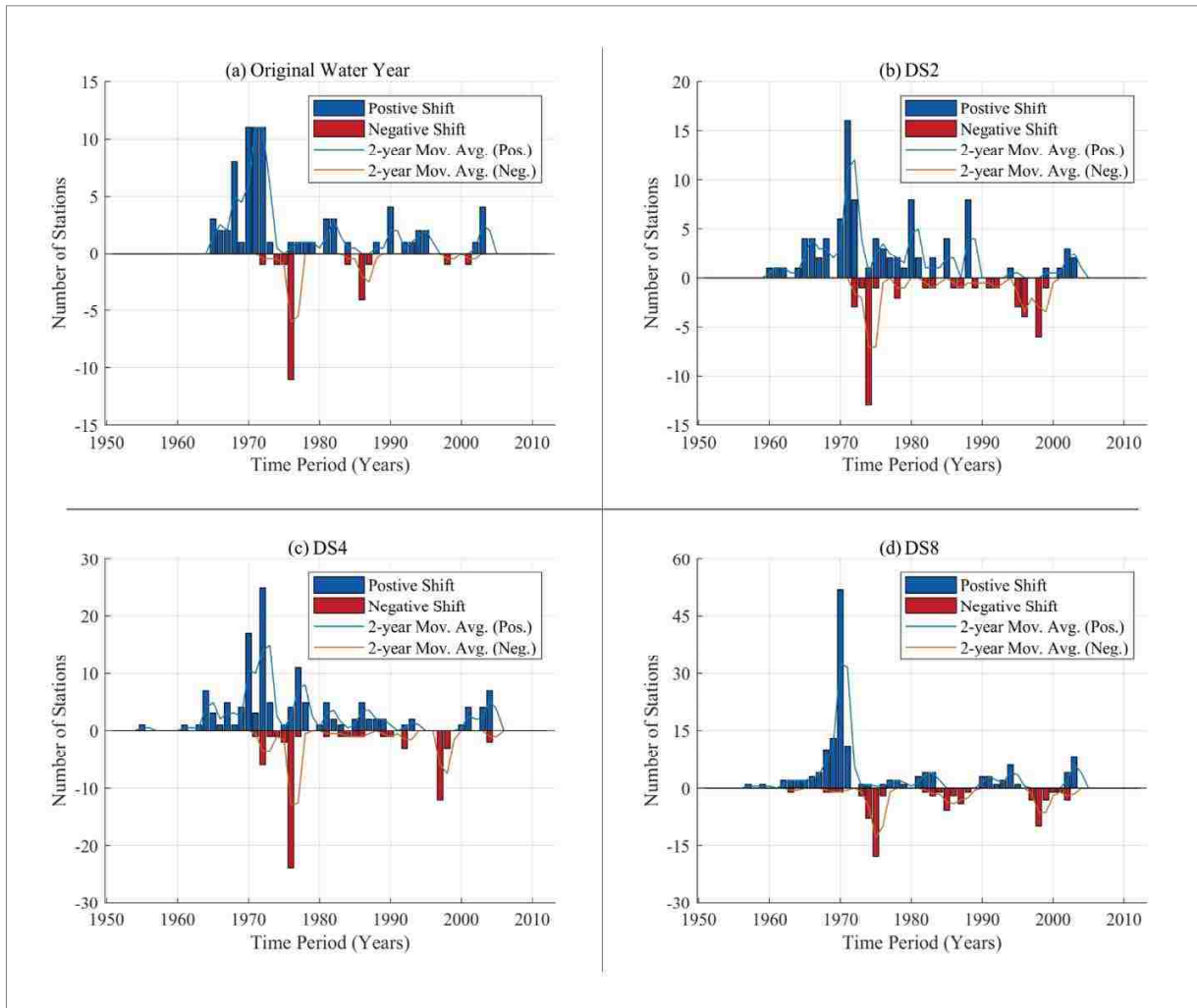
Figure A2.D 1: Number of stations with significant shifts in water year and its DSs. Blue (red) bars indicate positive (negative) shifts. Blue (red) lines represent the 2-year-moving-average trend lines for positive (negative) shifts.

During the AMO positive (warm) years, positive shifts were more prevalent compared to negative shifts (Figure A2.D2). Also, the majority of the stations during the AMO warm years coincided with the El Niño years across the continental US, while only one station coincided with a La Niña year. A few stations were found not to coincide neither with the El Niño nor the La Niña years, but no pattern was observed among them. During the AMO negative (cold) years,

both positive and negative shifts were observed across the US, with the majority of the stations coinciding with the La Niña years. Similar to the AMO warm years, a few stations were found to coincide neither with the El Niño nor the La Niña years. The comparison of PDO and AMO phases showed similar locations of stations with shifts – the similarity was found to be higher during their cold phases.

Figure A2.D2 shows that NE, MA, GL, OH, UMS, SRR, MO, and PN had a significant number of stations with shifts at one or more of the coupled phases of the climate signals, i.e., El Niño/La Niña phase during PDO warm/cold years, and/or El Niño/La Niña phase during AMO positive/negative years. All these regions also showed field significance during the DSs of the water year (Figure 2.2). The concept of CWT was applied to evaluate the variance of these regions' streamflow and the climate signals across multiple CSs. The first principal component (PC1), obtained from the principal component analysis (PCA) of all the stations in a region, was used to represent the regional streamflow time series. Table A2.D1 lists the percentage of variability explained by the PC1 from the PCA analysis for each region. The CWTs explained how these individual time series have varied over time across the CSs (Figures A2.D3 and A2.D4), where the higher power in the wavelet power spectrum represents higher variability.
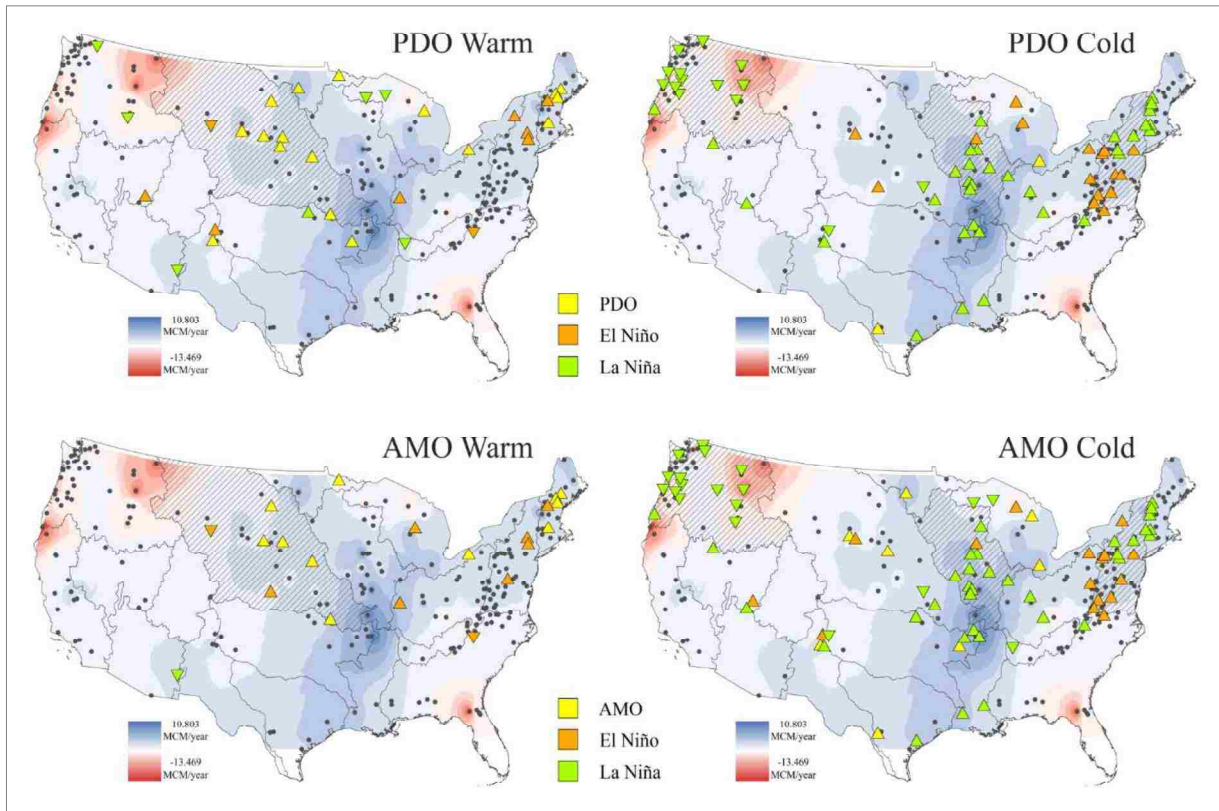
Figure A2.D 2: (**1ˢᵗ row**) Location of stations with significant shifts coinciding with the PDO warm (**left**) and cold (**right**) years, in conjunction with the ENSO (El Niño or La Niña) years. (**2ⁿᵈ row**) Location of stations with significant shifts coinciding with the AMO warm (**left**) and cold (**right**) years, in conjunction with the ENSO (El Niño or La Niña) years. Upward (downward) pointing triangles indicate positive (negative) shifts. The blue and red shades indicate the increasing and decreasing slope of trends, respectively.

Table A2.D 1: Percentage of variance explained by the first principal component (PC1) obtained from the principal component analysis (PCA) of the selected regions.

Hydrologic Region Name	Number of Stations	Variance of data Explained by the PC1
New England (NE)	18	87.62%
Mid-Atlantic (MA)	39	71.29%
Great Lakes (GL)	10	67.03%
Ohio (OH)	20	64.96%
Upper Mississippi (UMS)	19	67.05%
Souris-Red-Rainy (SRR)	3	86.79%
Missouri (MO)	21	66.41%
Pacific Northwest (PN)	37	80.22%

The CWTs of the climate signals revealed that each of them experienced higher variance at different CSs during various time intervals. The highest significant variance for ENSO was observed in CS4 to CS8 between 1980 and 1990 (Figure A2.D3). For PDO, the highest significant variance was observed in CS8 to CS12 from 1995 to 2005. For AMO, there was a higher variance after CS16 but it was not found to be statistically significant. The highest significant variance for AMO was found below CS4. The global wavelet spectra for each of the climate signals also showed similar higher power as was observed in their wavelet power spectra. The three-to-six-year-scale-average for each of the climate signals showed their periodic nature over the study period (Figure A2.D3).
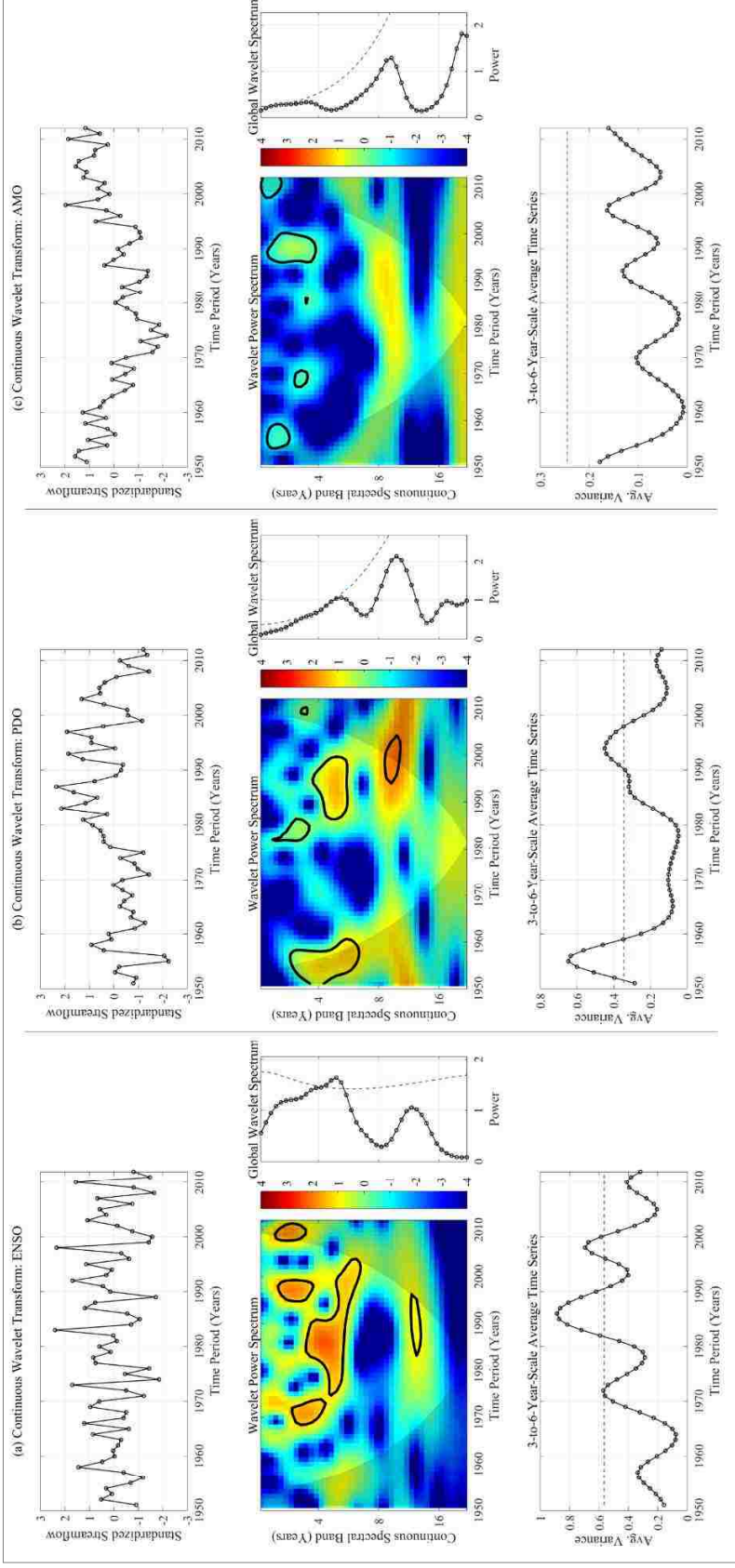
Figure A2.D 3: Standardized time series, continuous wavelet power spectrum, global wavelet spectrum, and three-to-six-year-scale average time-series of (**a**) ENSO, (**b**) PDO, and (**c**) AMO. Red (blue) represents stronger (weaker) power or variance. 5% significance zones against the red noise are delineated by the thick black contour lines.

151

The results showed that ENSO had a much better-defined periodicity, which was less than a decade, compared to PDO and AMO. For PDO, there was no definite periodicity during the study period. Though AMO showed cyclic behavior, the periodicity varied from a decade to more than a decade over the study period.

The CWTs of the regional streamflow showed significant variation among them (Figure A2.D4). There was a definite presence of higher variance after 1970 for the majority of the regions, though the ranges of CSs varied. From the global wavelet spectra, it was observed that the majority of the regions experienced higher variance in CS8 to CS16. Higher variance beyond CS16 was also observed for certain regions. All the regions, except for MO, had more than one significant zone of noticeable duration (Figure A2.D4).
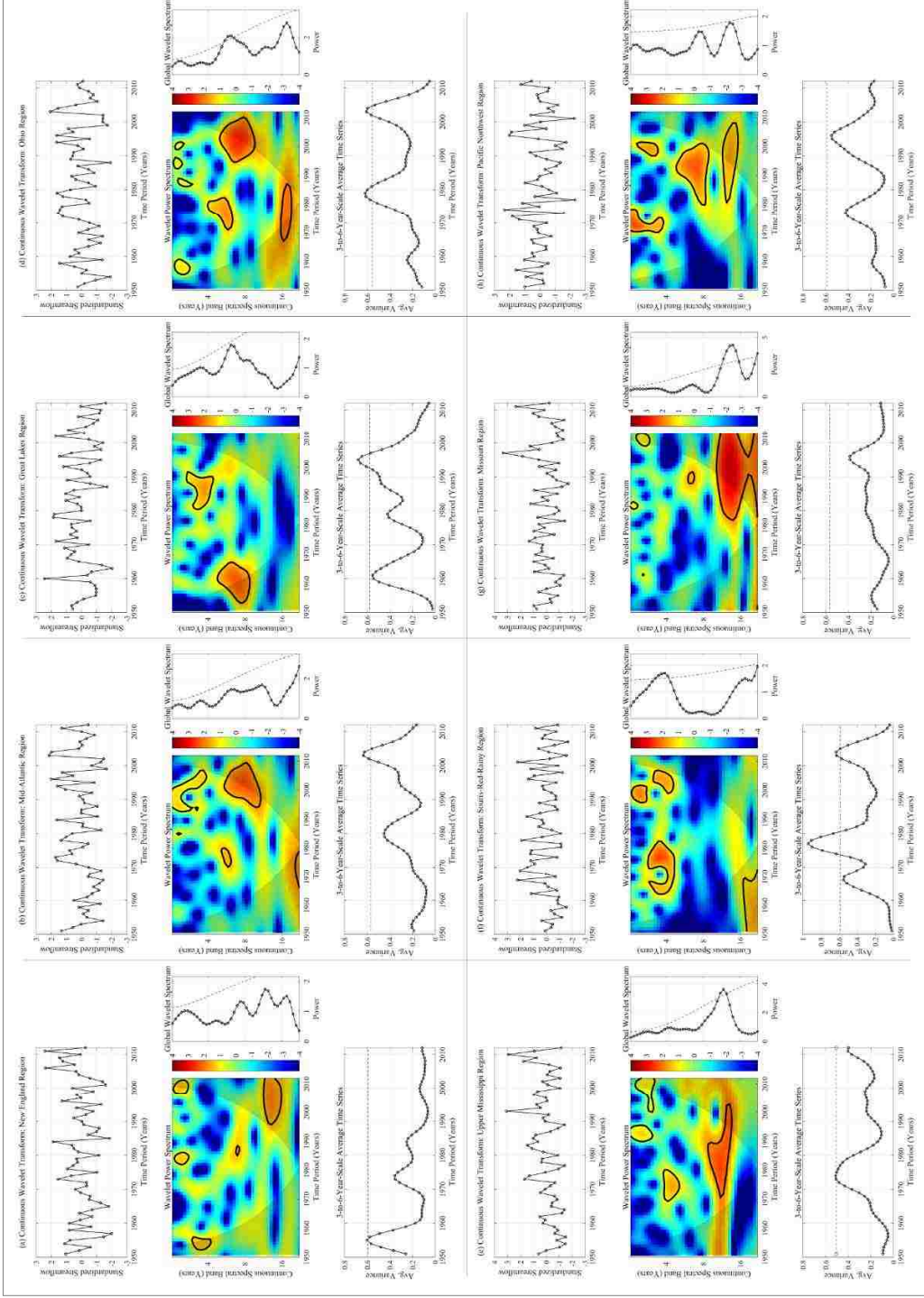
Figure A2.D 4: Standardized time series, continuous wavelet power spectrum, global wavelet spectrum, and three-to-six-year-scale average time-series (**1ˢᵗ three rows**, left to right) New England (NE), Mid-Atlantic (MA), Great Lakes (GL), Ohio (OH), (**2ⁿᵈ three rows**, left to right) Upper Mississippi (UMS), Souris-Red-Rainy (SRR), Missouri (MO), and Pacific Northwest (PN). Red (blue) represents stronger (weaker) power or variance. 5% significance zones against the red noise are delineated by the thick black contour lines.

153

Appendix 2.E
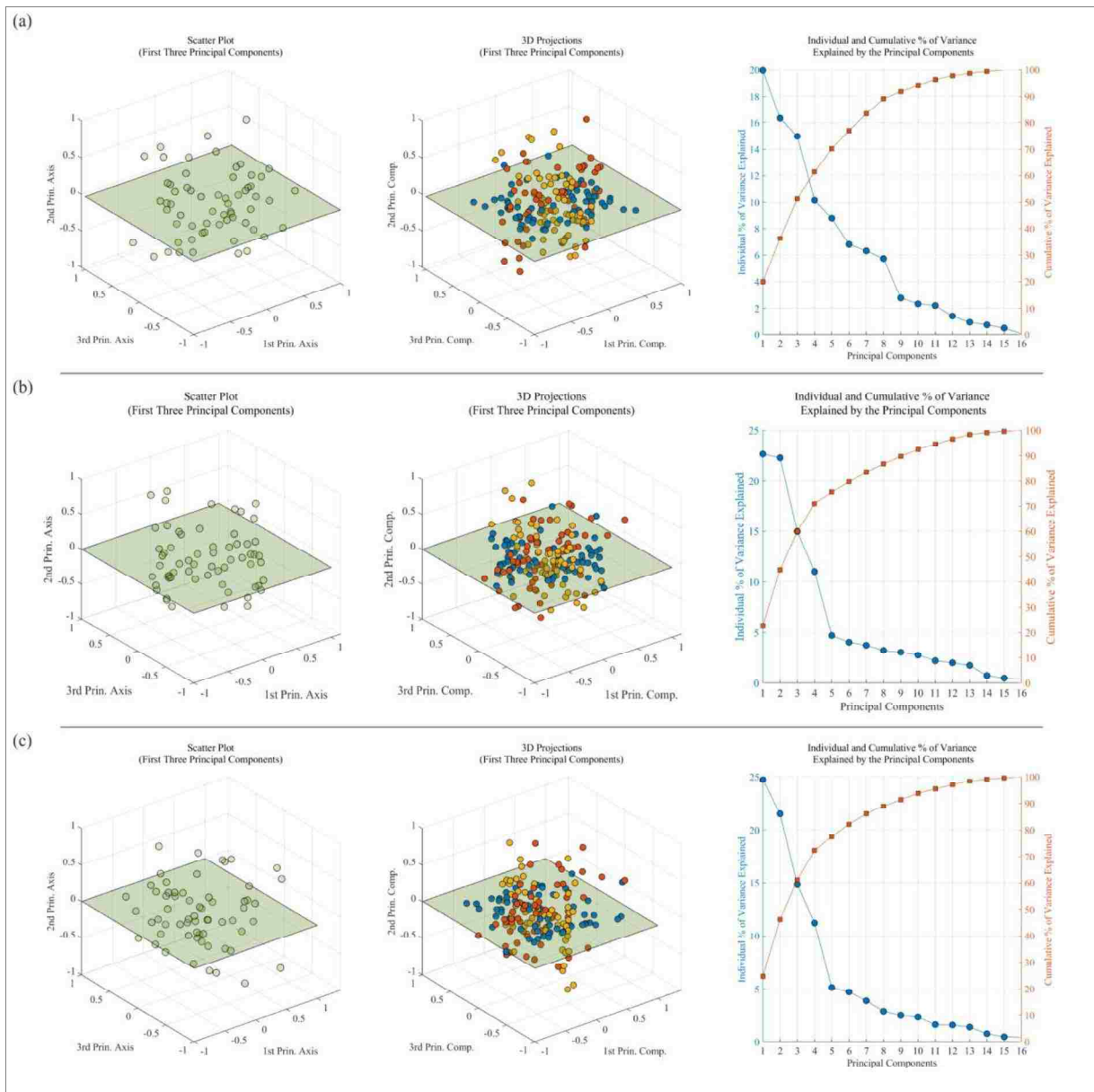
Figure A2.E 1: Principal component analyses (PCA) of the (**a**) Mid-Atlantic (MA), (**b**) Missouri (MO), and (**c**) Pacific Northwest (PN) region. **(Left)** The 3D plots show the first three principal components and their projections. **(Right)** Plots showing percentage of individual and cumulative variance explained by the principal components. For MA, MO, and PN, the number of principal components explaining more than 95% of the variability was 11, 12, and 11, respectively, out of the total 16 possible inputs.
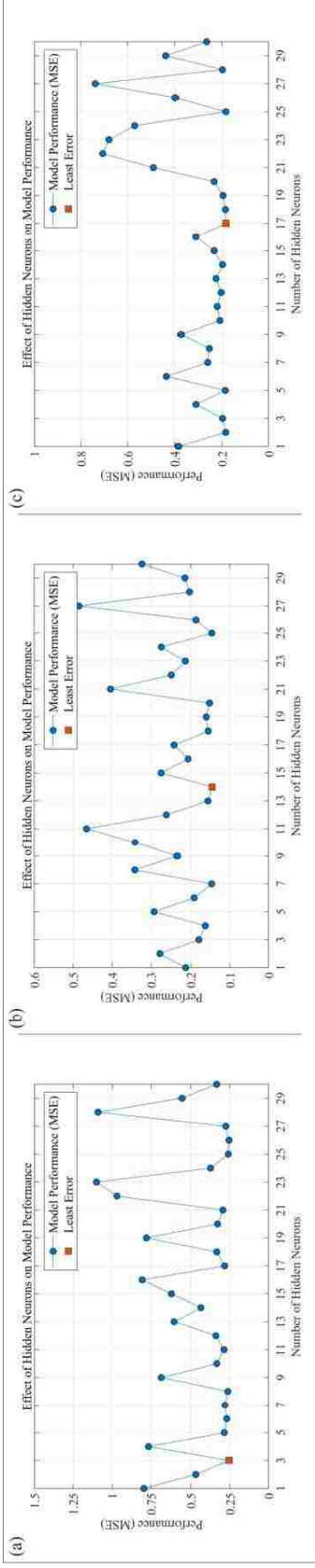
Figure A2.E 2: Effect of hidden neurons on the model performance for the (**a**) Mid-Atlantic (MA), (**b**) Missouri (MO), and (**c**) Pacific Northwest (PN) region. The appropriate number of hidden neurons chosen for MA, MO, and PN was three, seven, and two, respectively.
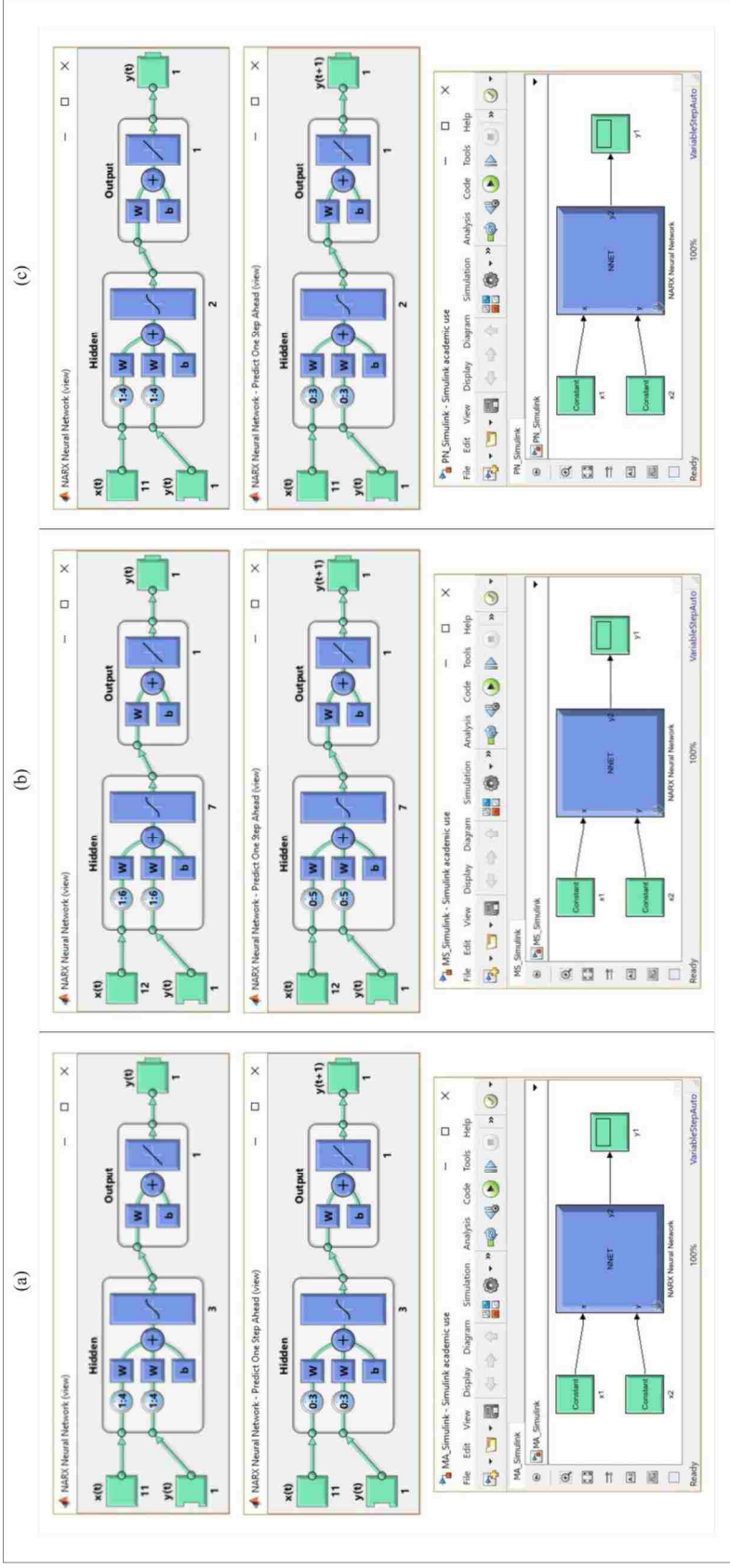
Figure A2.E 3: Screen dump of the optimized NARX model from MATLAB 2018a for the (**a**) Mid-Atlantic (MA), (**b**) Missouri, and (**c**) Pacific Northwest region. Rows 1 through 3 show the fitted model, fitted model with one step ahead prediction, and the Simulink model, respectively.
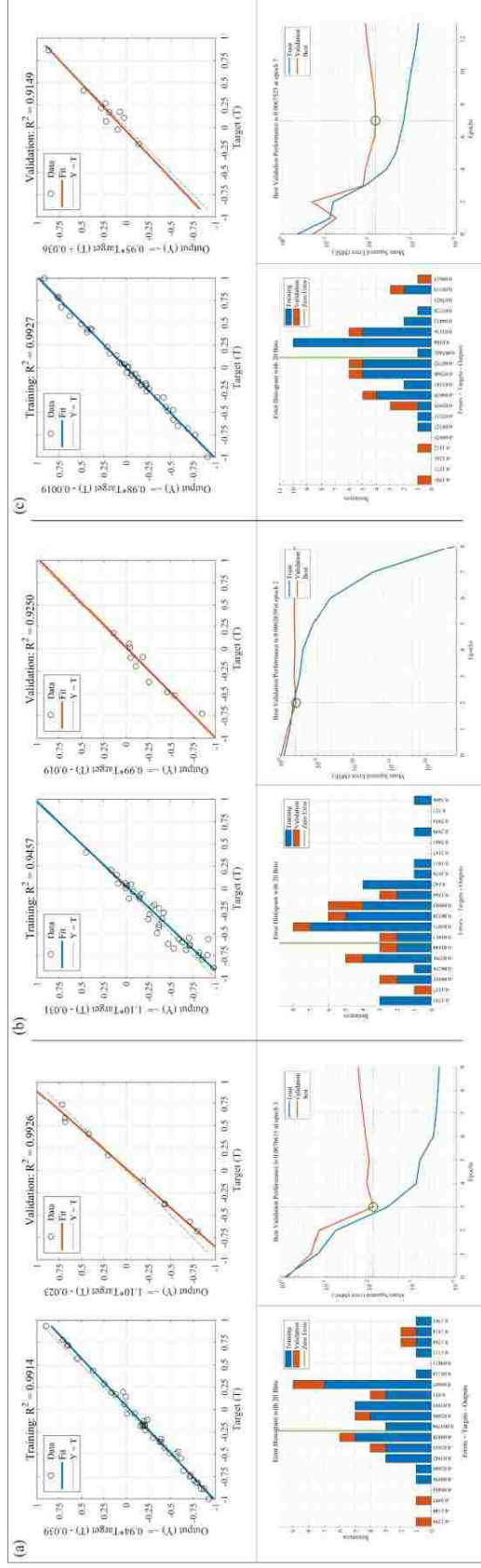
Figure A2.E 4: (**1st row**) Model fitting, (**2nd row**) error histogram, and the best validation performance of the WANN model (training and validation) for the (**a**) Mid-Atlantic (MA), (**b**) Missouri (MO), and (**c**) Pacific Northwest region. 20% of the data were randomly selected for validation.

157
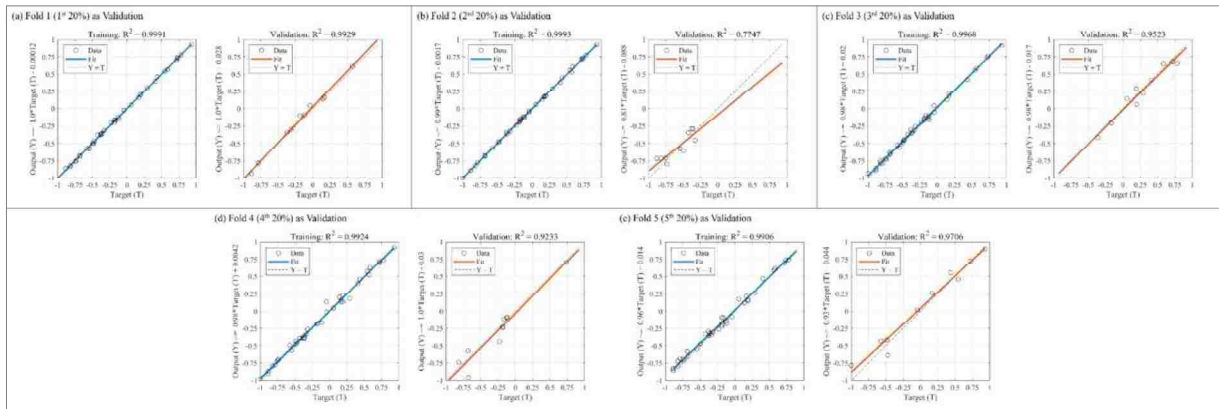
Figure A2.E 5: Model fitting (training and validation) of the K-fold cross-validation (5 folds as shown in a through e) for the Mid-Atlantic (MA) region.
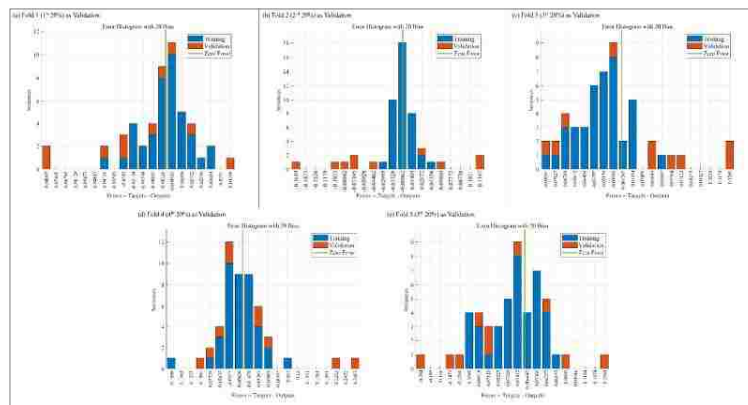
Figure A2.E 6: Error histogram (training and validation) of the K-fold cross-validation (5 folds as shown in a through e) for the Mid-Atlantic (MA) region.
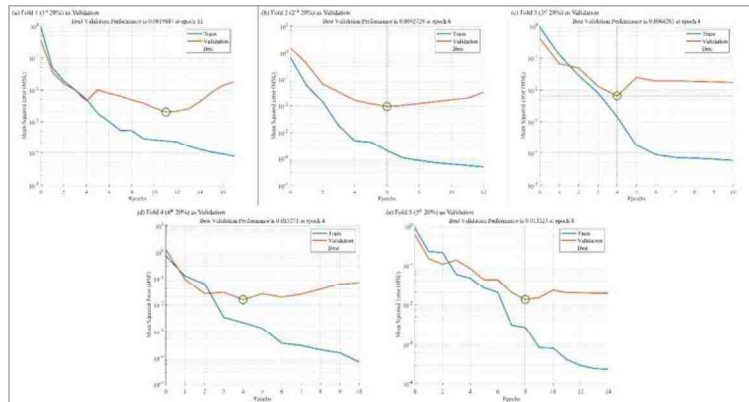
Figure A2.E 7: Best validation performance (training and validation) of the K-fold cross-validation (5 folds as shown in a through e) for the Mid-Atlantic (MA) region.
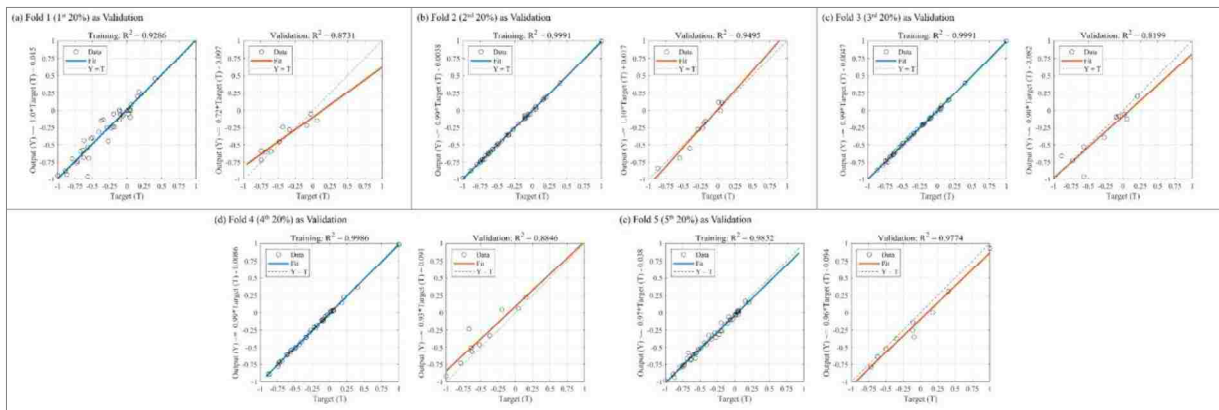
Figure A2.E 8: Model fitting (training and validation) of the K-fold cross-validation (5 folds as shown in a through e) for the Missouri (MO) region.
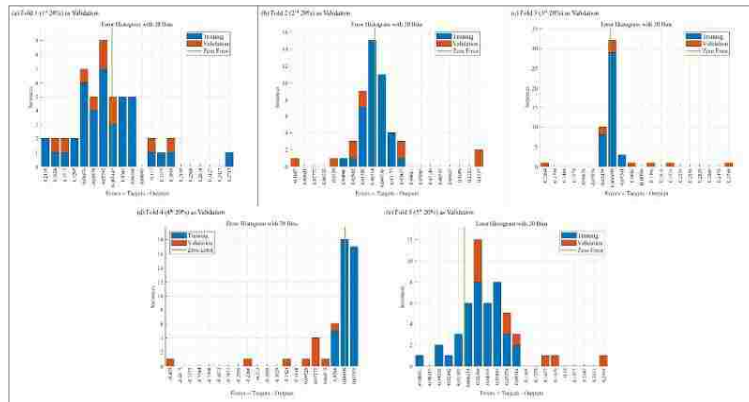
Figure A2.E 9: Error histogram (training and validation) of the K-fold cross-validation (5 folds as shown in a through e) for the Missouri (MO) region.
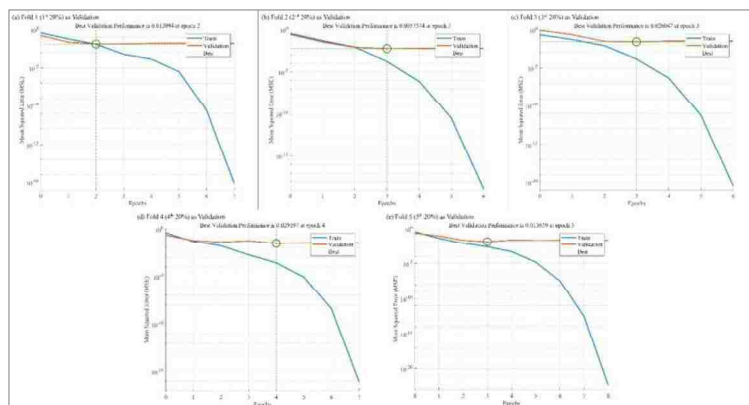
Figure A2.E 10: Best validation performance (training and validation) of the K-fold cross-validation (5 folds as shown in a through e) for the Missouri (MO) region.
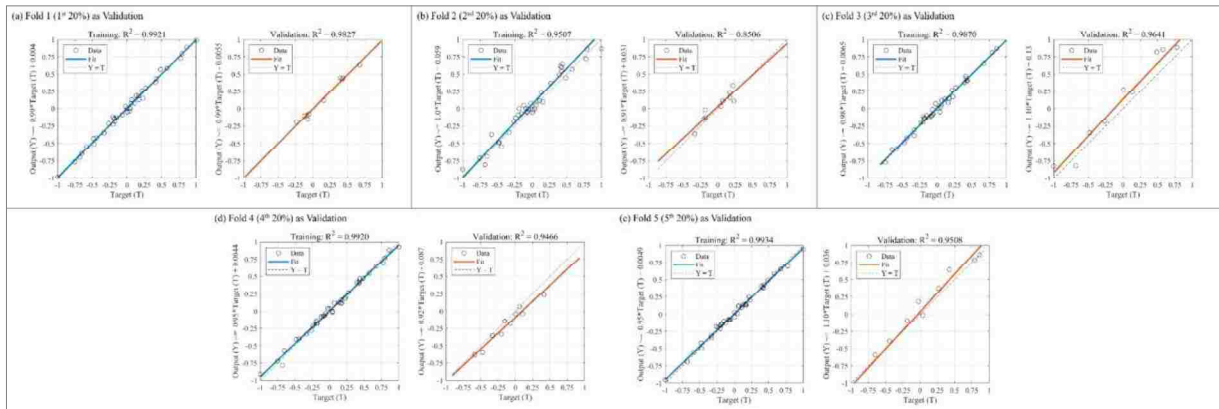
Figure A2.E 11: Model fitting (training and validation) of the K-fold cross-validation (5 folds as shown in a through e) for the Pacific Northwest (PN) region.
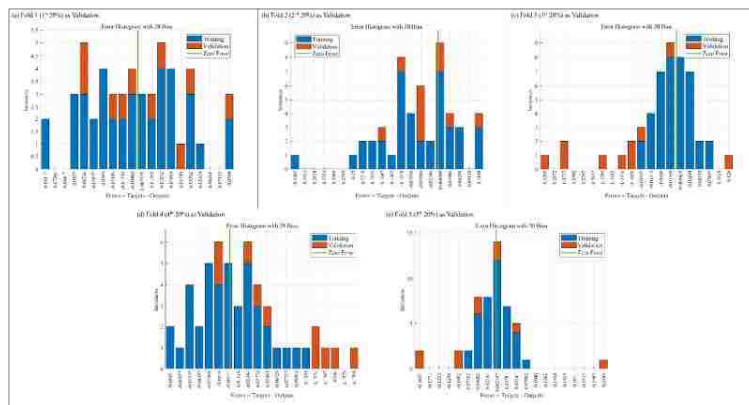
Figure A2.E 12: Error histogram (training and validation) of the K-fold cross-validation (5 folds as shown in a through e) for the Pacific Northwest (PN) region.

161
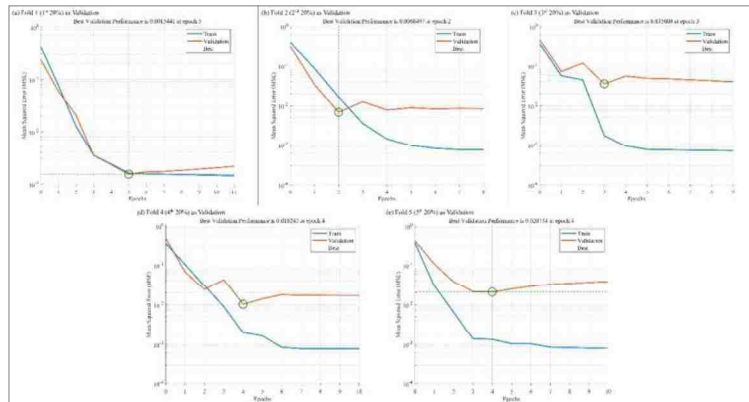
Figure A2.E 13: Best validation performance (training and validation) of the K-fold cross-validation (5 folds as shown in a through e) for the Pacific Northwest (PN) region.

Table A2.E 1: Comparison among various support vector machine (SVM) and Gaussian process regression (GPR) models during the training and validation phase (aggregated result of the K-fold cross-validation with 5 folds) for the Mid-Atlantic (MA) region.

Group		Models	Brief Description of the Models	RMSE	R^2	MSE	MAE
1.0		Support Vector Machines (SVM)					
	1.1	Linear SVM	A SVM that follows simple linear structure in the data, using the linear kernel	0.1268	0.9400	0.0160	0.0947
	1.2	Quadratic SVM	A SVM that uses the quadratic kernel	0.1208	0.9500	0.0145	0.0860
	1.3	Cubic SVM	A SVM that uses the cubic kernel	0.1323	0.9400	0.0175	0.0971
2.0		Gaussian Process Regression Models					
	4.1	Squared Exponential	A Gaussian process model that uses the squared exponential kernel	0.0699	0.9800	0.0048	0.0503
	4.2	Matern 5/2	A Gaussian process model that uses the Matern 5/2 kernel	0.0695	0.9800	0.0048	0.0497
	4.3	Exponential	A Gaussian process model that uses the exponential kernel	0.1797	0.8800	0.0323	0.1312
	4.4	Rational Quadratic	A Gaussian process model that uses the rational quadratic kernel	0.0699	0.9800	0.0048	0.0503

Table A2.E 2: Comparison among various support vector machine (SVM) and Gaussian process regression (GPR) models during the training and validation phase (aggregated result of the K-fold cross-validation with 5 folds) for the Missouri (MO) region.

Group		Models	Brief Description of the Models	RMSE	R^2	MSE	MAE
1.0		Support Vector Machines (SVM)					
	1.1	Linear SVM	A SVM that follows simple linear structure in the data, using the linear kernel	0.0967	0.9400	0.0093	0.0722
	1.2	Quadratic SVM	A SVM that uses the quadratic kernel	0.0909	0.9600	0.0065	0.0605
	1.3	Cubic SVM	A SVM that uses the cubic kernel	0.0977	0.9400	0.0095	0.0722
2.0		Gaussian Process Regression Models					
	2.1	Squared Exponential	A Gaussian process model that uses the squared exponential kernel	0.0280	0.9900	0.0007	0.0225
	2.2	Matern 5/2	A Gaussian process model that uses the Matern 5/2 kernel	0.0279	0.9900	0.0007	0.0224
	2.3	Exponential	A Gaussian process model that uses the exponential kernel	0.1460	0.8600	0.0213	0.1034
	2.4	Rational Quadratic	A Gaussian process model that uses the rational quadratic kernel	0.0280	0.9900	0.0007	0.0225

Table A2.E 3: Comparison among various support vector machine (SVM) and Gaussian process regression (GPR) models during the training and validation phase (aggregated result of the K-fold cross-validation with 5 folds) for the Pacific Northwest (PN) region.

Group	Models		Brief Description of the Models	RMSE	R^2	MSE	MAE
1.0	Support Vector Machines (SVM)						
	1.1	Linear SVM	A SVM that follows simple linear structure in the data, using the linear kernel	0.1295	0.9100	0.0167	0.0933
	1.2	Quadratic SVM	A SVM that uses the quadratic kernel	0.0995	0.9500	0.0099	0.0738
	1.3	Cubic SVM	A SVM that uses the cubic kernel	0.1061	0.9400	0.0112	0.0828
2.0	Gaussian Process Regression Models						
	2.1	Squared Exponential	A Gaussian process model that uses the squared exponential kernel	0.0681	0.9800	0.0046	0.0548
	2.2	Matern 5/2	A Gaussian process model that uses the Matern 5/2 kernel	0.0680	0.9800	0.0046	0.0545
	2.3	Exponential	A Gaussian process model that uses the exponential kernel	0.1554	0.8700	0.0241	0.1130
	2.4	Rational Quadratic	A Gaussian process model that uses the rational quadratic kernel	0.0681	0.9800	0.0046	0.0548

Table A2.E 4: Comparison of various learning algorithms during the testing phase (unseen data) for the Mid-Atlantic (MA) region.

Group		Training Function - Learning Algorithm	R^2	RMSE
1.0		Backpropagation training function with Jacobian derivative		
	1.1	trainbr - Bayesian Regularization backpropagation	0.9786	0.0864
	1.2	trainlm - Levenberg-Marquardt backpropagation	0.9565	0.1231
2.0		Backpropagation training function with gradient derivative		
	2.1	trainbfg - BFGS quasi-Newton backpropagation	0.9565	0.1231
	2.2	traincgb - Conjugate gradient backpropagation with Powell-Beale restarts	0.9645	0.1112
	2.3	traincgf - Conjugate gradient backpropagation with Fletcher-Reeves updates	0.9662	0.1085
	2.4	traincgp - Conjugate gradient backpropagation with Polak-Ribiere updates	0.9643	0.1115
	2.5	traingd - Gradient descent backpropagation	0.5940	0.3761
	2.6	traingda - Gradient descent with adaptive lr backpropagation	0.9306	0.1555
	2.7	traingdm - Gradient descent with momentum	_	_
	2.8	traingdx - Gradient descent w/momentum & adaptive lr backpropagation	_	_
	2.9	trainoss - One step secant backpropagation	0.9741	0.0950
	2.10	trainrp - RPROP backpropagation	0.7169	0.3140
	2.11	trainscg - Scaled conjugate gradient backpropagation	0.9588	0.1198
3.0		Supervise weight/bias training functions		
	3.1	trainb - Batch training with weight & bias learning rules	_	_
	3.2	trainc - Cyclical order weight/bias training	0.9646	0.1111
	3.3	trainr - Random order weight/bias training	0.8952	0.1911
	3.4	trains - Sequential order weight/bias training	0.8451	0.2323

Table A2.E 5: Comparison of various learning algorithms during the testing phase (unseen data) for the Missouri (MO) region.

Group	Training Function - Learning Algorithm		R^2	RMSE
1.0	Backpropagation training function with Jacobian derivative			
	1.1	trainbr - Bayesian Regularization backpropagation	0.9891	0.0441
	1.2	trainlm - Levenberg-Marquardt backpropagation	0.8986	0.1344
2.0	Backpropagation training function with gradient derivative			
	2.1	trainbfg - BFGS quasi-Newton backpropagation	0.8854	0.1429
	2.2	traincgb - Conjugate gradient backpropagation with Powell-Beale restarts	0.8849	0.1432
	2.3	traincgf - Conjugate gradient backpropagation with Fletcher-Reeves updates	0.8883	0.1411
	2.4	traincgp - Conjugate gradient backpropagation with Polak-Ribiere updates	0.8670	0.1539
	2.5	traingd - Gradient descent backpropagation	0.7016	0.2306
	2.6	traingda - Gradient descent with adaptive lr backpropagation	0.8219	0.1781
	2.7	traingdm - Gradient descent with momentum	0.7034	0.2299
	2.8	traingdx - Gradient descent w/momentum & adaptive lr backpropagation	0.8652	0.1550
	2.9	trainoss - One step secant backpropagation	0.8869	0.1419
	2.10	trainrp - RPROP backpropagation	0.8272	0.1755
	2.11	trainscg - Scaled conjugate gradient backpropagation	0.8892	0.1405
3.0	Supervise weight/bias training functions			
	3.1	trainb - Batch training with weight & bias learning rules	0.7034	0.2299
	3.2	trainc - Cyclical order weight/bias training	0.8756	0.1489
	3.3	trainr - Random order weight/bias training	0.6622	0.2453
	3.4	trains - Sequential order weight/bias training	0.7234	0.2220

Table A2.E 6: Comparison of various learning algorithms during the testing phase (unseen data) for the Pacific Northwest (PN) region.

Group		Training Function - Learning Algorithm	R^2	RMSE
1.0		Backpropagation training function with Jacobian derivative		
	1.1	trainbr - Bayesian Regularization backpropagation	0.8960	0.1242
	1.2	trainlm - Levenberg-Marquardt backpropagation	0.8518	0.1483
2.0		Backpropagation training function with gradient derivative		
	2.1	trainbfg - BFGS quasi-Newton backpropagation	0.8670	0.1405
	2.2	traincgb - Conjugate gradient backpropagation with Powell-Beale restarts	0.8853	0.1305
	2.3	traincgf - Conjugate gradient backpropagation with Fletcher-Reeves updates	0.8311	0.1583
	2.4	traincgp - Conjugate gradient backpropagation with Polak-Ribiere updates	0.9039	0.1194
	2.5	traingd - Gradient descent backpropagation	_	_
	2.6	traingda - Gradient descent with adaptive lr backpropagation	_	_
	2.7	traingdm - Gradient descent with momentum	_	_
	2.8	traingdx - Gradient descent w/momentum & adaptive lr backpropagation	_	_
	2.9	trainoss - One step secant backpropagation	_	_
	2.10	trainrp - RPROP backpropagation	0.8175	0.1646
	2.11	trainscg - Scaled conjugate gradient backpropagation	0.6274	0.2351
3.0		Supervise weight/bias training functions		
	3.1	trainb - Batch training with weight & bias learning rules	_	_
	3.2	trainc - Cyclical order weight/bias training	0.9052	0.1186
	3.3	trainr - Random order weight/bias training	_	_
	3.4	trains - Sequential order weight/bias training	_	_

Appendix 3

Chapter 3 has no additional/supplementary material.

Appendix 4

Table A4. 1: Names and numbers of the individual districts in each of the states. The states are color coded based on Figure 4.1.

No.	Name	No.	Name	No.	Name	No.	Name	No.	Name
1	Chandigarh	33	Anantanag	64	Agra	96	Hardoi	134	Almora
2	New Delhi	34	Badgam	65	Aligarh	97	Hathras	135	Bageshwar
3	Ambala	35	Baramula	66	Allahabad	98	Jalaun	136	Chamoli
4	Bhiwani	36	Doda	67	Ambedkar Nagar	99	Jaunpur	137	Champawat
5	Faridabad	37	Jammu	68	Auraiya	100	Jhansi	138	Dehradun
6	Fatehabad	38	Kargil	69	Azamgarh	101	Jyotiba Phule Nagar	139	Garhwal
7	Gurgaon	39	Kathua	70	Baghpat	102	Kannauj	140	Hardwar
8	Hisar	40	Kupwara	71	Bahraich	103	Kanpur Dehat	141	Nainital
9	Jhajjar	41	Leh (Ladakh)	72	Ballia	104	Kanpur Nagar	142	Pithoragarh
10	Jind	42	Pulwama	73	Balrampur	105	Kaushambi	143	Rudraprayag
11	Kaithal	43	Punch	74	Banda	106	Kheri	144	Tehri Garhwal
12	Karnal	44	Rajauri	75	Barabanki	107	Kushinagar	145	Udham Singh Nagar
13	Kurukshetra	45	Srinagar	76	Bareilly	108	Lalitpur	146	Uttarkashi
14	Mahendragarh	46	Udhampur	77	Basti	109	Lucknow		
15	Panchkula	47	Amritsar	78	Bijnor	110	Maharajganj		
16	Panipat	48	Bathinda	79	Budaun	111	Mahoba		
17	Rewari	49	Faridkot	80	Bulandshahar	112	Mainpuri		
18	Rohtak	50	Fatehgarh Sahib	81	Chandauli	113	Mathura		
19	Sirsa	51	Firozpur	82	Chitrakoot	114	Mau		
20	Sonipat	52	Gurdaspur	83	Deoria	115	Meerut		
21	Yamunanagar	53	Hoshiarpur	84	Etah	116	Mirzapur		
22	Chamba	54	Jalandhar	85	Etawah	117	Moradabad		
23	Hamirpur	55	Kapurthala	86	Faizabad	118	Muzaffarnagar		
24	Kangra	56	Ludhiana	87	Farrukhabad	119	Pilibhit		
25	Kinnaur	57	Mansa	88	Fatehpur	120	Pratapgarh		
26	Kullu	58	Moga	89	Firozabad	121	Rae Bareli		
27	Lahul & Spiti	59	Muktsar	90	Gautam Buddha Nagar	122	Rampur		
28	Mandi	60	Nawanshahr	91	Ghaziabad	123	Saharanpur		
29	Shimla	61	Patiala	92	Ghazipur	124	Sant Kabir Nagar		
30	Sirmaur	62	Rupnagar	93	Gonda	125	Sant Ravidas Nagar		
31	Solan	63	Sangrur	94	Gorakhpur	126	Shahjahanpur		
32	Una			95	Hamirpur	127	Shrawasti		
						128	Siddharthnagar		
						129	Sitapur		
						130	Sonbhadra		
						131	Sultanpur		
						132	Unnao		
						133	Varanasi		

Appendix 5

Table A5. 1: List of CMIP5 temperature and precipitation models used in the study.

	CMIP5 Temperature Models
1	ACCESS1-0
2	bcc-csm1-1
3	CanESM2
4	CCSM4
5	CESM1-CAM5
6	CNRM-CM5
7	CSIRO-Mk3-6-0
8	GFDL-CM3
9	GFDL-ESM2G
10	GFDL-ESM2M
11	GISS-E2-H
12	GISS-E2-R
13	HadCM3
14	HadGEM2-CC
15	HadGEM2-ES
16	inmcm4
17	IPSL-CM5A-LR
18	IPSL-CM5A-MR
19	MIROC5
20	MIROC-ESM
21	MPI-ESM-LR
22	MRI-CGCM3
23	NorESM1-M
24	ACCESS1-3
25	CESM1-BGC
26	CESM1-FASTCHEM
27	CESM1-WACCM
28	CMCC-CESM
29	CMCC-CM
30	CMCC-CMS
31	CNRM-CM5-2
32	FGOALS-s2
33	GFDL-CM2p1
34	GISS-E2-H-CC
35	GISS-E2-R-CC
36	HadGEM2-AO
37	IPSL-CM5B-LR
38	MIROC-ESM-CHEM
39	MPI-ESM-P
40	MRI-ESM1
41	NorESM1-ME

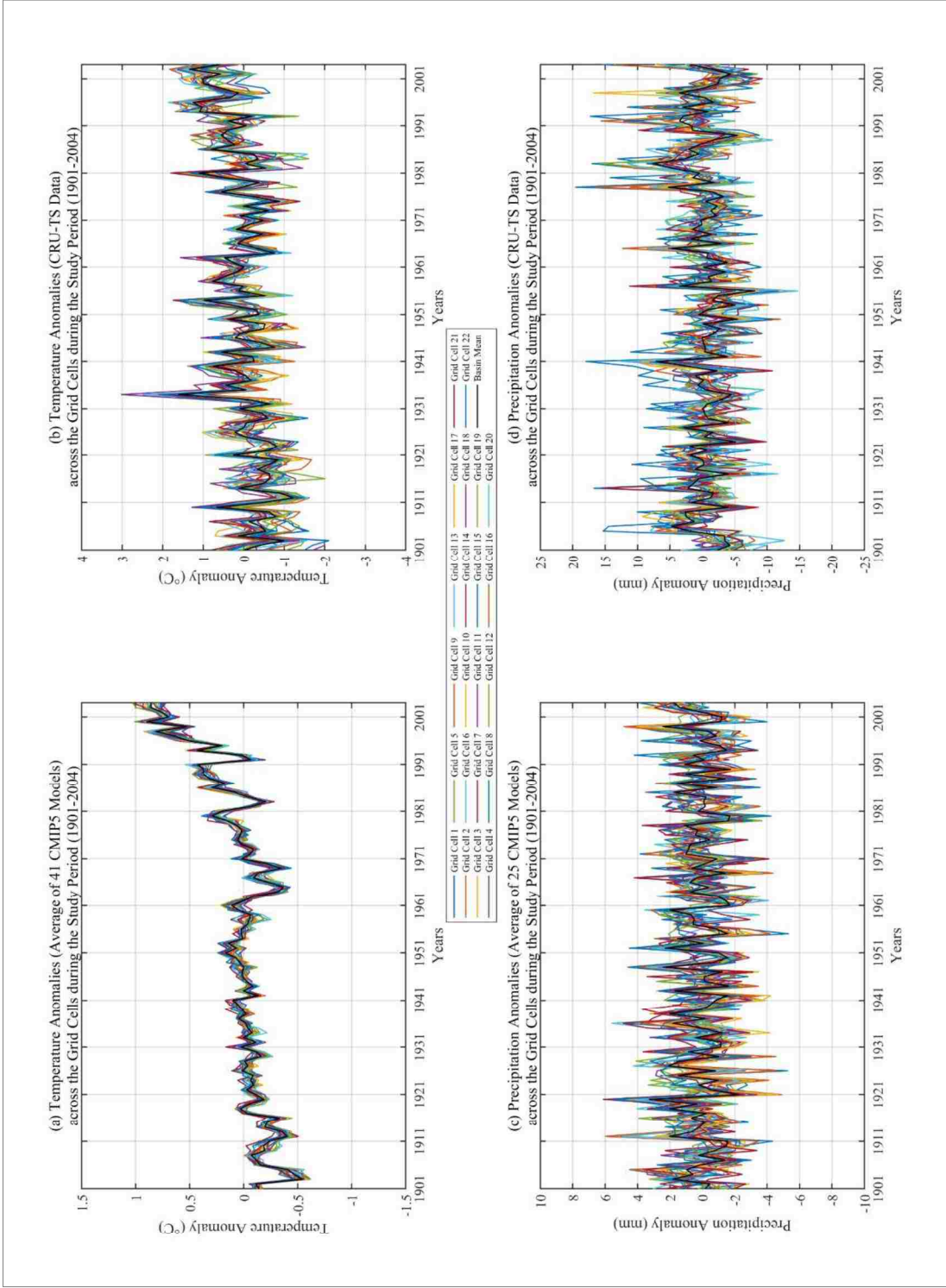|	CMIP5 Precipitation Models
1	bcc-csm1-1
2	CanESM2
3	CCSM4
4	CESM1-CAM5
5	CNRM-CM5
6	CSIRO-Mk3-6-0
7	GFDL-CM3
8	GFDL-ESM2G
9	GFDL-ESM2M
10	GISS-E2-H
11	GISS-E2-R
12	HadCM3
13	HadGEM2-CC
14	HadGEM2-ES
15	inmcm4
16	IPSL-CM5A-LR
17	IPSL-CM5A-MR
18	MIROC5
19	MIROC-ESM
20	MPI-ESM-LR
21	MRI-CGCM3
22	NorESM1-M
23	MRI-ESM1
24	NorESM1-ME
25	MPI-ESM-MR

Figure A5. 1: Temperature (**a** and **b**) and precipitation (**c** and **d**) anomalies of the CMIP5 simulation models (in terms of multi-model averages) and CRU-TS observations across the study period for each of the grid cells.

Table A5. 2: Shift-Trend results of the CMIP5 temperature models across the grid cells of the Upper and Lower Colorado River Basins. The +/- columns relate to the number of positive/negative trends or shifts. Mode of SPs among the Models (column 7) shows the year with the maximum SPs among the models along with the number of occurrences in parenthesis. The percentage in each row shows the percentage in terms of the total number of models (41) at the particular grid cell. The last row (Total) shows the percentage in terms of the total number of models across all the grid cells (41*22).

River Basin	Grid Cell No.	No. of Models with Significant Shift Points (SPs) Total	+/-	Range of SPs among the Models	Mean of SPs among the Models	Median of SPs among the Models	Mode of SPs among the Models	Standard Deviation of SPs among the Models	MK1 Before SP Total	+/-	MK1 After SP Total	+/-	MK2 Before SP Total	+/-	MK2 After SP Total	+/-	MK3 Before SP Total	+/-	MK3 After SP Total	+/-	MK4 Before SP Total	+/-	MK4 After SP Total	+/-
LCRB	1	33 (80%)	32/1	1920-1992	1966	1970	1959 (3)	18	8 (20%)	6/2	17 (41%)	17/0	9 (22%)	6/3	18 (44%)	18/0	5 (12%)	3/2	18 (44%)	15/0	5 (12%)	4/1	13 (32%)	13/0
LCRB	2	31 (76%)	30/1	1917-1988	1965	1967	1965 (2)	18	8 (20%)	7/1	16 (39%)	16/0	7 (17%)	6/1	16 (39%)	16/0	5 (12%)	5/0	15 (37%)	13/0	6 (15%)	5/1	12 (29%)	12/0
LCRB	3	33 (80%)	31/2	1917-1990	1964	1972	1972 (3)	20	7 (17%)	6/1	15 (37%)	15/0	7 (17%)	6/1	16 (39%)	16/0	8 (20%)	7/1	13 (32%)	13/0	7 (17%)	6/1	12 (29%)	12/0
LCRB	4	36 (88%)	33/3	1917-1990	1962	1972	1973 (3)	21	6 (15%)	5/1	18 (44%)	18/0	6 (15%)	5/1	18 (44%)	18/0	4 (10%)	3/1	13 (32%)	12/0	5 (12%)	4/1	15 (37%)	15/0
LCRB	5	35 (85%)	31/4	1920-1987	1960	1966	1966 (3)	20	5 (12%)	5/0	17 (41%)	17/0	7 (17%)	7/0	18 (44%)	18/0	3 (7%)	3/0	12 (29%)	14/0	4 (10%)	4/0	13 (32%)	13/0
LCRB	6	31 (76%)	28/3	1916-1992	1962	1965	1955 (3)	17	7 (17%)	6/1	19 (46%)	19/0	7 (17%)	6/1	20 (49%)	20/0	6 (15%)	5/1	14 (34%)	15/0	6 (15%)	5/1	14 (34%)	14/0
LCRB	7	32 (78%)	30/2	1920-1986	1962	1966	1966 (4)	18	8 (20%)	7/1	18 (44%)	18/0	9 (22%)	8/1	17 (41%)	17/0	4 (10%)	3/1	15 (37%)	16/0	7 (17%)	6/1	14 (34%)	14/0
LCRB	8	34 (83%)	32/2	1918-1985	1964	1971	1979 (3)	19	5 (12%)	4/1	20 (49%)	20/0	6 (15%)	5/1	20 (49%)	20/0	5 (12%)	3/2	16 (39%)	17/0	5 (12%)	4/1	16 (39%)	16/0
LCRB	9	35 (85%)	32/3	1918-1985	1961	1967	1976 (4)	19	5 (12%)	4/1	19 (46%)	19/0	5 (12%)	4/1	19 (46%)	19/0	5 (12%)	4/1	17 (41%)	17/0	5 (12%)	4/1	15 (37%)	15/0
LCRB	10	36 (88%)	31/5	1918-1990	1961	1967	1984 (3)	21	6 (15%)	5/1	17 (41%)	17/0	7 (17%)	6/1	19 (46%)	19/0	4 (10%)	4/0	17 (41%)	15/0	5 (12%)	4/1	13 (32%)	13/0
UCRB	11	36 (88%)	31/5	1919-1990	1957	1957	1936 (2)	19	9 (22%)	8/1	17 (41%)	17/0	10 (24%)	8/2	17 (41%)	17/0	6 (15%)	6/0	15 (37%)	16/0	7 (17%)	6/1	12 (29%)	12/0
UCRB	12	33 (80%)	31/2	1919-1985	1962	1968	1959 (2)	18	9 (22%)	5/4	20 (49%)	20/0	10 (24%)	6/4	18 (44%)	18/0	10 (24%)	6/4	16 (39%)	13/0	7 (17%)	4/3	15 (37%)	15/0
UCRB	13	31 (76%)	30/1	1918-1987	1959	1967	1945 (2)	21	5 (12%)	4/1	17 (41%)	17/0	5 (12%)	4/1	17 (41%)	17/0	4 (10%)	4/0	13 (32%)	15/0	4 (10%)	3/1	15 (37%)	15/0
LCRB	14	32 (78%)	30/2	1917-1987	1959	1968	1972 (3)	22	8 (20%)	6/2	19 (46%)	19/0	8 (20%)	6/2	19 (46%)	19/0	8 (20%)	6/2	15 (37%)	17/0	6 (15%)	4/2	13 (32%)	13/0
LCRB	15	34 (83%)	30/4	1917-1990	1961	1967	1973 (3)	21	7 (17%)	7/0	23 (56%)	23/0	6 (15%)	6/0	23 (56%)	23/0	6 (15%)	6/0	17 (41%)	11/0	6 (15%)	6/0	18 (44%)	18/0
UCRB	16	33 (80%)	32/1	1917-1990	1961	1969	1984 (3)	23	5 (12%)	4/1	15 (37%)	14/1	5 (12%)	4/1	16 (39%)	15/1	4 (10%)	3/1	11 (27%)	16/0	4 (10%)	3/1	11 (27%)	11/0
UCRB	17	33 (80%)	33/0	1919-1991	1965	1969	1969 (3)	20	13 (32%)	10/3	17 (41%)	17/0	12 (29%)	9/3	18 (44%)	18/0	6 (15%)	2/4	16 (39%)	16/0	11 (27%)	9/2	15 (37%)	15/0
UCRB	18	33 (80%)	33/0	1919-1993	1968	1973	1975 (3)	18	6 (15%)	4/2	17 (41%)	17/0	6 (15%)	4/2	17 (41%)	17/0	5 (12%)	3/2	16 (39%)	13/0	5 (12%)	3/2	14 (34%)	14/0
LCRB	19	31 (76%)	30/1	1917-1990	1963	1970	1979 (2)	21	7 (17%)	5/2	16 (39%)	16/0	7 (17%)	5/2	16 (39%)	16/0	6 (15%)	4/2	13 (32%)	12/0	6 (15%)	4/2	13 (32%)	13/0
UCRB	20	32 (78%)	30/2	1917-1990	1962	1971	1973 (2)	22	6 (15%)	5/1	13 (32%)	13/0	6 (15%)	5/1	15 (37%)	15/0	7 (17%)	5/2	12 (29%)	18/0	6 (15%)	5/1	12 (29%)	12/0
UCRB	21	34 (83%)	32/2	1919-1989	1961	1966	1965 (3)	19	9 (22%)	5/4	22 (54%)	22/0	9 (22%)	5/4	22 (54%)	22/0	8 (20%)	4/4	18 (44%)	18/0	7 (17%)	5/2	18 (44%)	18/0
UCRB	22	33 (80%)	32/1	1920-1993	1965	1967	1965 (3)	17	7 (17%)	5/2	21 (51%)	21/0	7 (17%)	5/2	21 (51%)	21/0	6 (15%)	3/3	18 (44%)	0/0	6 (15%)	5/1	17 (41%)	17/0
Total		731 (81%)	684/47						156 (17%)	123/33	393 (44%)	392/1	161 (18%)	126/35	400 (44%)	399/1	125 (14%)	92/33	330 (37%)	330/0	130 (14%)	103/27	310 (34%)	310/0

171

Note: LCRB = Lower Colorado River Basin; Grid Cells: 1-10, 14, and 15. UCRB = Upper Colorado River Basin; Grid Cells: 11-13 and 16-22.

Table A5. 3: Shift-Trend results of the CRU-TS temperature data across the grid cells of the Upper and Lower Colorado River Basins.

River Basin	Grid cell No.	Significant Shift Point (SP)	SP Direction	Direction of Significant Trend Before SP (MK1)	Direction of Significant Trend After SP (MK1)	Direction of Significant Trend Before SP (MK2)	Direction of Significant Trend After SP (MK2)	Direction of Significant Trend Before SP (MK3)	Direction of Significant Trend After SP (MK3)	Direction of Significant Trend Before SP (MK4)	Direction of Significant Trend After SP (MK4)
LCRB	1	1956	+	+	+	+	+			+	
LCRB	2	1933	+								
LCRB	3	1976	+		+		+		+		+
LCRB	4	1985	+								
LCRB	5	1985	+								
LCRB	6	1933	+	+		+	+	+		+	
LCRB	7	1933	+		+		+				
LCRB	8	1979	+		+		+		+		+
LCRB	9	1976	+								
LCRB	10	1932	+								
UCRB	11	1930	+								
UCRB	12	1957	+		+		+		+		+
UCRB	13	1976	+		+		+		+		+
LCRB	14	1932	+	-		-		-		-	
LCRB	15	1932	+					-			
UCRB	16	1957	+		+		+		+		+
UCRB	17	1924	+	+	+	+	+	+			
UCRB	18	1953	+	+	+	+	+	+		+	
UCRB	19	1952	+	+	+	+	+	+		+	
UCRB	20	1932	+								
UCRB	21	1932	+	+	+	+	+	+	+	+	
UCRB	22	1976	+	+	+	+	+	+	+	+	+
Total (+/-)			22/0	7/1	12/0	7/1	13/0	6/2	7/0	6/1	6/0

Note: LCRB = Lower Colorado River Basin; Grid Cells: 1-10, 14, and 15. UCRB = Upper Colorado River Basin; Grid Cells: 11-13 and 16-22.

Table A5. 4: Shift-Trend results of the CMIP5 precipitation models across the grid cells of the Upper and Lower Colorado River Basins. The +/- columns relate to the number of positive/negative trends or shifts. Mode of SPs among the Models (column 7) shows the year with the maximum SPs among the models along with the number of occurrences in parenthesis. The percentage in each row shows the percentage in terms of the total number of models (25) at each of the particular grid cells. The last row (Total) shows the percentage in terms of the total number of models across all the grid cells (25*22).

River Basin	Grid Cell No.	Number of Models with Significant Shift Points (SPs)		Range of SPs among the Models	Mean of SPs among the Models	Median of SPs among the Models	Mode of SPs among the Models	Standard Deviation of SPs among the Models	Number of Models with Significant Trends Before SP (MK1)		Number of Models with Significant Trends After SP (MK1)		Number of Models with Significant Trends Before SP (MK2)		Number of Models with Significant Trends After SP (MK2)		Number of Models with Significant Trends Before SP (MK3)		Number of Models with Significant Trends After SP (MK3)		Number of Models with Significant Trends Before SP (MK4)		Number of Models with Significant Trends After SP (MK4)	
		Total	+/-						Total	+/-	Total	+/-	Total	+/-	Total	+/-	Total	+/-	Total	+/-	Total	+/-	Total	+/-
LCRB	1	5 (20%)	3/2	1940-1970	1953	1952	–	10	2 (8%)	1/1	0 (0%)	0/0	2 (8%)	1/1	0 (0%)	0/0	4 (16%)	1/3	0 (0%)	0/0	2 (8%)	1/1	0 (0%)	0/0
LCRB	2	8 (32%)	3/5	1922-1971	1948	1945	–	15	2 (8%)	2/0	0 (0%)	0/0	2 (8%)	2/0	0 (0%)	0/0	2 (8%)	2/0	1 (4%)	1/0	2 (8%)	2/0	0 (0%)	0/0
LCRB	3	3 (12%)	3/0	1934-1966	1951	1953	–	13	1 (4%)	0/1	0 (0%)	0/0	1 (4%)	0/1	0 (0%)	0/0	2 (8%)	1/1	0 (0%)	0/0	1 (4%)	0/1	0 (0%)	0/0
LCRB	4	2 (8%)	0/2	1928-1946	1937	1937	–	9	0 (0%)	0/0	0 (0%)	0/0	0 (0%)	0/0	0 (0%)	0/0	3 (12%)	1/2	0 (0%)	0/0	0 (0%)	0/0	0 (0%)	0/0
LCRB	5	1 (4%)	0/1	1926-1926	1926	1926	–	0	0 (0%)	0/0	0 (0%)	0/0	0 (0%)	0/0	0 (0%)	0/0	1 (4%)	0/1	0 (0%)	0/0	0 (0%)	0/0	0 (0%)	0/0
LCRB	6	7 (28%)	2/5	1939-1968	1957	1960	–	10	3 (12%)	2/1	0 (0%)	0/0	2 (8%)	2/0	0 (0%)	0/0	3 (12%)	2/1	0 (0%)	0/0	3 (12%)	2/1	0 (0%)	0/0
LCRB	7	7 (28%)	2/5	1943-1971	1958	1959	–	9	3 (12%)	3/0	0 (0%)	0/0	3 (12%)	3/0	0 (0%)	0/0	2 (8%)	2/0	0 (0%)	0/0	3 (12%)	3/0	0 (0%)	0/0
LCRB	8	5 (20%)	3/2	1924-1971	1951	1954	–	17	1 (4%)	1/0	1 (4%)	1/0	1 (4%)	1/0	1 (4%)	1/0	4 (16%)	2/2	1 (4%)	1/0	1 (4%)	1/0	1 (4%)	1/0
LCRB	9	7 (28%)	4/3	1929-1975	1949	1946	1946 (2)	13	0 (0%)	0/0	2 (8%)	2/0	0 (0%)	0/0	2 (8%)	2/0	0 (0%)	0/0	3 (12%)	3/0	0 (0%)	0/0	2 (8%)	2/0
LCRB	10	8 (32%)	4/4	1923-1973	1950	1951	–	14	1 (4%)	1/0	1 (4%)	1/0	1 (4%)	1/0	1 (4%)	1/0	1 (4%)	1/0	2 (8%)	2/0	1 (4%)	1/0	1 (4%)	1/0
UCRB	11	5 (20%)	3/2	1923-1987	1954	1963	–	25	1 (4%)	1/0	1 (4%)	1/0	1 (4%)	1/0	1 (4%)	1/0	2 (8%)	1/1	1 (4%)	1/0	1 (4%)	1/0	1 (4%)	1/0
UCRB	12	4 (16%)	3/1	1940-1970	1954	1952	–	11	3 (12%)	1/2	0 (0%)	0/0	3 (12%)	1/2	0 (0%)	0/0	3 (12%)	1/2	0 (0%)	0/0	3 (12%)	1/2	0 (0%)	0/0
UCRB	13	4 (16%)	2/2	1924-1976	1958	1966	–	20	0 (0%)	0/0	1 (4%)	1/0	0 (0%)	0/0	1 (4%)	1/0	1 (4%)	0/1	0 (0%)	0/0	0 (0%)	0/0	1 (4%)	1/0
LCRB	14	6 (24%)	3/3	1916-1968	1950	1953	–	19	0 (0%)	0/0	1 (4%)	1/0	0 (0%)	0/0	1 (4%)	1/0	1 (4%)	1/0	1 (4%)	1/0	0 (0%)	0/0	0 (0%)	0/0
LCRB	15	8 (32%)	2/6	1921-1967	1935	1928	–	15	0 (0%)	0/0	2 (8%)	2/0	0 (0%)	0/0	2 (8%)	2/0	1 (4%)	1/0	2 (8%)	2/0	0 (0%)	0/0	1 (4%)	1/0
UCRB	16	4 (16%)	2/2	1932-1966	1945	1940	–	13	2 (8%)	1/1	0 (0%)	0/0	2 (8%)	1/1	0 (0%)	0/0	1 (4%)	0/1	0 (0%)	0/0	2 (8%)	1/1	0 (0%)	0/0
UCRB	17	3 (12%)	0/3	1953-1978	1962	1954	–	12	1 (4%)	1/0	0 (0%)	0/0	1 (4%)	1/0	0 (0%)	0/0	2 (8%)	2/0	0 (0%)	0/0	1 (4%)	1/0	0 (0%)	0/0
UCRB	18	3 (12%)	0/3	1940-1954	1949	1953	–	6	1 (4%)	1/0	0 (0%)	0/0	1 (4%)	1/0	0 (0%)	0/0	2 (8%)	1/1	1 (4%)	1/0	1 (4%)	1/0	0 (0%)	0/0
UCRB	19	5 (20%)	2/3	1940-1977	1960	1966	–	15	1 (4%)	1/0	0 (0%)	0/0	1 (4%)	1/0	0 (0%)	0/0	2 (8%)	2/0	1 (4%)	0/1	1 (4%)	1/0	0 (0%)	0/0
UCRB	20	4 (16%)	3/1	1951-1974	1961	1960	–	9	2 (8%)	0/2	1 (4%)	1/0	2 (8%)	0/2	1 (4%)	1/0	3 (12%)	1/2	1 (4%)	1/0	2 (8%)	0/2	1 (4%)	1/0
UCRB	21	7 (28%)	3/4	1943-1968	1958	1963	1968 (2)	11	1 (4%)	1/0	0 (0%)	0/0	1 (4%)	1/0	0 (0%)	0/0	3 (12%)	3/0	0 (0%)	0/0	1 (4%)	1/0	1 (4%)	1/0
UCRB	22	8 (32%)	3/5	1922-1971	1952	1954	–	14	1 (4%)	1/0	0 (0%)	0/0	1 (4%)	1/0	0 (0%)	0/0	1 (4%)	1/0	0 (0%)	0/0	1 (4%)	1/0	0 (0%)	0/0
Total		114 (21%)	50/64						26 (5%)	18/8	10 (2%)	10/0	25 (5%)	18/7	10 (2%)	10/0	44 (8%)	26/18	14 (3%)	13/1	26 (5%)	18/8	8 (1%)	8/0

Note: LCRB = Lower Colorado River Basin; Grid Cells: 1-10, 14, and 15. UCRB = Upper Colorado River Basin; Grid Cells: 11-13 and 16-22.

173

Table A5. 5: Shift-Trend results of the CRU-TS precipitation data across the grid cells of the Upper and Lower Colorado River Basins.

River Basin	Grid cell No.	Significant Shift Point (SP)	SP Direction	Direction of Significant Trend Before SP (MK1)	Direction of Significant Trend After SP (MK1)	Direction of Significant Trend Before SP (MK2)	Direction of Significant Trend After SP (MK2)	Direction of Significant Trend Before SP (MK3)	Direction of Significant Trend After SP (MK3)	Direction of Significant Trend Before SP (MK4)	Direction of Significant Trend After SP (MK4)
LCRB	1	1945	-								-
LCRB	2										
LCRB	3										
LCRB	4										
LCRB	5	1962	+		-		-		-		
LCRB	6	1956	+					-			
LCRB	7	1956	+	-		-		-		-	
LCRB	8										
LCRB	9	1977	+	-		-		-		-	
LCRB	10										
UCRB	11										
UCRB	12										
UCRB	13	1964	+	-		-		-		-	
LCRB	14	1963	+								
LCRB	15										
UCRB	16	1962	+								
UCRB	17	1940	-								
UCRB	18										
UCRB	19										
UCRB	20										
UCRB	21										
UCRB	22										

Total (+/-)	7/2	0/3	0/1	0/3	0/1	0/4	0/1	0/3	0/1

174

Note: LCRB = Lower Colorado River Basin; Grid Cells: 1-10, 14, and 15. UCRB = Upper Colorado River Basin; Grid Cells: 11-13 and 16-22.

REFERENCES

Ahmed, W., Rais, M., Bano, R., Tamaddun, K., Ahmad, S., 2018. Water sharing, governance, and management among the provinces in Pakistan: A support of evidence-based decision support system. ASCE World Environmental & Water Resources Congress, Minneapolis, MN, June 3-7.

Ahn, K., Palmer, R., 2015. Trend and Variability in Observed Hydrological Extremes in the United States. J Hydrol Eng 10.1061/ (ASCE) HE.1943-5584.0001286, 04015061.

Abeysingha, N. S., Singh, M., Sehgal, V. K., Khanna, M., Pathak, H., 2016. Analysis of trends in streamflow and its linkages with rainfall and anthropogenic factors in Gomti River basin of North India. Theoretical and Applied Climatology, 123(3-4), 785–799. doi:10.1007/s00704-015-1390-5.

Allan, R. J., Reason, C. J. C., Lindesay, J. A., Ansell, T. J., 2003. Protracted ENSO episodes and their impacts in the Indian Ocean region, Deep Sea Res., Part II, 50, 2331–2347.

Arnell, N. W., 2011. Incorporating climate change into water resources planning in England and Wales. J. Amer. Water Resour. Assoc., 47, 541–549.

Ashok, K., Guan, Z., Yamagata, T., 2001. Impact of the Indian Ocean dipole on the relationship between the Indian monsoon rainfall and ENSO, Geophys. Res. Lett., 28, 4499–4502.

Ashok, K., Guan, Z., Saji, N. H., Yamagata, T., 2004. Individual combined influences of the ENSO and Indian Ocean Dipole on the Indian summer monsoon. J. Clim. 17, 3141–3155.

Asrar, G., Busalacchi, A., Hurrel, J., 2012. Developing plans and priorities for climate science in service to society. Eos, Trans. Amer. Geophys. Union, 93, 128–128.

Ateeq-ur-Rauf, Ghumman, A. R., Ahmad, S., Hashmi, H. N., 2018. Performance assessment of artificial neural networks and support vector regression models for stream flow predictions. Environmental Monitoring and Assessment, 190(12), 704. https://doi.org/10.1007/s10661-018-7012-9.

Barnett, T. P., Pierce, D. W., Saravanan, R., Planck, M., 1999. Origins of the midlatitude Pacific decadal variability. Geophysical Research Letters 26 (10), 1453–1456.

Bayazit, M., 2015. Nonstationarity of Hydrological Records and Recent Trends in Trend Analysis: A State-of-the-art Review. Environmental Processes, 2(3), 527–542. http://doi.org/10.1007/s40710-015-0081-7.

Bayazıt, M., Aksoy, H., 2001. Using wavelets for data generation. Journal of Applied Statistics 28(2), pp 157–166.

Beebee, R. A., Manga, M., 2004. Variation in the relationship between snowmelt runoff in Oregon and ENSO and PDO. Journal of the American Water Resources Association 40 (02099), 1011–1024. doi:10.1111/j.1752-1688.2004.tb01063.x.

Belayneh, A., Adamowski, J., Khalil, B., Quilty, J., 2016. Coupling machine learning methods with wavelet transforms and the bootstrap and boosting ensemble approaches for drought prediction. Atmospheric Research, 172–173, 37–47. http://doi.org/10.1016/j.atmosres.2015.12.017.

Bhandari, S., Kalra, A., Tamaddun, K., Ahmad, S., 2018. Relationship between Ocean-Atmospheric Climate Variables and Regional Streamflow of the Conterminous United States. Hydrology, 5(2), 30. https://doi.org/10.3390/hydrology5020030.

Bhandari, S., Thakur, B., Kalra, A., Miller, W. P., Lakshmi, V., Pathak, P., 2019. Streamflow Forecasting Using Singular Value Decomposition and Support Vector Machine for the Upper Rio Grande River Basin. Journal of the American Water Resources Association, 1–20. https://doi.org/10.1111/1752-1688.12733.

Birsan, M. V., Molnar, P., Burlando, P., Pfaundler, M., 2005. Streamflow trends in Switzerland. J Hydrol 314 (1–4):312–329.

Bonan, G. B., 2008. Forests and climate change: Forcings, feedbacks, and the climate benefits of forests. Science. 320, 1444–1449.

Bounoua, L., Hall, F. G., Sellers, P. J., Kumar, A., Collatz, G. J., Tucker, C. J., Imhoff, M. L., 2010. Quantifying the negative feedback of vegetation to greenhouse warming: A modeling approach. Geophys. Res. Lett. 37, L23701.

Boyer, C., Chaumont, D., Chartier, I., Roy, A. G., 2010. Impact of climate change on the hydrology of St. Lawrence tributaries. J Hydrol 384 (1–2):65–83.

Bukhary, S., Ahmad, S., Batista, J., 2018. Analyzing land and water requirements for solar deployment in the Southwestern United States. Renewable and Sustainable Energy Reviews, 82(April 2017), 3288–3305. https://doi.org/10.1016/j.rser.2017.10.016

Burn, D. H., Sharif, M., Zhang, K., 2010. Detection of trends in hydrological extremes for Canadian watersheds. Hydrol Process 24 (13):1781–1790.

Burn, D. H., 2008. Climatic influences on streamflow timing in the headwaters of the Mackenzie River Basin. J. Hydrol. 352, 225–238.

Carrier, C., Kalra, A., Ahmad, S., 2016. Long-range precipitation forecast using paleoclimate reconstructions in the western United States. Journal of Mountain Science 13 (4), 614–632. doi:10.1007/s11629-014-3360-2.

Cayan, D. R., 1996. Interannual climate variability and snowpack in the western United States. J. Climate, 9, 928–948.

Cayan, D. R., Redmond, K. T., Riddle, L. G., 1999. ENSO and hydrological extreme in the western United States. Journal of Climate 12, 2881–2893. doi:10.1175/1520-0442(1999) 012<2881:EAHEIT>2.0.CO;2.

Changnon, D., McKee, T. B., Doesken, N. J. 1991. Hydroclimatic variability in the Rocky Mountains. Journal of the American Water Resources Association, 27(5), 733–743. doi:10.1111/j.1752-1688.1991.tb01471.x.

Charles, C. D., 1997. Interaction between the ENSO and the Asian Monsoon in a Coral Record of Tropical Climate. Science, 69(1), 27–42. doi:10.1126/science.277.5328.925.

Cheo, A. E., 2016. Understanding seasonal trend of rainfall for the better planning of water harvesting facilities in the Far-North region, Cameroon. Water Utility Journal, (13), 3–11.

Chen, C., Kalra, A., Ahmad, S., 2018. Hydrologic responses to climate change using downscaled GCM data on a watershed scale. Journal of Water and Climate Change, 10(1), 63–77. https://doi.org/10.2166/wcc.2018.147.

Clark, J. S., Yiridoe, E. K., Burns, N. D., Astatkie, T., 2000. Regional climate change: trend analysis of temperature and precipitation series at selected Canadian sites. Can J Agric Econ 48 (1):27–38.

Coscarelli, R., Caloiero, T., Lo Feudo, T., 2013. Relationship between winter rainfall amount and teleconnection patterns in Southern Italy. European Water, (43), 13–21.

Coulibaly, P., Burn, D. H., 2004. Wavelet analysis of variability in annual Canadian streamflows. Water Resour Res 40 (3):W03105.

Datta, R., Gupta, M., 1968. Synoptic study of the formation and movements of Western Depressions. Indian Journal of Meteorology & Geophysics, India Meteorological Department.

David, V. S., Rajasekaran, S., 2009. Pattern Recognition Using Neural and Functional Networks. Springer-Verlag, Berlin, Germany.

Dawadi, S., Ahmad, S., 2013. Evaluating the impact of demand-side management on water resources under changing climatic conditions and increasing population. Journal of Environmental Management 114:261–75. doi:10.1016/j.jenvman.2012.10.015.

Deser, C., Knutti, R., Solomon, S., Phillips, A. S., 2012a. Communication of the role of natural variability in future North American climate. Nature Climate Change, 2(11), 775–779. http://doi.org/10.1038/nclimate1562.

Deser, C., Phillips, A., Bourdette, V., Teng, H., 2012b. Uncertainty in climate change projections: The role of internal variability. Climate Dynamics, 38(3–4), 527–546. http://doi.org/10.1007/s00382-010-0977-x.

177

Dettinger, M. D., Diaz, H. F., 2000. Global characteristics of streamflow seasonality and variability. J Hydrometeorology 1 (4):289–310.

Diffenbaugh, N. S., Swain, D. L., Touma, D., 2015. Anthropogenic warming has increased drought risk in California, Proc. Natl. Acad. Sci. U.S.A. 112(13), 3931–3936.

Dimri, A., 2004. Models to improve winter minimum surface temperature forecasts, Delhi, India. Meteorological Applications, 11, pp. 129-139, Royal Meteorological Society, Cambridge University Press.

Dimri, A. P., 2013. Relationship between ENSO phases with Northwest India winter precipitation. Int. J. Climatol. 33, 1917–1923.

Dirmeyer, P. A., Brubaker, K. L., 2006. Evidence for trends in the northern hemisphere water cycle. Geophys. Res. Lett. 33, L14712.

Drago, A. F., Boxall, S. R., 2002. Use of the wavelet transform on hydro-meteorological data. Physics and Chemistry of the Earth 27 (32–34):1387–1399

Dudley, R. W., Hodgkins, G. A., McHale, M. R., Kolian, M. J., Renard, B., 2017. Trends in snowmelt-related streamflow timing in the conterminous United States. Journal of Hydrology, 547, 208–221. http://doi.org/10.1016/j.jhydrol.2017.01.051.

Durdu, Ö. F., 2010. Effects of climate change on water resources of the Büyük Menderes River basin, western Turkey. Turk J Agric Forest 34 (4):319–332

Foufoula-Georgiou, E., Kumar, P., 1995. Wavelets in Geophysics. Academic Press, San Diego, CA, USA, p. 373.

Gadgil, S., Vinaychandran, P. N., Francis, P. A., Gadgil, S., 2004. Extremes of Indian summer monsoon rainfall, ENSO, equatorial Indian Ocean Oscillation. Geophys. Res. Lett. 31, L12213.

Gaucherel, C., 2002. Use of wavelet transform for temporal characterisation of remote watersheds. Journal of Hydrology 269, pp 101–121.

Geological Survey of India (GSI), 2016. Geological Survey of India, MOI, Government of India. http://www.portal.gsi.gov.in/ (accessed March 10, 2016).

Griffin, D., Anchukaitis, K. J., 2014. How unusual is the 2012–2014 California drought? Geophys. Res. Lett., 41, 9017–9023, doi:10.1002/2014GL062433.

Grinsted, A., Moore, J. C., Jevrejeva, S., 2004. Application of the cross wavelet transform and wavelet coherence to geophysical time series. Nonlinear Processes in Geophysics 11:561–566. doi:10.1002/etep.

Groisman, P. Y., Knight, R. W., Karl, T. R., 2001. Heavy precipitation and high streamflow in the contiguous United States: trends in the twentieth century. Bull Am Meteorol Soc 82 (2):219–246.

Guillevic, P., Koster, R. D., Suarez, M. J., Bounoua, L., Collatz, G. J., Los, S. O., Mahanama, S. P. P., 2002. Influence of the interannual variability of vegetation on the surface energy balance – A global sensitivity study. J. Hydrometeorol. 3, 617–629.

Hamed, K. H., Ramachandra Rao, A., 1998. A modified Mann-Kendall trend test for autocorrelated data. Journal of Hydrology, 204(1–4), 182–196. http://doi.org/10.1016/S0022-1694(97)00125-X.

Hamed, K. H., 2008: Trend detection in hydrologic data: The Mann–Kendall trend test under the scaling hypothesis. Journal of Hydrology, 349(3–4), 350–363. http://doi.org/10.1016/j.jhydrol.2007.11.009.

Hamlet, A. F., Mote, P. W., Clark, M. P., Lettenmaier, D. P., 2005. Effects of temperature and precipitation variability on snowpack trends in the western United States. J Clim 18 (21):4545–4561.

Hanson, R. T., Newhouse, M. W., Dettinger, M. D., 2004. A methodology to assess relations between climatic variability and variations in hydrologic time-series in the southwestern United States. Journal of Hydrology 287 (1), 252–269. http:// dx.doi.org/ 10.1016/j.jhydrol.2003.10.006.

Helsel, D. R., Frans, L. M., 2006. The regional Kendall test for trend. Environmental Science and Technology 40:4066-4073.

Hunter, T., Tootle, G., Piechota, T., 2006. Oceanic-atmospheric variability and western U.S. snowfall. Geophysical Research Letters, 33(13), 1–5. doi:10.1029/2006GL026600.

Huntington, T. G., 2006. Evidence for intensification of the global water cycle: Review and synthesis. J. Hydrol. 319, 83–95.

India Water Portal (IWP), 2016. India Water Portal Met Data. http://www.indiawaterportal.org/met_data/ (accessed March, 12, 2016).

Intergovernmental Panel on Climate Change (IPCC), 2013. Climate Change 2013: The Physical Science Basis; IPCC: Geneva, Switzerland, p. 33, doi:10.1017/CBO9781107415324.

Intergovernmental Panel on Climate Change (IPCC), 2014. Climate Change 2014 Synthesis Report Summary Chapter for Policymakers. IPCC, 31. http://doi.org/10.1017/CBO9781107415324.

Intergovernmental Panel on Climate Change (IPCC), 2019. Climate Change 2022 Synthesis Report. Retrieved from: https://www.ipcc.ch/report/sixth-assessment-report-cycle/

Jevrejeva, S., Moore, J. C., Grinsted, A., 2003. Influence of the arctic oscillation and El Niño-Southern Oscillation (ENSO) on ice conditions in the Baltic Sea: the wavelet approach. Journal of Geophysical Research 108 (D21), 4677. doi:10. 1029/2003JD003417.

Jobe, A., Kalra, A., Ibendahl, E., 2018. Conservation Reserve Program effects on floodplain land cover management. Journal of Environmental Management, 214, 305–314. https://doi.org/10.1016/j.jenvman.2018.03.016

Ju, J., Slingo, J., 1995. The Asian summer monsoon and ENSO. Quart. J. Roy. Meteor. Soc., 121, 1133–1168.

Kahya, E., Dracup, J. A., 1993. U.S. streamflow patterns in relation to the El Niño/ Southern Oscillation. Water Resour. Res. 29 (8), 2491–2503. http://dx.doi.org/ 10.1029/93WR00744.

Kalra, A., Piechota, T. C., Davies, R., and Tootle, G. A., 2008. Changes in U.S. streamflow and western U.S. snowpack. J. Hydrol. Eng. 13 (3), 156–163.

Kalra, A., Sagarika, S., Pathak, P., Ahmad, S., 2017. Hydro-climatological changes in the Colorado River Basin over a century. Hydrological Sciences Journal, 62(14), 2280–2296. http://doi.org/10.1080/02626667.2017.1372855.

Karthikeyan, L., Nagesh Kumar, D., 2013. Predictability of nonstationary time series using wavelet and EMD based ARMA models. Journal of Hydrology 502:103–119. doi:10.1016/j.jhydrol.2013.08.030

Kaul, H., 1998. Rediscovery of Ladakh. New Delhi: Indus Publishing, ISBN 9788173870866.

Kendall, M. G., 1975. Rank Correlation Methods; Charles Griffin: London, UK.

Kandissounon, G. A., Kalra, A., Ahmad, S., 2018. Integrating System Dynamics and Remote Sensing to Estimate Future Water Usage and Average Surface Runoff in Lagos, Nigeria. Civil Engineering Journal, 4(2), 378. https://doi.org/10.28991/cej-030998.

Khaliq, M. N., Ouarda, T. B. M. J., Gachon, P., Sushama, L., St-Hilaire, A., 2009. Identification of hydrological trends in the presence of serial and cross correlations: A review of selected methods and their application to annual flow regimes of Canadian rivers. Journal of Hydrology 368(1–4):117–130. http://doi.org/10.1016/j.jhydrol.2009.01.035.

Khare, D., Mondal, A., Kundu, S., Mishra, P. K., 2016. Climate change impact on soil erosion in the Mandakini River Basin, North India. Applied Water Science. doi:10.1007/s13201-016-0419-y.

Klein, S. A, Soden, B. J., Lau, N. C., 1999. Remote Sea Surface Temperature Variations during ENSO: Evidence for a Tropical Atmospheric Bridge. Journal of Climate, 12, 917–932. doi:10.1175/1520-0442(1999)012<0917:RSSTVD>2.0.CO;2.

Kohli, R. K., Batish, D. R., Singh, H. P., Dogra, K. S., 2006. Status, invasiveness and environmental threats of three tropical American invasive weeds (Parthenium hysterophorus L., Ageratum conyzoides L., Lantana camara L.) in India. Biological Invasions, 8(7), 1501–1510. doi:10.1007/s10530-005-5842-1.

Koutsoyiannis, D., 2003. Climate change, the Hurst phenomenon, and hydrological statistics. Hydrological Sciences Journal, 48(1), 3–24. http://doi.org/10.1623/hysj.48.1.3.43481.

Kramer, R., Bounoua, L., Zhang, P., Wolfe, R., Huntington, T., Imhoff, M., Thome, K., Noyce, G., 2015. Evapotranspiration Trends over the Eastern United States During the 20th Century. Hydrology, 2(2), 93–111. doi:10.3390/hydrology2020093.

Krishnamurthi, V., Goswami, B. N., 2000. Indian Monsoon ENSO relationship on interdecadal timescale. American Meteorological Society, 13, 579–595. doi:10.1175/1520-0442(2000)013<0579:IMEROI>2.0.CO;2.

Küçük M., Ağiralioğlu N (2006) Wavelet Regression Technique for Streamflow Prediction. Journal of Applied Statistics 33(9):943–960. doi:10.1080/02664760600744298.

Kumar, K., Rajagopalan, B., Cane, M., 1999. On the weakening relationship between the Indian monsoon and ENSO. Science (New York, N.Y.), 284(5423), 2156–9. doi:10.1126/science.284.5423.2156.

Kumar, K., Rajagopalan, B., Hoerling, M., Bates, G., Cane, M., 2006. Unraveling the Mystery of Indian Monsoon Failure during El Niño. Science, 314, 115-119.

Kumar, S., Merwade, V., Kam, J., Thurner, K., 2009. Streamflow trends in Indiana: Effects of long term persistence, precipitation and subsurface drains. Journal of Hydrology, 374(1–2), 171–183. http://doi.org/10.1016/j.jhydrol.2009.06.012.

Kumar, S., Merwade, V., Kinter, J. L., Niyogi, D., 2013. Evaluation of temperature and precipitation trends and long-term persistence in CMIP5 twentieth-century climate simulations. Journal of Climate, 26(12), 4168–4185. http://doi.org/10.1175/JCLI-D-12-00259.1.

Labat, D., 2005. Recent advances in wavelet analyses: Part 1. A review of concepts. J Hydrol 314:(1–4) 275–288.

Labat, D., 2008. Wavelet analysis of the annual discharge records of the world's largest rivers. Advances in Water Resources 31(1):109–117. doi:10.1016/j.advwatres.2007.07.004.

Labat, D., Goddéris, Y., Probst, J. L., Guyot, J. L., 2004. Evidence for global runoff increase related to climate warming. Adv Water Resour 27 (6):631–642.

Lau, K. M., Weng, H., 1995. Climate signal detection using wavelet transform: how to make a time-series sing. Bulletin of the American Meteorological Society 76, 2391–2402.

Lettenmaier, D. P., Wood, E. F., Wallis, J. R., 1994. Hydro-climatological trends in the continental United States, 1948-88. J. Clim., 7, 586–607.

Levis, S., Foley, J. A., Pollard, D., 2000. Large-scale vegetation feedbacks on a doubled CO2 climate. J. Clim. 13, 1313–1325.

Lins, H., Slack, J., 1999. Streamflow trends in the United States. Geophysical Research Letters 26(2):227–230. http://dx.doi.org/10.1029/1998GL900291

Lins, H. F., 2012. USGS Hydro-Climatic Data Network 2009 (HCDN–2009). US Geological Survey Fact Sheet 2012–3047 p 4. http://pubs.usgs.gov/fs/2012/ 3047/

Loo, Y. Y., Billa, L., Singh, A., 2015. Effect of climate change on seasonal monsoon in Asia and its impact on the variability of monsoon rainfall in Southeast Asia. Geoscience Frontiers, 6(6), 817–823. doi:10.1016/j.gsf.2014.02.009.

Lynch, C., Seth, A., Thibeault, J., 2016. Recent and projected annual cycles of temperature and precipitation in the Northeast United States from CMIP5. Journal of Climate, 29(1), 347–365. http://doi.org/10.1175/JCLI-D-14-00781.1.

Mallakpour, I., Villarini, G., 2016. A simulation study to examine the sensitivity of the Pettitt test to detect abrupt changes in mean. Hydrological Sciences Journal, 61(2), 245–254. http://doi.org/10.1080/02626667.2015.1008482.

Mann, H. B., 1945. Nonparametric tests against trend. Econom. J. Econom. Soc., 13, 245–259.

Mauget, S. A., 2003. Multidecadal regime shifts in U.S. streamflow, precipitation, and temperature at the end of the twentieth century. Journal of Climate, 16(23), 3905–3916. doi:10.1175/1520-0442(2003)016<3905:MRSIUS>2.0.CO;2.

Mazdiyasni, O., AghaKouchak, A., 2015. Substantial increase in concurrent droughts and heatwaves in the United States. Proceedings of the National Academy of Sciences, 112(37), 11484–11489. doi:10.1073/pnas.1422945112.

McBean, E., Motiee, H., 2006. Assessment of impacts of climate change on water resources– a case study of the Great Lakes of North America. Hydrology and Earth System Sciences Discussions 3(5):3183–3209. doi:10.5194/hessd-3-3183-2006.

McCabe, G. J., Legates, D. R., 1995. Relationships between 700 hPa height anomalies and 1 April snowpack accumulations in the western USA. Int. J. Climatol., 15, 517–530.

McCabe, G. J., Dettinger, M. D., 2002. Primary Modes and Predictability of Year-to-Year Snowpack Variations in the Western United States from Teleconnections with Pacific Ocean Climate. Journal of Hydrometeorology, 3(1), 13–25. doi:10.1175/1525-7541(2002)003<0013:PMAPOY>2.0.CO;2.

McCabe, G. J., Wolock, D. M., 2002. A step increase in streamflow in the conterminous United States. Geophysical Research Letters 29(24):2185. doi:10.1029/2002GL015999.

McCabe, G. J., Betancourt, J. L., Hidalgo, H. G., 2007. Associations of decadal to multidecadal sea-surface temperature variability with Upper Colorado River flow. J Am Water Resour Assoc 43 (1):183–192.

McCabe, G. J., Wolock, D. M., 2015. Spatial and temporal patterns in conterminous United States streamflow characteristics. Geophysical Research Letters 41(September). doi:10.1002/2014GL061980.

Melesse, A. M., Ahmad, S., McClain, M. E., Wang, X., Lim, Y. H., 2011. Suspended sediment load prediction of river systems: An artificial neural network approach. Agricultural Water Management 98(5):855–866. doi:10.1016/j.agwat.2010.12.012.

Miller, W. P., Piechota, T. C., 2008. Regional analysis of trend and step changes observed in hydroclimatic variables around the Colorado River Basin. J. Hydrometeorology 9 (5), 1020–1034.

Milly, P. C. D., Betancourt, J., Falkenmark, M., Hirsch, R. M., Kundzewicz, Z. W., Lettenmaier, D. P., Stouffer R. J., 2008. Stationarity is dead: whither water management? Science 319: 573–574.

Mirchi, A., Madani, K., Watkins, Jr D., Ahmad, S., 2012. Synthesis of system dynamics tools for holistic conceptualization of water resources problems. Water Resour Manage 26 (9):2421–2442.

Mishra, A. K., Özger, M., Singh, V. P., 2009. An entropy-based investigation into the variability of precipitation. Journal of Hydrology, 370(1-4), 139–154. doi:10.1016/j.jhydrol.2009.03.006.

Mitchell, T. D., Jones, P. D., 2005. An improved method of constructing a database of monthly climate observations and associated high-resolution grids. Int. J. Climatol., 25, 693–712, doi:10.1002/joc.1181.

Moriasi, D. N., Arnold, J. G., Van Liew, M. W., Bingner, R. L., Harmel, R. D., Veith, T.L., 2007. Model evaluation guidelines for systematic quantification of accuracy in watershed simulations. American Society of Agricultural and Biological Engineers 50 (3), 885e900.

Nalley, D., Adamowski, J., Khalil, B., 2012. Using discrete wavelet transforms to analyze trends in streamflow and precipitation in Quebec and Ontario (1954–2008). Journal of Hydrology 475:204–228.

National Oceanic and Atmospheric Administration (NOAA), 2015. Niño 3.4: Standard PSD Format. http://www.esrl.noaa.gov/psd/gcos_wgsp/Timeseries/Nino34/ (accessed March 14, 2016).

Nyaupane, N., Thakur, B., Kalra, A., Ahmad, S., 2018. Evaluating future flood scenarios using CMIP5 climate projections. Water (Switzerland), 10(12), 1–18. https://doi.org/10.3390/w10121866

Nowak, K., Hoerling, M., Rajagopalan, B., Zagona, E., 2012. Colorado River basin hydroclimatic variability. Journal of Climate, 25(12), 4389–4403. http://doi.org/10.1175/JCLI-D-11-00406.1.

Önöz, B., Bayazit, M., 2003. The power of statistical tests for trend detection. Turk. J. Eng. Environ. Sci. 27, 247–251.

Pagano, T., Garen, D., 2004. A recent increase in western US streamflow variability and persistence. Journal of Hydrometeorology 173–179. Retrieved from http://journals.ametsoc.org/doi/abs/10.1175/JHM410.1.

Palmer, P. L., 1988. The SCS snow survey water supply forecasting program: Current operations and future directions. Proc. Western Snow Conf., Kalispell, MT, 43-51.

Partal, T., Küçük, M., 2006. Long-term trend analysis using discrete wavelet components of annual precipitations measurements in Marmara region (Turkey). Physics and Chemistry of the Earth Parts A/B/C 31(18):1189– 1200. doi:10.1016/j.pce.2006.04.043.

Pathak, P., Kalra, A., Ahmad, S., Bernardez, M., 2016. Wavelet-Aided Analysis to Estimate Seasonal Variability and Dominant Periodicities in Temperature, Precipitation, and Streamflow in the Midwestern United States. Water Resources Management. doi:10.1007/s11269-016-1445-0.

Pathak, P., Kalra, A., Ahmad, S., 2017. Temperature and precipitation changes in the Midwestern United States: implications for water management. International Journal of Water Resources Development, 33(6), 1003–1019. https://doi.org/10.1080/07900627.2016.1238343

Pathak, P., Kalra, A., Lamb, K. W., Miller, W. P., Ahmad, S., Amerineni, R., Ponugoti, D. P., 2018. Climatic variability of the Pacific and Atlantic Oceans and Western US Snowpack. International Journal of Climatology, 38(3), 1257–1269. https://doi.org/10.1002/joc.5241

Percival, D. B., Walden, A. T., 2000. Wavelet Methods for Time-series Analysis. Cambridge University Press, Cambridge, p. 594.

Pettitt, A., 1979. A non-parametric approach to the change-point problem. Appl. Stat. 28, 126– 135.

Pozo-Vázquez, D., Esteban-Parra, M. J., Radrigo, F. S., Castro-Diez, Y., 2001. The association between ENSO and winter atmospheric circulation and temperature in the North Atlantic region. Journal of Climate 14, 3408–3420.

Rahaman, M., Thakur, B., Kalra, A., Ahmad, S., 2019. Modeling of GRACE-Derived Groundwater Information in the Colorado River Basin. Hydrology, 6(1), 19. https://doi.org/10.3390/hydrology6010019

Rathore, L. S., Attri, S. D., Jaswal, A. K., 2013. State level climate change trends in India, (Environment Meteorology-02/2013), 147.

Reason, C. J. C., Allan, R. J., Lindesay, J. A., Ansell, T. J., 2000. Enso and climatic signals across the Indian Ocean basin in the global context: Part I, Interannual composite patterns. International Journal of Climatology, 20(11), 1285–1327. doi:10.1002/1097-0088(200009)20:11<1285::AID-JOC536>3.0.CO;2-R.

Redmond, K. T., Koch, R. W., 1991. Surface climate and streamflow variability in the western United States and their relationship to large-scale circulation indices. Water Resour Res 27:2381–2399

Restrepo, J. M., Venkataramani, S., Comeau, D., Flaschka, H., 2014. Defining a trend for time series using the intrinsic time-scale decomposition. New Journal of Physics 16. http://doi.org/10.1088/1367-2630/16/8/085004

Robeson, S. M., 2015. Revisiting the recent California drought as an extreme value, Geophys. Res. Lett., 42, 6771–6779, doi:10.1002/ 2015GL064593.

Ropelewski, C. F., Halpert, M. S., 1986. North American precipitation and temperature patterns associated with El-Niño-Southern Oscillation (ENSO). Mon. Weather Rev. 114, 2165–2352.

Rowell, G., 1980. Many people come, looking, looking. Seattle: Mountaineers, ISBN 9780916890865.

Sagarika, S., Kalra, A., Ahmad, S., 2014. Evaluating the effect of persistence on long-term trends and analyzing step changes in streamflows of the continental United States. Journal of Hydrology, 517, 36–53. doi:10.1016/j.jhydrol.2014.05.002.

Sagarika, S., Kalra, A., Ahmad, S., 2015. Interconnections between oceanic-atmospheric indices and variability in the U.S. streamflow. Journal of Hydrology, 525, 724–736. https://doi.org/10.1016/j.jhydrol.2015.04.020

Sagarika, S., Kalra, A., Ahmad, S., 2016. Pacific Ocean and SST and Z_{500} climate variability and western U.S. seasonal streamflow. International Journal of Climatology 36, 1515– 1533. doi:10.1002/joc.4442.

Saji, N. H., Goswami, B. N., Vinayachandran, P. N., Yamagata, Y., 1999. A dipole mode in the tropical Indian Ocean. Nature 401, 360–363.

Sarlis, N. V., Skordas, E. S., Varotsos, P. A., Nagao, T., Kamogawa, M., Tanaka, H., Uyeda, S., 2013. Seismicity order parameter fluctuations in Japan. Proc. Natl. Acad. Sci. USA, 110, 13734.

Sarlis, N. V., Skordas, E. S., Varotsos, P. A., Ramírez-Rojas, A., Flores-Márquez, E. L., 2018. Natural time analysis: On the deadly Mexico M8.2 earthquake on 7 September 2017. Physica A, 506, 625.

Sarlis, N. V., Skordas, E. S., Varotsos, P. A., 2018. A remarkable change of the entropy of seismicity in natural time under time reversal before the super-giant M9 Tohoku earthquake on 11 March 2011. Europhys. Lett., 124, 29001.

Seager, R., Hoerling, M., Schubert, S., Wang, H., Lyon, B., Kumar, A., Nakamura, J., Henderson, N., 2015. Causes of the 2011–14 California drought, J. Clim., 28(18), 6997–7024.

Sellers, P. J., Field, C. B., Jensen, T. G., Bounoua, L., Collatz, G. J., Randall, D. A., Dazlich, D. A., Los, S. O., Berry, J. A., Fung, I., 1996. Comparison of radiative and physiological effects of doubled atmospheric CO2 on climate. Science. 271, 1402–1406.

Sen, P. K., 1968. Estimates of the regression coefficient based on Kendall's Tau. J. Am. Stat. Assoc. 63, 1379–1389.

Serinaldi, F., Kilsby, C. G., 2016. The importance of prewhitening in change point analysis under persistence. Stochastic Environmental Research and Risk Assessment 30(2): 763–777. http://doi.org/10.1007/s00477-015-1041-5.

Serreze, M. C., Clark, M. P., Armstrong, R. L., McGinnis, D. A., Pulwarty, R. S., 1999. Characteristics of the western U.S. snowpack from SNOTEL data. Water Resour. Res., 35, 2145–2160.

Shakya, S., Tamaddun, K., Stephen, H., Ahmad, S., 2019. Retrofitting Urban Storm Water Management System. ASCE World Environmental & Water Resources Congress, Pittsburgh, PA, May 19-23.

Shannon, C. E., 1948. A mathematical theory of communication. Bell. System Tech. J. 27, 379–423. 623–656.

Shukla, S., Safeeq, M., AghaKouchak, A., Guan, K., Funk, C., 2015. Temperature impacts on the water year 2014 drought in California, Geophys. Res. Lett., 42, 4384–4393, doi:10.1002/2015GL063666.

Singh, V. P., 1997. The use of entropy in hydrology and water resources. Hydrol. Process. 11, 587–626.

Singh, R. P., Roy, S., Kogan, F., 2003. Vegetation and temperature condition indices from NOAA AVHRR data for drought monitoring over India. International Journal of Remote Sensing, 24(22), 4393–4402. doi:10.1080/0143116031000084323.

Singh, S., 2003. India: Lonely Planet Guide. Gurgaon: Lonely Planet, ISBN 1-74059-421-5.

Singh, Y., 2010. Social Science Textbook for Class IX Geography. New Delhi: VK Publications, ISBN 978-81-89611-15-6.

Small, D., Islam, D., Vogel, R. M., 2006. Trends in precipitation and streamflow in the eastern U.S.: Paradox or perception? Geophys Res Lett 33: L03403. http://dx.doi.org/10.1029/2005GL024995.

Smith, L. C., Turcotte, D. L., Isacks, B. L., 1998. Stream flow characterization and feature detection using a discrete wavelet transform. Hydrological processes 12(2): 233-249.

Stewart, I. T., Cayan, D. R., Dettinger, M. D., 2005. Changes toward earlier streamflow timing across Western North America. J Clim 18 (8): 1136–1155.

Tamaddun, K., A., Kalra, A., Ahmad, S., 2015. Spectral Analysis of Streamflow for Continental USA. ASCE World Environmental & Water Resources Congress, Austin, TX, May 17-21.

Tamaddun, K., Kalra, A., Ahmad, S., 2016a. Identification of Streamflow Changes across the Continental United States Using Variable Record Lengths. Hydrology 3(2): 24. http://doi.org/10.3390/hydrology3020024.

Tamaddun, K., Kalra, A., Ahmad, S., 2016b. Patterns and periodicities of continental U.S. streamflow change. ASCE World Environmental & Water Resources Congress, West Palm Beach, FL, May 22-26.

Tamaddun, K. A., Kalra, A., Bernardez, M., Ahmad, S., 2017a. Multi-Scale Correlation between the Western U.S. Snow Water Equivalent and ENSO/PDO Using Wavelet Analyses. Water Resources Management, 31(9), 2745–2759. http://doi.org/10.1007/s11269-017-1659-9.

Tamaddun, K. A., Kalra, A., Ahmad, S., 2017b. Wavelet analysis of western U.S. streamflow with ENSO and PDO. Journal of Water and Climate Change 1–15. http://doi.org/10.2166/wcc.2016.162.

Tamaddun, K., Kalra, A., Ahmad, S., 2017c. Multi-scale correlation analyses between California streamflow and ENSO/PDO. ASCE World Environmental & Water Resources Congress, Sacramento, CA, May 21-25.

Tamaddun, K., Kalra, A., Ahmed, W., Dars, G. H., Burian, S., Ahmad, S., 2017d. Evaluation of spatio-temporal relationship of precipitation with Indian Ocean SST and Z500 climate variability – A case study on Pakistan. ASCE World Environmental & Water Resources Congress, Sacramento, CA, May 21-25.

Tamaddun, K., Kalra, A., Ahmad, S., 2017e. Potential of Rainwater Harvesting in meeting the domestic outdoor demand: a study in dry and wet regions of the United States. XVI World Water Congress, Cancun, Quintana, Mexico, May 29-June 2.

Tamaddun, K., Kalra, A., Ahmad, S., 2018a. Potential of rooftop rainwater harvesting to meet outdoor water demand in arid regions. Journal of Arid Land, 10(1), 68-83. https://doi.org/10.1007/s40333-017-0110-7.

Tamaddun, K., Ahmed, W., Burian, S., Kalra, A., Ahmad, S., 2018b. Reservoir Regulations of the Indus River Basin under Different Flow Conditions. ASCE World Environmental & Water Resources Congress, Minneapolis, MN, June 3-7.

Tamaddun, K. A., Kalra, A., Ahmad, S., 2019a. Spatiotemporal Variation in the Continental US Streamflow in Association with Large-Scale Climate Signals Across Multiple Spectral Bands. Water Resources Management. https://doi.org/10.1007/s11269-019-02217-8.

Tamaddun, K., Kalra, A., Bernardez, M., Ahmad, S., 2019b. Changes in Trends and Entropy during North India's Monsoon Season: Effects of ENSO on Temperature, Precipitation, and Potential Evapotranspiration. Water, 11(2), 189. https://doi.org/10.3390/w11020189.

Tamaddun, K., Kalra, A., Ahmad, S., 2019c. Ambient Air Quality of Major Indian States and Cities: A Spatiotemporal Analysis. ASCE World Environmental & Water Resources Congress, Pittsburgh, PA, May 19-23.

Tan, Z., Lu, B., Sun, Y., Sun, Y., Huang, S., 2011. Wavelet analysis of $\delta^{18}O$ time series of monthly precipitation. Int Conf Remote Sens Environ Transport Eng (RSETE) 8731–8734

Tang, C., Chen, D., Crosby, B. T., Piechota, T. C., Wheaton, J. M., 2014. Is the PDO or AMO the climate driver of soil moisture in the Salmon River Basin, Idaho? Global and Planetary Change, 120, 16–23. doi:10.1016/j.gloplacha.2014.05.008.

Taylor, K. E., Stouffer, R. J., Meehl, G. A., 2012. An overview of CMIP5 and the experiment design. Bull. Amer. Meteor. Soc., 93, 485–498.

Thakali, R., Kalra, A., Ahmad, S., 2016. Understanding the Effects of Climate Change on Urban Stormwater Infrastructures in the Las Vegas Valley. Hydrology, 3(4), 34. https://doi.org/10.3390/hydrology3040034.

Thakali, R., Kalra, A., Ahmad, S., Qaiser, K., 2018. Management of an Urban Stormwater System Using Projected Future Scenarios of Climate Models: A Watershed-Based Modeling Approach. Open Water Journal, 5(2), 1.

Theil, H., 1950. A rank-invariant method of linear and polynomial regression analysis. Adv. Stud. Theor. Appl. Econom., 23, 345–381.

Tiwari, M. K., Adamowski, J. F., 2017. An ensemble wavelet bootstrap machine learning approach to water demand forecasting: a case study in the city of Calgary, Canada. Urban Water Journal, 14(2), 185–201. http://doi.org/10.1080/1573062X.2015.1084011.

Tiwari, P. R., Kar, S. C., Mohanty, U. C., Dey, S., Kumari, S., Sinha, P., 2016a. Seasonal prediction skill of winter temperature over North India. Theoretical and Applied Climatology, 124(1-2), 15–29. doi:10.1007/s00704-015-1397-y.

Tiwari, P. R., Kar, S. C., Mohanty, U. C., Dey, S., Kumari, S., Sinha, P., Raju, P., Shekhar, M. S., 2016b. Simulations of Tropical Circulation and Winter Precipitation over North India:

an Application of a Tropical Band Version of Regional Climate Model (RegT-Band). Pure and Applied Geophysics, 173(2), 657–674. doi:10.1007/s00024-015-1102-1.

Tootle, G. A., Piechota, T. C., Singh, A., 2005. Coupled oceanic-atmospheric variability and U.S. streamflow. Water Resources Research 41(12), 1–11. doi:10.1029/2005WR004381

Torrence, C., Compo, G. P., 1998. A practical guide to wavelet analysis. Bulletin of the American Meteorological Society 79 (1): 61–78. doi:10.1175/1520-0477(1998)079<0061: APGTWA>2.0.CO;2

Torrence, C., Webster, P., 1999. Interdecadal changes in the ENSO-monsoon system. Journal of Climate, 2679–2690. Retrieved from http://journals.ametsoc.org/doi/abs/10.1175/1520-0442(1999)012%3C2679:ICITEM%3E2.0.CO;2.

Trenberth, K. E., Fasullo, J., 2007. Water and energy budgets of hurricanes and implications for climate change. Journal of Geophysical Research Atmospheres 112 (D23).

Trenberth, K. E., Hurrell, J. W., 1994. Decadal atmosphere-ocean variations in the Pacific. Climate Dynamics 9, 303–319. doi:10.1007/BF00204745.

United States Environmental Protection Agency, US EPA, 2012. Streamflow, Society and Ecosystems, Climate Change Indicators in the United States, <http://www.epa.gov/climatechange/science/indicators/society-eco/streamflow.html>

Varotsos, P. A., Sarlis, N. V., Skordas, E. S., Lazaridou, M. S., 2013. Seismic Electric Signals: An additional fact showing their physical interconnection with seismicity. Tectonophysics, 589, 116.

Varotsos, C. A., Tzanis, C., Cracknell, A. P., 2016a. Precursory signals of the major El Niño Southern Oscillation events. Theor. Appl. Climatol., 124, 903.

Varotsos, C. A., Tzanis, C. G., Sarlis, N. V., 2016b. On the progress of the 2015–2016 El Niño event. Atmos. Chem. Phys., 16, 2007–2011.

Varotsos, C. A., Sarlis, N. V., Efstathiou, M., 2018. On the association between the recent episode of the quasi-biennial oscillation and the strong El Niño event. Theor. Appl. Climatol., 133, 569.

Venema, V. K. C., et al., 2013. Benchmarking homogenization algorithms for monthly data. AIP Conference Proceedings, 1552 8, 1060–1065. https://doi.org/10.1063/1.4819690

Villarini, G., Serinaldi, F., Smith, J. A., Krajewski, W. F., 2009. On the stationarity of annual flood peaks in the continental United States during the 20th century. Water Resources Research, 45, W08417. doi:10.1029/2008WR007645.

Wallace, J. M., Zhang, Y., Lau, K. H., 1993. Structure and seasonality of interannual and interdecadal variability of the geopotential height and temperature-fields in the northern-hemisphere troposphere. Journal of Climate 6 (11), 2063–2082.

Wang, P., Clemens, S., Beaufort, L., Braconnot, P., Ganssen, G., Jian, Z., Kershaw, P., Sarnthein, M., 2005. Evolution and variability of the Asian monsoon system: State of the art and outstanding issues. Quaternary Science Reviews, 24(5-6), 595–629. doi:10.1016/j.quascirev.2004.10.002.

Wang, B., 2006. The Asian Monsoon. Berlin: Springer, ISBN 3-540-40610-7.

Webster, P. J., Yang, S., 1992. Monsoon and ENSO: Selectively interactive systems. Quart. J. Roy. Meteor. Soc., 118, 877–926.

Wei, J., Jin, Q., Yang, Z., Dirmeyer, P. A., 2016. Role of ocean evaporation in California droughts and floods. Geophysical Research Letters 6554–6562. doi:10.1002/grl.54627.

Wilks, D. S., 2006. On ''Field Significance'' and the false discovery rate. J. Appl. Meteorology Climatology 45: 1181–1189.

Williams, C. N., Menne, M. J., and Thorne, P. W., 2013. Benchmarking the performance of pairwise homogenization of surface temperatures in the United States. AIP Conference Proceedings, 1552 8(December 2011), 1072–1077. https://doi.org/10.1063/1.4821423

Williams, A. P., Seager, R., Abatzoglou, J. T., Cook, B. I., Smerdon, J. E., Cook, E. R., 2015. Contribution of anthropogenic warming to California drought during 2012–2014, Geophys. Res. Lett., 42, 6819–6828, doi:10.1002/2015GL064924.

Worland, S. C., Steinschneider, S., Hornberger, G. M., 2018. Drivers of Variability in Public-Supply Water Use Across the Contiguous United States. Water Resources Research, 1–22. http://doi.org/10.1002/2017WR021268.

Wu, G., Li, L., Ahmad, S., Chen, X., Pan, X., 2013. A dynamic model for vulnerability assessment of regional water resources in arid areas: a case study of Bayingolin, China, Water Resour. Manage 27 (8): 3085–3101.

Wuebbles, D., and Coauthors, 2014. CMIP5 climate model analyses: Climate extremes in the United States. Bulletin of the American Meteorological Society, 95(4), 571–583. http://doi.org/10.1175/BAMS-D-12-00172.1.

Xie, S. P., Hu, K., Hafner, J., Tokinaga, H., Du, Y., Huang, G., Sampe, T., 2009. Indian Ocean capacitor effect on Indo-Western Pacific climate during the summer following El Niño. Journal of Climate, 22(3), 730–747. doi:10.1175/2008JCLI2544.1.

Yang, J., Liu, Q., Xie, S. P., Liu, Z., Wu, L., 2007. Impact of the Indian Ocean SST basin mode on the Asian summer monsoon. Geophysical Research Letters, 34(2), 1–5. doi:10.1029/2006GL028571.

Yiou, P., Sornette, D., Ghil, M., 2000. Data-adaptive wavelets and multi-scale single spectra analysis. Physica D 142, 254– 290.

Yoon, J. H., Wang, S. Y., Gillies, R. R., Kravitz, B., Hipps, L., Rasch, P. J., 2015. Increasing water cycle extremes in California and in relation to ENSO cycle under global warming, Nat. Commun., doi:10.1038/ncomms9657.

Yue, S., Pilon, P., Phinney, B., Cavadias, G., 2002. The influence of autocorrelation on the ability to detect trend in hydrological series. Hydrol. Process., 16, 1807–1829.

Zhang, X., David Harvey, K., Hogg, W. D., Yuzyk, T. R., 2001. Trends in Canadian streamflow. Water Resources Research, 37(4), 987–998. doi:10.1029/2000WR900357.

CURRICULUM VITAE

Kazi Tamaddun, Ph.D. Candidate

University of Nevada, Las Vegas
Department of Civil and Environmental Engineering and Construction
Email address: kaziali.tamaddun@gmail.com

Education:

University of Nevada, Las Vegas
M.Sc., Civil and Environmental Engineering, 2016

Institute of Business Administration, University of Dhaka
M.B.A., Marketing, 2014

Bangladesh University of Engineering and Technology
B.Sc., Civil Engineering, 2012

Journal Publications:

Tamaddun, **K.**, Kalra, A., Ahmad, S., 2019. CMIP5 Models' Ability to Capture Historical Trends under the Influence of Shifts and Persistence: A Study for Colorado River Basin. *Journal of Applied Meteorology and Climatology*. (Revision submitted for the 2nd round of review)

Tamaddun, **K. A.**, Kalra, A., Ahmad, S., 2019. Spatiotemporal Variation in the Continental US Streamflow in Association with Large-Scale Climate Signals Across Multiple Spectral Bands. *Water Resources Management*. https://doi.org/10.1007/s11269-019-02217-8.

Tamaddun, **K.**, Kalra, A., Bernardez, M., Ahmad, S., 2019. Changes in Trends and Entropy during North India's Monsoon Season: Effects of ENSO on Temperature, Precipitation, and Potential Evapotranspiration. *Water*, 11(2), 189. https://doi.org/10.3390/w11020189.

Bhandari, S., Kalra, A., **Tamaddun**, **K.**, Ahmad, S., 2018. Relationship between Ocean-Atmospheric Climate Variables and Regional Streamflow of the Conterminous United States. *Hydrology*, 5(2), 30. https://doi.org/10.3390/hydrology5020030.

Tamaddun, **K.**, Kalra, A., Ahmad, S., 2018. Potential of rooftop rainwater harvesting to meet outdoor water demand in arid regions. *J. Arid Land*, 10(1), 68-83. https://doi.org/10.1007/s40333-017-0110-7.

Tamaddun, **K. A.**, Kalra, A., Bernardez, M., Ahmad, S., 2017. Multi-Scale Correlation between the Western U.S. Snow Water Equivalent and ENSO/PDO Using Wavelet

Analyses. *Water Resources Management*, 31(9), 2745–2759.
http://doi.org/10.1007/s11269-017-1659-9.

Tamaddun, **K. A.**, Kalra, A., Ahmad, S., 2017. Wavelet Analyses of Western US
Streamflow with ENSO and PDO. *Journal of Water and Climate Change*, 8(1), 26–39.
http://doi.org/10.2166/wcc.2016.162.

Tamaddun, **K.**, Kalra, A., Ahmad, S., 2016. Identification of Streamflow Changes
across the Continental United States Using Variable Record Lengths. *Hydrology*, 3(2),
24. http://doi.org/10.3390/hydrology3020024.

Dissertation Title: Multi-resolution spatio-temporal change analyses of hydro-climatological
variables in association with large-scale oceanic-atmospheric climate signals